ISBN 978-82-326-5807-7 (printed ver.)
ISBN 978-82-326-5561-8 (electronic ver.)
ISSN 1503-8181 (printed ver.)
ISSN 2703-8084 (electronic ver.)

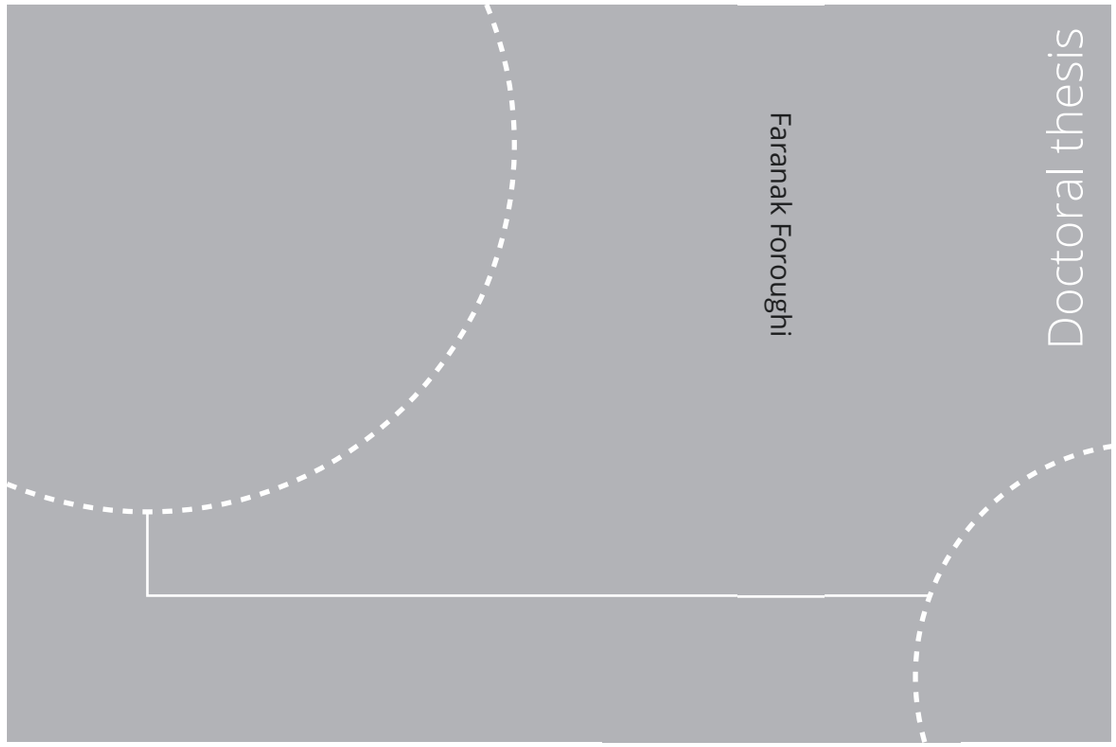

Doctoral theses at NTNU, 2022:172

Faranak Foroughi

Understanding the Effects of Power Ultrasound on the Hydrogen Evolution Reaction (HER) and the Oxygen Evolution Reaction (OER) on Polycrystalline Pt and Ni in Alkaline and Acidic Solutions

Doctoral theses at NTNU, 2022:172
Faranak Foroughi

NTNU
Norwegian University of Science and Technology

Thesis for the degree of Philosophiae Doctor
Faculty of Engineering
Department of Energy and Process Engineering

NTNU
Norwegian University of Science and Technology

Faranak Foroughi

Understanding the Effects of Power Ultrasound on the Hydrogen Evolution Reaction (HER) and the Oxygen Evolution Reaction (OER) on Polycrystalline Pt and Ni in Alkaline and Acidic Solutions

Thesis for the degree of Philosophiae Doctor

Trondheim, June 2022

Norwegian University of Science and Technology
Faculty of Engineering
Department of Energy and Process Engineering

NTNU
Norwegian University of
Science and Technology

NTNU
Norwegian University of Science and Technology

Thesis for the degree of Philosophiae Doctor

Faculty of Engineering
Department of Energy and Process Engineering

ISBN 978-82-326-5807-7 (printed ver.)
ISBN 978-82-326-5561-8 (electronic ver.)
ISSN 1503-8181 (printed ver.)
ISSN 2703-8084 (electronic ver.)

Doctoral theses at NTNU, 2022:172

PRINTED IN NORWAY
NO - 1598

NORDIC SWAN ECOLABEL
Printed matter
2041 0731

Printed by Skipnes Kommunikasjon AS

*"**Yes, my friends, I believe that water will one day be employed as fuel, that hydrogen and oxygen which constitute it, used singly or together, will furnish an inexhaustible source of heat and light, of an intensity of which coal is not capable**."*

- Jules Verne 1874, The Mysterious Island -

Preface

This thesis is submitted in partial fulfilment of the requirement for the degree of Philosophiae Doctor (Ph.D.) at the Norwegian University of Science and Technology (NTNU). The work was carried out at the Department of Energy and Process Engineering, NTNU in close collaboration with the Department of Materials science and Engineering and under the supervision of Professor Bruno G. Pollet, Associate Professor Jacob J. Lamb and Professor Svein Sunde. The Ph.D. project was funded by NTNU and the ENERSENSE research initiative with Grant Agreement Nº 81771434. In addition, all costs related to research visits and conference participation were covered by the ENERSENSE and CANOPENER programs.

Acknowledgement

This project would not have been possible without the support of many people. First and foremost, thank you to my supervisor, Professor Bruno G. Pollet, for your patience, guidance, and support. I have benefited greatly from your wealth of knowledge and meticulous editing. I am extremely grateful that you took me on as a student and continued to have faith in me over the years. I'm proud of, and grateful for, my time working with Bruno.

Many thanks to Associate Professor Jacob J. Lamb, who read my numerous revisions and helped make some sense of the confusion.

Thank you to my co-supervisor, Professor Svein Sunde, for all his help and advice with this Ph.D.

I would like to thank Professors Gregory Jerkiewicz and Christophe Coutanceau for their continuous and useful advice, guidance, and support.

Thanks to the Norwegian University of Science and Technology (NTNU) for awarding me a Dissertation Completion Fellowship, providing me with the financial means to complete this project.

Special and warm thanks go to all my ENERSENSE colleagues Silije, Lena, Yash, Islam, Pauline, Asanthie, Bjørn, Simon, Kjersti, Zohreh, Ebi, Guarav, Behnam, Markus and Henrik. I will always be grateful for your support and will always remember the wonderful time we had together. Also, I would like to special thank to the leader of ENERSENSE, Professor Odne. S. Burheim.

Many thanks to the members of Professor Gregory Jerkiewicz's group, Marina, Sho, Liam, Eduardo and Derek who provided several helpful comments and suggestions. I had also a great time with you in Kingston, Ontario, Canada.

Many thanks to Dr. Alaa Y. Faid for his assistance at every stage of the research project.

Thank you to my parents, Masoume Homayooni and Aliashar Foroughi, for your endless support. You have always stood behind me, and this was no exception. Mom, thank you for fielding a ridiculous number of phone calls, for calming me down. Dad, thank you for all of your love and for always reminding me of the end goal.

Last but not the least, thank you to my sister, Farnoush, and my brother, Kourosh, for always being there for me and for telling me that I am awesome even when I didn't feel that way.

Trondheim, March 31st 2022

List of Abbreviations and Symbols

Abbreviation

HER – Hydrogen Evolution Reaction

OER – Oxygen Evolution Reaction

HOR – Hydrogen Oxidation Reaction

ORR – Oxygen Reduction Reaction

SMR – Steam Methane Reforming

AWE – Alkaline Water Electrolyser

PEMWE – Proton Exchange membrane Water Electrolyser

AEMWE – Anion Exchange Membrane Water electrolyser

SOEC – Solid Oxide Electrolysis cell

PCCEL – Proton Conducting Ceramic Electrolyser

SEM – Scanning Electron Microscopy

HBE – Hydrogen Binding Energy

BVE – Butler-Volmer Equation

H_{upd} – Under-Potentially Deposited Hydrogen

H_{opd} – Over-Potentially Deposited Hydrogen

PGM – Platinum Group Metal

WE – Working Electrode

CE – Counter Electrode

RE – Reference Electrode

CV – Cyclic Voltammetry

LSV – Linear Sweep Voltammetry

EIS – Electrochemical Impedance Spectroscopy

ECSA– Electrochemical Surface Area

RHE – Reversible Hydrogen Electrode

SHE – Standard Hydrogen Electrode

CPE – Constant-Phase Element

pzfc – Potential of Zero Free Charge

rds – Rate-determining step

OCP – Open-Circuit Potential

US – Ultrasound

PUS – Power Ultrasound

Pt – Platinum

Ni – Nickel

N_2 – Nitrogen

RC – Charge Transfer

wt% – weight percent

NP – Nanoparticle

TPB – Triple Phase Boundary

ads – Adsorbed

BE – Binding Energy

TZR – Three-Zone Region

UHP – Ultra High Purity

Symbols

E – Potential

E^o – Standard Potential

p^o – Standard Pressure

F – Faraday's Constant

R – Universal Gas Constant

R – Resistance

T – Temperature

η – Overpotential

b – Tafel slope

j_o – Exchange current density

j – Current Density

I – Current

C_{dl} – Double-layer capacitance

C – Capacitance

z – Number of Electrons

A – Surface Area

Q – Charge

v – Scan Rate

P – Power

t – time

Ø – Diameter

Abstract

The aim of this Ph.D. project was to investigate the effect of power ultrasound on the hydrogen evolution reaction (HER) and the oxygen evolution reaction (OER) on polycrystalline nickel (Ni) and platinum (Pt) in alkaline and acidic electrolytes in order to understand the kinetics and mechanisms of HER and OER at these electrodes under ultrasonic conditions. The secondary objective was to elucidate the mechanism(s) for the observed decrease in cell voltages and the anodic and cathodic overpotentials in the presence of ultrasonication.

In the present dissertation, firstly, we investigated the effects of power ultrasound (26 kHz, up to 100% acoustic amplitude) on the HER on polycrystalline Pt disc electrode in 0.5 M H_2SO_4 by cyclic and linear sweep voltammetry at 25 °C. We also studied the formation of molecular hydrogen bubbles on a Pt wire in the absence and presence of power ultrasound using ultra-fast camera imaging. It was found that ultrasound significantly increases currents towards the HER i.e., a ~250% increase in current density was achieved at maximum ultrasonic power. The potential at a current density of -10 mA cm^{-2} under *silent* conditions was found to be -46 mV and decreased to -27 mV at 100% acoustic amplitude i.e., a ΔE shift of ~+20 mV, indicating the influence of ultrasound on improving the HER activity. A nearly 100% increase in the exchange current density (j_o) and a 30% decrease in the Tafel slope (b) at maximum ultrasonic power, was observed in the low overpotential region, although in the high overpotential region, the Tafel slopes (b) were not significantly affected when compared to *silent* conditions.

Motivated by the fact that Ni and Ni-based materials have attracted great interest in the development of renewable energy technologies, including fuel cells and water electrolysers, and due to their good stability, catalytic activity, abundance, and lower cost when compared to the currently used Platinum Group Metals (PGM)-based materials, we designed a facile and scalable approach for activating the surface of metallic Ni for the HER in aqueous alkaline media through continuous and pulsed ultrasound (24 kHz, 44 W, 60% acoustic amplitude). Sonoactivated Ni showed a remarkably enhanced HER activity with a much lower overpotential at −10 mA cm^{-2} of −277 mV *vs.* RHE when compared to non-sonoactivated Ni. The outcome of our research offers a novel route for activating Ni-based materials by ultrasonic treatment to tune the chemical composition and electrocatalytic activity of the Ni surface for the electrochemical water splitting reaction.

Understanding the activity dependence of the KOH concentration (pH) of alkaline electrolytes is essential for designing durable and active HER catalysts. Motivated by this fact, the HER activity and kinetics of polycrystalline and nanostructured nickel-based catalysts were evaluated in various pH's and KOH concentrations. The results for nanostructured NiMo catalyst indicate that both electrochemical active surface area and reaction order have a promoting region under various pH and KOH concentrations (0.01 M-1.0 M, pH=12-14) accompanied by better HER activity (a lower overpotential for achieving -10 mA cm^{-2}) and Tafel slope decreases from around 180 mV dec^{-1} to 60 mV dec^{-1} in the same pH and KOH concentration range. The polycrystalline Ni displays different behaviour where a promoting (0.01 to 0.10 M, pH = 12-13), stabilizing (0.1 to 1.0 M, pH 13-14), and an inhibiting region (2.0 M, pH > 14) are present. However, Tafel slopes of around 120 mV dec^{-1} are obtained for polycrystalline Ni at all KOH concentrations. The HER characteristics are inhibited at 2.0 M KOH for both catalysts due to slower OH^- transport kinetics. The results confirmed the importance of tuning catalyst-pH/KOH concentration for better HER activity and kinetics.

The development of cost-effective and active water-splitting electrocatalysts is an essential step towards the realisation of sustainable energy. Its success requires an intensive improvement in the kinetics of the anodic half-reaction of the OER, which determines the overall system efficiency to a large extent. Motivated by this, we developed a facile and one-route strategy to activate the surface of metallic nickel (Ni) for the OER in alkaline media by ultrasound (24 kHz, 44 W, 60% acoustic amplitude). Sonoactivated Ni showed enhanced OER activity with a much lower potential at +10 mA cm^{-2} of +1.594 V *vs.* RHE after 30 min ultrasonic treatment compared to +1.617 V *vs.* RHE before ultrasonication. In addition, lower charge transfer resistance of 11.1 Ω was observed for sonoactivated Ni as compared to 98.5 Ω for non-sonoactivated Ni.

Finally and for completeness of the Ph.D. project, the electrochemical kinetics and mechanism of Raney-Ni towards the HER and the OER under *silent* (no ultrasound) and ultrasonic (408 kHz) conditions have been investigated in 30 wt.- % aqueous KOH solution at different temperatures (T = 25, 40 and 60 °C). It was observed that there is a significant difference between the effect of ultrasonication on the HER and the OER. Ultrasonication significantly shifts the overpotential at -300 mA cm^{-2} (η_{300}) of HER by +34 mV at 25 °C due chiefly to the effective bubble removal while it does not influence the OER overpotential. It was also shown that the ultrasonic effect on the HER depends upon temperature, and ultrasonication does not play a remarkable role at high temperatures. Moreover, ultrasonication cannot overcompensate for the decreasing HER activity by lowering the temperature.

Author's contributions to the published articles

Paper 1. Does Power Ultrasound (26 kHz) Affect the Hydrogen Evolution Reaction (HER) on Pt Polycrystalline Electrode in a Mild Acidic Electrolyte?

Bruno G. Pollet, **F. Foroughi**, A. Y. Faid, D. R. Emberson, Md. H. Islam.

The idea of this work was developed by Prof. Bruno G. Pollet. The experimental works and data analysis were carried out by Faranak Foroughi. The main manuscript was drafted by Prof. Bruno G. Pollet and Faranak Foroughi with comments and discussion from Prof. Bruno G. Pollet and Dr. Alaa Y. Faid. The high-speed camera imaging was performed by Dr. David. R. Emberson and Dr. Md. H. Islam.

Paper 2. *In-situ* Sonoactivation of Polycrystalline Ni for the Hydrogen Evolution Reaction (HER) in Alkaline Media

F. Foroughi, G. Jerkiewicz, A.Y. Faid, S. Sunde, C. Coutanceau, B.G. Pollet.

This work was carried out as the main part of the Ph.D. project of Faranak Foroughi. Under the supervision of Prof. Bruno G. Pollet and Prof. Svein Sunde. Faranak Foroughi planned and carried out the main experimental work. The main manuscript was drafted by Faranak Foroughi with input, comments, and discussion from Prof. Bruno G. Pollet, Prof. Svein Sunde, Prof. Christophe Coutanceau, Prof. Gregory Jerkiewicz and Dr. Alaa Y. Faid.

Paper 3. Unveiling Hydrogen Evolution Dependence on KOH Concentration for Polycrystalline and Nanostructured Nickel-based Catalysts

A.Y. Faid, **F. Foroughi**, S. Sunde, B.G. Pollet.

The idea of this work was developed by Faranak Foroughi and Dr. Alaa Y. Faid. The experimental works and data analysis were carried out by Faranak Foroughi and Dr. Alaa Faid. The main manuscript was drafted by Faranak Foroughi and Dr. Alaa Y. Faid with comments and discussion from Prof. Bruno G. Pollet and Prof. Svein Sunde. Dr. Alaa Y. Faid and Faranak Foroughi have the same contribution in this work.

Paper 4. Sonoactivated Polycrystalline Ni Electrodes for Alkaline Oxygen Evolution Reaction (OER)

F. Foroughi, A.Y. Faid, S. Sunde, B.G. Pollet.

Faranak Foroughi planned and carried out the experimental work, analysed the data, and drafted the main manuscript with comments and discussion from Prof. Bruno G. Pollet, Dr. Alaa Y. Faid and Prof. Svein Sunde.

Paper 5. Understanding the Effects of Ultrasound (408 kHz) on the Hydrogen Evolution Reaction (HER) and the Oxygen Evolution Reaction (OER) on Raney-Ni in Alkaline Media

F. Foroughi, C.I. Bernäcker, L. Röntzsch, B.G. Pollet.

This work was the last of part of the PhD project of Faranak Foroughi in collaboration with Fraunhofer IFAM (Germany). Prof. Bruno G. Pollet supervised the project. The electrodes were provided by Fraunhofer IFAM. Faranak Foroughi carried out the experimental work, analysed the data, and drafted the main manuscript with comments and discussion from Prof. Bruno G. Pollet, Dr. C.I. Bernäcker and Dr. L. Röntzsch.

Table of Contents

1 Introduction

1.1 Background and motivation

Hydrogen is the simplest and most abundant element on earth. Hydrogen can store and deliver usable energy, but it does not typically exist by itself in nature and must be produced from compounds that contain it. Hydrogen is mainly an energy carrier and not an energy source as such, because it is produced by means of a chemical reaction from a primary resource.

1.1.1 Sources of Hydrogen Energy

Hydrogen can be produced from different sources. Currently, most of the hydrogen is produced from fossil fuels, specifically from natural gas. Electricity from the grid or from renewable sources such as biomass, geothermal, solar, hydro or wind is also currently used to produce hydrogen. In the longer term, solar energy and biomass can be used more directly to generate hydrogen as new technologies make alternative production methods cost competitive [1]. Figure 1.1 illustrates that the majority of hydrogen used today is produced from fossil fuels [2].

1.1.2 Hydrogen Production Pathways

Hydrogen can also be produced through steam methane reforming (SMR), a high-temperature process in which steam reacts with a hydrocarbon fuel to produce hydrogen. Another common hydrogen production method takes water (H_2O) and splits the H_2O molecule into oxygen and hydrogen through a process called water electrolysis. Electrolysis takes place in an electrolyser, which functions much like a fuel cell in reverse—instead of using the energy of a hydrogen (and an oxygen) molecule, like a fuel cell does, an electrolyser produces hydrogen (and oxygen) from water molecules. Biological processes can also produce hydrogen through biological reactions using microbes, bacteria and microalgae. In these processes, microbes consume plant material to produce hydrogen gas. There are many ways to produce hydrogen for example, using sunlight, including photobiological, photoelectrochemical, photovoltaic-driven electrolysis, and solar thermochemical processes [1, 3].

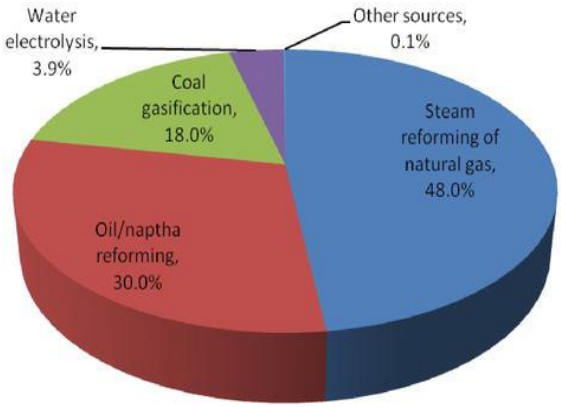

Figure 1.1. Global hydrogen production from main sources [2].

1.1.3 Hydrogen as an Energy Carrier

As stated earlier, hydrogen is an energy carrier, not an energy source and can deliver or store large amount of energy. Hydrogen can be used in fuel cells to generate electricity or burnt in an ICE (internal combustion engine) to release power and heat. Today, hydrogen is mostly used in petroleum refining and fertilizer production, while transportation and utilities are emerging markets [1].

1.1.4 Uses for Hydrogen

Hydrogen is a clean fuel that, when consumed in a fuel cell, produces only water, electricity, and heat. Hydrogen and fuel cells can play an important role in the energy strategy and energy transition, with the potential for use in a broad range of applications, across almost all sectors, e.g., transportation, commercial, industrial, residential, and portable. Hydrogen and fuel cells can provide energy for use in diverse applications, including distributed or combined-heat-and-power; backup power; systems for storing and enabling renewable energy; portable power; auxiliary power for trucks, aircraft, rail, and ships; specialty vehicles such as forklifts; and passenger and freight vehicles including cars, trucks, and buses. Figure 1.2 shows an overview of hydrogen energy sources and uses [4].

Due to their high efficiency and zero-or near zero-emissions operations, hydrogen and fuel cells have the potential to reduce greenhouse gas (GHG) emissions in many sectors. Many energy analysis reports have shown that hydrogen and fuel cells have the potential to achieve the following reductions in emissions [1]:

- Light-duty highway vehicles: more than 50% to more than 90% reduction in emissions over today's gasoline vehicles.

- Specialty vehicles: more than 35% reduction in emissions over current diesel and battery-powered lift trucks.
- Transit buses: demonstrated fuel economies of approximately 1.5 times greater than diesel internal combustion engine (ICE) buses and approximately 2 times higher than natural gas ICE buses.
- Auxiliary power units (APUs): more than 60% reduction in emissions compared to truck engine idling.
- Combined heat and power (CHP) systems: 35% to more than 50% reduction in emissions over conventional heat and power sources (with much greater reductions—more than 80%—if biogas or hydrogen from low- or zero-carbon sources is used in the fuel cell).

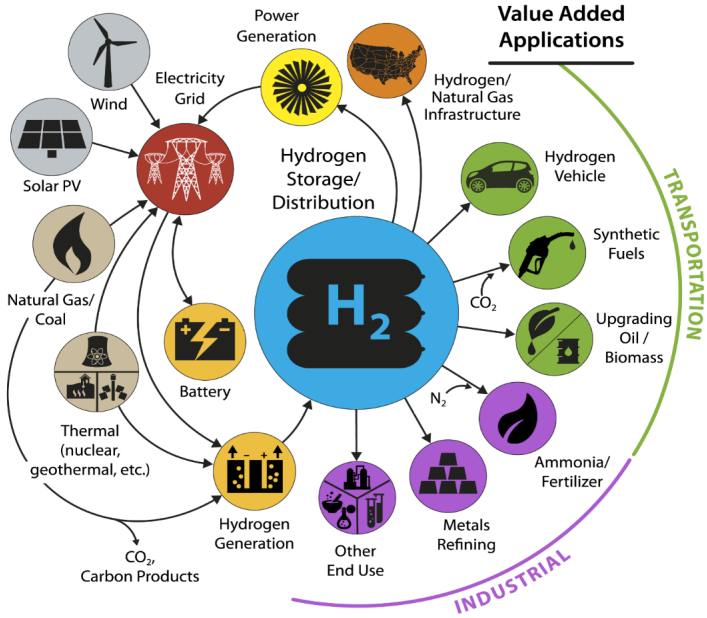

Figure 1.2. Hydrogen sources and uses of hydrogen energy [4].

The greatest challenge for hydrogen production, particularly from renewable resources, is providing hydrogen at lower cost (when compared to other traditional fuels). For transportation fuel cells, hydrogen must be cost-competitive with conventional fuels and technologies on a per-mile basis. This means that the cost of hydrogen regardless of the production technology—must be less than 0.55 $/litre of gasoline equivalent. To reduce the overall hydrogen cost, research is focused on improving the efficiency and lifetime of hydrogen

production technologies as well as reducing the cost of capital equipment (CAPEX), operations (OPEX), and maintenance [1].

As more countries pursue deep decarbonisation strategies, hydrogen will have a critical role to play. In this regard, hydrogen needs to be low carbon from the outset and ultimately green (produced by the electrolysis of water using renewable electricity) [5]. In addition to regulations and market design, the cost of production is a major barrier to the uptake of "green hydrogen". Costs are falling largely due to falling renewable power costs, but "green hydrogen" is still 2-3 times more expensive than "blue hydrogen" (produced from reformed fossil fuels with carbon capture and storage, CCS) and further cost reductions are needed [5]. The largest single cost component for on-site production of "green hydrogen" is the cost of the renewable electricity needed to power the electrolyser unit. This renders production of "green hydrogen" more expensive than "blue hydrogen", regardless of the cost of the electrolyser. A low cost of electricity is therefore a necessary condition for producing competitive "green hydrogen". This creates an opportunity to produce hydrogen at locations around the world that have optimal renewable resources, in order to achieve competitiveness. However, low electricity cost is not enough by itself for competitive "green hydrogen" production, and reductions in the cost of electrolysis facilities are also needed [5]. This is the second largest cost component of "green hydrogen" production. There are some key strategies to reduce investment costs for electrolysis plants from 40% in the short term to 80% in the long term. These strategies range from the fundamental design of the electrolyser stack to broader system-wide elements, including [5]: a) electrolyser design and construction, b) economies of scale, c) procurement of materials d) efficiency and flexibility in operations.

In Chapter 2, we will discuss in more details the water electrolysis fundamentals and the characteristics of each type of water electrolysers.

1.2 Aim of the thesis

The efficiency of water electrolysis can therefore be increased by controlling the following factors: (a) more effective disengagement of molecular hydrogen (H_2) and oxygen (O_2) gas bubbles from the cathode and anode electrodes and the membranes, thereby virtually eliminating gas blanketing; (b) making gas bubble removal more effective from the electrolyte, even with very small electrode spacing; and (c) promoting faster removal of the gas bubbles at the electrode surface to increase the local heat/mass transfer coefficients. In order to enhance the transfer process more effectively, the boundary layer of the three-zone region (TZR) should be significantly reduced or even eliminated since gas bubbles generated on the electrode surfaces are involved in the interfacial phenomena in the TZR [6, 7]. According to the above considerations, it should be possible to carry out electrochemical operations, in which gas is evolved at one or both electrodes in the presence of an ultrasonic field. On the basis that water electrolysis is an important electrochemical operation worldwide, the possibility of providing the basis for a more realistic cell design for water electrolysis in an ultrasonic field is a valuable area for investigation. In particular, the energy and the investment in equipment needed to create the ultrasonic field are quite small compared to the energy that could be saved. For example, a 100 kA cell suffering from a bubble overvoltage of 0.3 V has a potential energy saving of 30 kW; whereas, the energy of the ultrasonic field will be about 0.05 kW [8]. The effects of ultrasound on many electrochemical processes can be found in the literature [8-14], however, fundamental studies on the effect of ultrasound on the HER and OER in alkaline and acidic solutions are scarce and require further investigations. This fundamental research project will focus on overcoming a significant gap in this research field by posing the following scientific question:

Does power ultrasound affect the hydrogen and oxygen evolution reactions on polycrystalline Pt and Ni?

This project is aimed at elucidating and understanding the electron-transfer mechanisms at polycrystalline Pt (platinum) and Ni (nickel) electrodes under ultrasonic conditions. It is also to separate the observed sonochemical effects on electrode kinetics from the mechanical, chemical, and thermal contributions. The secondary objective is to elucidate the mechanism(s) for the observed decrease in cell voltages, and the anodic and cathodic overpotentials in the presence of ultrasonication.

The main objectives of this research project include:

(i) Investigating and understanding the sonoelectrochemical mechanism(s) of HER and OER on polycrystalline Pt and Ni;
(ii) Separating the effect of sonochemical (free radical formation), temperature and mass-transport from the sonoelectrochemically generated data.

The *sub-objectives* for this investigation are as follows:

(i) The effect of ultrasonic power on the HER on polycrystalline Pt in acidic media.
(ii) The effect of ultrasonic power and frequency on the HER and OER on polycrystalline Ni in alkaline media.
(iii) The effect of ultrasound on the electrode active surface area and surface roughness of Pt and Ni in alkaline and acidic solutions.
(iv) The effect of concentration, pH and scan rate on the HER on polycrystalline Ni in alkaline media

For completeness, the effect of ultrasound on the HER and the OER on Raney-Ni at various temperatures in alkaline media was also investigated.

1.3 List of Articles

This thesis contains the following five (5) articles published or submitted in renowned international high impact factor peer-reviewed journals:

1. "Does Power Ultrasound (26 kHz) Affect the Hydrogen Evolution Reaction (HER) on Pt Polycrystalline Electrode in a Mild Acidic Electrolyte?" Bruno G. Pollet, **F. Foroughi**, A. Y. Faid, D. R. Emberson, Md. H. Islam. *Ultrasonic Sonochemistry*, 69, 105238, 2020. https://doi.org/10.1016/j.ultsonch.2020.105238

2. "*In-situ* Sonoactivation of Polycrystalline Ni for the Hydrogen Evolution Reaction (HER) in Alkaline Media" **F. Foroughi**, G. Jerkiewicz, A.Y. Faid, S. Sunde, C. Coutanceau, B.G. Pollet. **Submitted** in *ACS Applied Energy Materials*.

3. "Unveiling Hydrogen Evolution Dependence on KOH Concentration for Polycrystalline and Nanostructured Nickel-based Catalysts". A.Y. Faid, **F. Foroughi**, S. Sunde, B.G. Pollet. **Under review** in *Journal of Applied Electrochemistry*.

4. "Sonoactivated Polycrystalline Ni Electrodes for Alkaline Oxygen Evolution Reaction (OER)" **F. Foroughi**, A.Y. Faid, S. Sunde, B.G. Pollet. *Ultrasonics Sonochemistry*, 106013, 2022. https://doi.org/10.1016/j.ultsonch.2022.106013

5. "Understanding the Effects of Ultrasound (408 kHz) on the Hydrogen Evolution Reaction (HER) and the Oxygen Evolution Reaction (OER) on Raney-Ni in Alkaline Media" **F. Foroughi**, C.I. Bernäcker, L. Röntzsch, B.G. Pollet. *Ultrasonics Sonochemistry*, 105979, 2022. https://doi.org/10.1016/j.ultsonch.2022.105979

In addition, during the work as a Ph.D. candidate at the "Hydrogen Energy and Sonochemistry research group", the author has contributed to the following peer-review articles and conference proceeding.

Other peer-reviewed articles

1. "The Use of Ultrasound for the Electrochemical Synthesis of Magnesium Ammonium Phosphate Hexahydrate (Struvite)." **F. Foroughi**, László Kekedy-Nagy, Md. H. Islam, Jacob J. Lamb, Lauren F. Greenlee, and Bruno G. Pollet. *ECS Transactions* 92 (10), 47. Orally presented in 236th ECS meeting, Atlanta, GA, October 2019.

2. "Sonochemical and Sonoelectrochemical Production of Energy Materials" **F. Foroughi**, J.J. Lamb, O.S. Burheim, B.G. Pollet. *Catalysts*, 284, (2)11, 2021. https://doi.org/10.3390/catal11020284

3. "Advances, Opportunities and Challenges of Hydrogen and Oxygen Production from Seawater Electrolysis: An Electrocatalysis Perspective" E. Asghari, M. Imran Abdullah, **F. Foroughi**, J.J. Lamb, B.G. Pollet. *Current Opinion in Electrochemistry* 31, 100879. https://doi.org/10.1016/j.coelec.2021.100879

Other contributions

"The Effect of Power Ultrasound on the Electrochemical Rest Potential" **F. Foroughi**, M. Tintor, G. Jerkiewicz, B.G. Pollet. The last meeting of Ni Electro Can, Kingston, Ontario, Canada (Poster and 15 min oral talk).

References

[1] Satyapal, S. *Hydrogen: A Clean, Flexible Energy Carrier* 2017 [cited 2022 03.02.2022]; Available from: https://www.energy.gov/eere/articles/hydrogen-clean-flexible-energy-carrier.

[2] Ewan, B. and R. Allen, *A figure of merit assessment of the routes to hydrogen.* International Journal of Hydrogen Energy, 2005. **30**(8): p. 809-819.

[3] Lamba, J.J., et al., *Traditional routes for hydrogen production and carbon conversion.* Hydrogen, Biomass and Bioenergy: Integration Pathways for Renewable Energy Applications, 2020: p. 21.

[4] Casey, T. *Renewable Hydrogen Sneak Attack On "Toughest Third" Of Global CO2 Emissions* 2020 0.3.02.2022]; Available from: https://cleantechnica.com/2020/03/31/renewable-hydrogen-sneak-attack-on-toughest-third-of-global-co2-emissions-cleantechnica-exclusive-interview/.

[5] IRENA, *Green Hydrogen Cost Reduction: Scaling up Electrolysers to Meet the 1.5ºC Climate Goal*. 2020: Abu Dhabi.

[6] Wüthrich, R., C. Comninellis, and H. Bleuler, *Bubble evolution on vertical electrodes under extreme current densities.* Electrochimica Acta, 2005. **50**(25-26): p. 5242-5246.

[7] Wang, C.-C. and C.-Y. Chen, *Water electrolysis in the presence of an ultrasonic field.* Electrochimica Acta, 2009. **54**(15): p. 3877-3883.

[8] Li, S.-D., C.-C. Wang, and C.-Y. Chen, *Water electrolysis in the presence of an ultrasonic field.* Electrochimica Acta, 2009. **54**(15): p. 3877-3883.

[9] Pollet, B., *Power ultrasound in electrochemistry: from versatile laboratory tool to engineering solution. 2012*. John Wiley & Sons.

[10] Islam, M.H., et al., *Sonochemical conversion of CO2 into hydrocarbons: The Sabatier reaction at ambient conditions.* Ultrasonics Sonochemistry, 2021. **73**: p. 105474.

[11] Le Naour, C., et al., *Effect of power ultrasound on the electrochemical platinum/HCOOH interface.* Journal of Electroanalytical Chemistry, 2001. **501**(1-2): p. 215-221.

[12] Lepesant, M., *Sonoelectrochemical Production of Hydrogen for PEM Fuel Cell Applications*. 2011.

[13] Lin, M.-Y. and L.-W. Hourng, *Ultrasonic wave field effects on hydrogen production by water electrolysis.* Journal of the Chinese Institute of Engineers, 2014. **37**(8): p. 1080-1089.

[14] Cherepanov, P.V., et al., *The use of ultrasonic cavitation for near-surface structuring of robust and low-cost AlNi catalysts for hydrogen production.* Green chemistry, 2015. **17**(5): p. 2745-2749.

2 Literature review: Hydrogen Evolution Reaction (HER) and Oxygen Evolution Reaction (OER) on Bulk Pt, Metallic Ni and Oxidized Ni Electrodes in Aqueous Media

Electrochemical water splitting technologies for hydrogen generation will play a key role in meeting climate change targets [1]. Currently, less than 0.1% of the global hydrogen is produced through water electrolysis, while 99% is still produced through the steam methane reforming (SMR) of fossil methane [2-4]. Water electrolysers have the potential to provide the foundation of a sustainable hydrogen production network suitable for being coupled to intermittent renewable energy systems (RES) [5-8].

Electrochemical water splitting is a process in which a direct current (DC) is passed between two electrodes in an aqueous solution by applying a cell voltage (V_{cell}), where gaseous molecular hydrogen (H_2, also referred to as di-hydrogen) and oxygen (O_2, also referred to as di-oxygen) are generated at the cathode and anode, respectively [3, 5, 6, 9]. It involves two half-cell reactions: the hydrogen evolution reaction (HER) taking place at the cathode (the negative electrode) and the oxygen evolution reaction (OER) at the anode (the positive electrode) [9-12]. The reverse processes generate electrical energy (processes in blue, Figure 2.1) in fuel cells [5]. These half-cell reactions occurring in aqueous acidic and alkaline conditions are defined in Table 2.1 [10].

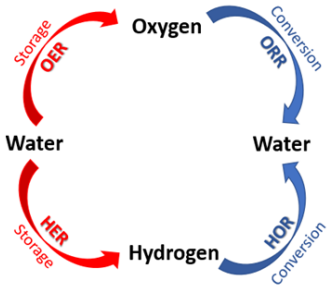

Figure 2.1. Hydrogen and oxygen cycle for electrical energy storage and electrical energy conversion. The two half-cell reactions employed for energy storage by water electrolysis are the hydrogen evolution reaction (HER) and the oxygen evolution reaction (OER), and the two half-cell reactions used for energy generation in fuel cells are the hydrogen oxidation reaction (HOR) and the oxygen reduction reaction (ORR).

Table 2.1. The hydrogen evolution reaction (HER) and oxygen evolution reaction (OER) occurring in aqueous acidic and alkaline conditions.

Half-cell reaction	*Redox*	*Acid*	*Alkaline*
HER	*Reduction*	$2H^+ + 2e^- = H_2, E^o = 0.000\ V_{SHE}$	$2H_2O + 2e^- = H_2 + 2OH^-, E^o = -0.828\ V_{SHE}$
OER	*Oxidation*	$H_2 = 1/2O_2 + 2H^+ + 2e^-, E^o = +1.229\ V_{SHE}$	$2OH^- = 1/2O_2 + H_2O + 2e^-, E^o = +0.401\ V_{SHE}$

2.1 Water Electrolysis

Water electrolysis is the most significant primary electrochemical method for H_2 (and O_2) production, and its importance will increase rapidly with renewable energy production in the near future [5, 6]. Depending on the electrolytes, separators, working temperatures and pressures employed, currently there are four main types of water electrolysers, namely:

1. Proton Exchange Membrane Water Electrolyser (PEMWE, liquid water, perfluorosulfonic acid (PFSA), <80 °C, <200 bar);
2. Alkaline Water Electrolyser (AWE, aqueous KOH or NaOH, < 80 °C, < 30 bar);
3. Anion Exchange Membrane Water Electrolyser (AEMWE, etc)
4. Solid Oxide Electrolyser (SOEL, water steam, 500-850 °C, atmospheric); and,
5. Proton Conducting Ceramic Electrolyser (PCCEL, etc) [13].

2.1.1 Proton Exchange Membrane Water Electrolysers (PEMWE)

Proton exchange membrane water electrolysers (PEMWEs) are considered to be the most effective water electrolysis technology [14]. One of the critical components in a PEMWE is the use of expensive and scarce PGMs (platinum group metals) and ion-exchange membrane. The two electrodes (the anode and cathode) form a sandwich against a proton-conducting polymer electrolyte. This sandwich forms the so-called membrane electrode assembly (MEA). This MEA is then immersed in high purity water, and a cell voltage (V_{cell}) is applied. The O_2 evolution then occurs at the anode, as shown in equation (2.1):

$$H_2O = \frac{1}{2}O_2 + 2e^- + 2H^+ \quad (E_A^o = +1.229\ \text{V}\ vs.\ \text{SHE at 25 °C}) \tag{2.1}$$

The hydrogen ions from the water splitting are then transported across the ion-exchange membrane and H_2 is generated at the cathode as shown in equation (2.2):

$$2H^+ + 2e^- = H_2 \quad (E_C^o = 0.000\ \text{V vs. SHE at 25 °C}) \tag{2.2}$$

Therefore, the overall reaction in a PEMWE is shown in equation (2.3):

$$H_2O \rightarrow H_2 + \frac{1}{2}O_2 \qquad (E^o = +1.229\ \text{V at 25 °C}) \tag{2.3}$$

Importantly, there is no net consumption of the electrolyte and only water is consumed as water electrolysis takes place. Provided that water is supplied at the rate at which it is consumed, the concentration of the ions remains constant. During the electrolysis, mobile species remain confined within the polymer membrane, resulting in very high acidity. Due to this, noble metal catalysts that resist (chemically stable) such a highly acidic environment, are required as both the cathode and the anode materials. However, it should be recognized that even Pt materials undergo slow but unavoidable degradation in acidic media and the rate their corrosive degradation is strongly related to the potential and temperature conditions [15].

Modern PEMWEs contain perfluorinated sulfonic acid co-polymer membranes because of their relatively high ionic conductivity (as compared to other membrane materials), high mechanical strength, and strong chemical stability. The most widely used membrane material is Nafion® developed by DuPont de Nemours Co. (USA). Nafion® membranes are thin, elastic, and transparent. However, swelling and dissociation of the ion-exchange groups of the membrane can occur when in contact with water, resulting in the free movement of protons from one electrode to another. At high temperatures (> 90 °C), the durability is further reduced due to the dehydration of the membrane and the subsequent drop in proton (H^+) conductivity [16]. The resistivity of perfluorinated sulfonic acid membranes is significantly larger than that of alkali solutions (i.e., 11-12 Ω cm^{-1} at 20 °C and 5-6 Ω cm^{-1} at 80-90 °C). Thin membranes having a thickness in the 100-300 μm range are used to reduce ohmic losses. However, the use of thin membranes increases the permeability of gases through the membrane, reducing the efficiency of the system. Since liquid electrolytes are not used in PEMWEs, the electrodes are pressed tightly against the membrane in a zero-gap configuration. The catalysts used in PEMWEs are deposited on the surface of the ion-conducting membrane in order to achieve high surface contact between the catalyst and the electrolyte [17]. Porous current collectors can then be pressed firmly against these catalytic layers with adjacent electrolysis cells stacked together and separated by metallic bipolar plates.

The catalysts used in PEMWEs are generally PGMs. Ruthenium (Ru) is one such PGM that has high catalytic activity in the O_2 evolution reaction (OER). However, it should be noted that Ru reveals poor stability in acidic conditions [18]. The most commonly used anode catalyst is iridium (Ir) with loadings of around 2.0 mg cm^{-2}, whereas platinum (Pt) or palladium (Pd) are the main catalysts used at the cathode, with the anode current collectors being constructed

of a porous titanium (Ti) material and the cathode current collectors being constructed of a platinum (Pt)/carbon material. The current collectors are used to supply the required potential.

When compared to other water electrolysers, the main advantages of a PEMWEs are as follows:

1. Possibility of operating at high current densities;
2. High energy efficiency;
3. High purity of generated gases; and
4. A high dynamic range (ideal for use with intermittent renewable energy).

The main drawbacks are:

1. High initial capital investment related to the cost of precious metals; and
2. Requirement for high-purity water feed.

2.1.2 Alkaline Water Electrolyser (AWE)

The alkaline water electrolyser cell consists of two metallic electrodes that are immersed in an aqueous electrolyte (e.g., aqueous solutions of KOH or NaOH generally 25-30 wt% in concentration; the working temperature range is 70-100°C) [19]. In order to provide maximum electrical conductivity at temperatures up to 90°C (e.g., KOH has a specific conductivity of 54.3 × 10^{-2} Ω^{-1} cm^{-1} at 25°C), the electrolyte solution usually has a concentration of up to 40% w/w (7.14 M) [20]. The reduction of water in an AWE takes place at the cathode of the electrolyser according to equation (2.4):

$$2H_2O + 2e^- = H_2 + 2OH^- \qquad (E_C^o = -0.828\ \text{V}\ vs.\ \text{SHE}) \tag{2.4}$$

while the hydroxyl ion oxidation occurs at the anode according to equation (2.5):

$$2OH^- = \frac{1}{2}O_2 + H_2O + 2e^- \qquad (E_A^o = +0.401\ \text{V}\ vs.\ \text{SHE}) \tag{2.5}$$

Therefore, the overall reaction in an AWE is shown in equation (2.6):

$$H_2O \rightarrow H_2 + \frac{1}{2}O_2 \qquad (E^o = +1.229\ \text{V at 25°C}) \tag{2.6}$$

Water and electrical energy are consumed during electrolysis; therefore, water and electricity must be supplied to the cell for the reactions to continue over prolonged periods of time. The addition of water must be constant to maintain an optimum concentration and a suitable and constant level of the electrolyte in the electrolyser. During the alkaline electrolysis, the gaseous products can carry away water vapour and traces of electrolyte at typical operating temperatures (60-80°C); however, on a dry basis, the purity of the produced H_2 is usually around 99.9% [3, 5, 6].

To avoid the spontaneous back recombination of H_2 and O_2 into the water, a cell separator in the form of a porous material is placed between the two electrodes. However, in an AWE gap-cell configuration, there is only a small gap (i.e., a few mm) between the electrodes and the separator where the gaseous H_2 and O_2 are evolved. When the current density increases in this configuration, gas bubbles form a continuous and highly resistive film at the surface of the electrodes, effectively limiting the operating current densities to 100 mA cm^{-2} [3]. One way to overcome this challenge is to use porous electrodes that can be pressed against the cell separator [3]. This results in a lower interpolar distance with the gases being evolved at the back of the electrodes increasing the current density [3].

In a typical AWE, pre-cleaned steel grids are used as electrodes. The charge transfer kinetics of the cell can then be improved by applying a layer of porous nickel. Asbestos (a natural silicate mineral) has been previously used as a porous diaphragm to separate the anode and cathode. However, due to its toxicity, research efforts have led to the development of a large variety of alternative solutions, in particular polymer-based composite materials that are used as separators [21]. Despite this, the presence of a porous diaphragm can generate operating problems (e.g., safety issues due to the possible mixing of produced gases at elevated pressures)[22]. In addition, the gas purity from the AWE usually decreases when the operating pressure is raised. Moreover, the H_2 quality in AWEs is still low due to the possible O_2, water vapour, and alkali impurities, meaning additional purification steps may be required to reach higher H_2 purities. Regardless, AWEs offer numerous advantages because: (i) they require relatively low initial capital investment (electrodes and separators), (ii) they are a proven technology, (iii) their large capacity units have been established industrially, and (iv) extensive water purification procedures are not required.

2.1.3 Anion Exchange Membrane Water Electrolyser (AEMWE)

In order to further decrease the internal resistance of the electrolysers and to operate the cells at a high pressure, the possibility of using a non-porous membrane with high anionic conductivity has also been studied [23]. Porous catalyst layers are deposited on each side of the membrane to form a membrane–electrodes assembly (MEA) very similar to what currently used in PEMWE [23]. The main requirements of OH^--conducting membranes are as follows:

- excellent mechanical and thermal stability in contact with water and during operations;
- insulator regarding electronic conductivity;

- efficient transfer of OH^- (hydroxide) ions from one electrode compartment to the other (high ionic conductivity);
- very low permeability to gases to minimize or even eliminate gas crossover between the anodic and cathodic compartments; and,
- low cost [23].

Some anion exchange membranes (AEM) are commercially available. However, the mobility of the hydroxide ion is approximately 15 times lower than that of the hydronium ion in proton-conducting membranes, and it is not straightforward to reach the conductivity offered by proton-conducting membranes [23]. Within the past 5 years, AEM conductivities have widely been reported to be in the 50-100 mS cm^{-1} range, with some even as high as 200 mS cm^{-1} [24, 25]. Moreover, many of these membranes still suffer from a lack of chemical stability at high-pH and high-temperature conditions, which is a critical issue that has prevented commercialization of AEMWE, since currently no AEM exists that can operate in the high-pH and high-temperature environments of AEMWE [24]. AEM is usually classified into three different categories [23]:

1. "Heterogeneous membranes" that are made of an anion exchange material embedded in an inert compound (relatively thick; 250-600 μm);
2. "Interpenetrating Polymer Networks" (or IPNs) that are a combination of two polymer networks without any covalent bonds between them; and
3. "Homogeneous membranes" where ionic conducting groups are covalently bonded to the polymer backbone and distributed homogeneously over the entire polymer matrix.

It should be noted that the development of a (thinner) membrane satisfying both chemical and mechanical stability, as well as performance requirements is only one of the limitations [23]. In AEMWE, the alkaline environment allows a greater variety of catalyst material selection, which could permit the use of non-precious metals for the HER and OER [24, 26]. The ability to use cheaper non-platinum or non-precious metal-based catalysts in AEMWEs is indeed very promising.

2.1.4 Solid Oxide Electrolyser (SOEL)

In solid oxide electrolysers (SOELs), oxide-ion conducting ceramics are used both as the solid electrolyte and the cell separator. The operating temperature for the SOELs is usually in the 800-1,000°C range, and they have a very high resistivity compared to PEMWEs and AWEs (around 30 Ω cm at 900-1,000°C). The electrolyte used in SOELs is generally zirconia

that has been stabilised with yttrium and scandium oxides [20, 27], with the main components of the SOEL consisting of stainless-steel bipolar plates and manganite-coated stabilized zirconia as the solid electrolyte. In the SOEL, water molecules are reduced at the cathode, as shown in equation (2.7):

$$H_2O_{(g)} + 2e^- \rightarrow H_{2(g)} + O^{2-} \quad (2.7)$$

The resulting oxygen ions can then migrate to the anode, where O_2 evolves as shown in equation (2.8):

$$O^{2-} \rightarrow \frac{1}{2}O_2 + 2e^- \quad (2.8)$$

Therefore, the overall reaction in an SOEL is shown in equation (2.9):

$$H_2O \rightarrow H_2 + \frac{1}{2}O_2 \quad (2.9)$$

The oxide ions are transported from the cathode to the anode across the zirconia electrolyte by an ionic diffusion process. To reduce the ohmic losses of ceramic membranes, the latter are typically very thin (ca. 30-150 μm thick). The favourable utilisation of SOEL technology is due to the possibility of operating SOELs at high current densities (e.g., a current density of 3.6 A cm^{-2} at 1.48 V and 950°C) and efficiencies [28]. In addition, the electrochemical processes are entirely reversible because SOELs are run at high operating temperatures. This allows a single SOEL unit to operate as either a fuel cell or an electrolysis cell.

2.1.5 Proton Conducting Ceramic Electrolyser (PCCEL)

A proton conducting ceramic water electrolyser (PCCEL) operates similarly to a SOEL, but the main difference is that in PCCEL, water vapour is supplied to the oxygen electrode side (anode), and the pure H_2 is generated at the cathode without dilution owing to the supplied water vapour [29]. The cathode in both a SOEL and a PCCEL is typically made of Ni in electrolyte composite (cermet). The oxidation and agglomeration of Ni at the cathode is avoided since the water vapour is supplied to the anode in a PCCEL [30, 31]. In addition, the intermediate operating temperatures of PCCEL (around 500°C) bring economic advantages. The required electrical energy for water electrolysis decreases as the operating temperature increases, since a significant portion of the energy supplied is in the form of thermal energy [32]. Because PCCELs operate at elevated temperatures, the sluggish kinetic issues at low temperatures are offset by the elevated operating temperatures. Therefore, PCCELs substantially enable water electrolysis with higher efficiency than room temperature operating

a PEMWE [29]. Although the first demonstration of PCCEL technology was reported in 1981 [33], its development has been slow due to the technical difficulty associated with the fabrication of the bilayer structure in the configuration of thin and dense electrolyte/porous electrode support [29].

2.2 Fundamentals of HER

2.2.1 Thermodynamics of HER

The overall process for the HER is represented in equation (2.10). Under standard conditions (i.e., p_{H_2}= 1.00 bar), the potential of H^+(aq)/H_2(g) redox couple is given by the *Nernst* equation (equation (2.11)) [34].

$$H^+(aq) + e^- \rightleftarrows \frac{1}{2}H_2(g) \tag{2.10}$$

$$E = E^o - \frac{RT}{F}\ln\left(\frac{\sqrt{f(H_2)/p^o}}{a(H^+)}\right) \tag{2.11}$$

where E^o is the standard potential of the H^+(aq)/H_2(g) redox couple (its value is zero at any temperature), f(H_2) is the fugacity of H_2(g) in bar, p^o is the standard pressure (p^o = 1.00 bar), a(H^+) is the activity of H^+(aq), F is the Faraday's constant (96,489 C mol^{-1}), R is the universal gas constant (8.314 J mol^{-1} K^{-1}) and T is the absolute temperature (K). Substitution of the equations for the fugacity of H_2(g) (equation 2.12) and the activity of H^+(aq) (equation 2.13) leads to equation (2.14) [34]:

$$f = \varphi p \tag{2.12}$$

$$a = \gamma\frac{m}{m^o} \tag{2.13}$$

$$E = E^o - \frac{RT}{F}\ln\left(\sqrt{p(H_2)\varphi(H_2)/p^o}\right) + \frac{RT}{F}\ln(m(H^+)\gamma_\pm/m^o) \tag{2.14}$$

where p(H_2) is the pressure of H_2(g) in bar, ϕ(H_2) is the fugacity coefficient of H_2(g), m(H^+) is the molality of H^+(aq), $\gamma_\pm$ is the mean activity coefficient of H^+(aq), and m^o is the standard molality (m^o = 1.00 mol kg^{-1}). If f(H_2) = 1.00 bar and a(H^+) = 1.00, $E = E^o$ and the hydrogen reference electrode is the standard hydrogen electrode (SHE). However, as soon as at least one of these parameters is not unit, the hydrogen reference electrode is the reversible hydrogen electrode (RHE) and its potential deviates from that of the SHE according to equation (2.11) [34].

The *Nernst* potential (E) in equation (2.11) is pH-dependent and as the pH increases the value of E decreases 0.0592 V (59.2 mV) per pH unit (equation 2.15). The pH dependence can be annulled when referenced to a reversible hydrogen electrode (RHE). On the RHE scale, the *Nernst* potential for HER is equal to zero regardless of the electrolytes in use [34, 35].

$$E = E^{o} - \frac{RT}{F}\ln\left(\frac{\sqrt{f(H_2)/p^o}}{a(H^+)}\right) = -0.0592 \times \text{ pH V } vs.\,\text{SHE} = 0.000\text{ V } vs.\,\text{RHE} \quad (2.15)$$

In practice, HER is not initiated at its equilibrium potential. This can be realized as most electrochemical processes must overcome a certain activation energy barrier to proceed. The total cell voltage (V_{cell}) for water splitting is shown in equation (2.16); where, E_{a} is the anode potential for the oxygen evolution reaction (OER), E_{c} is the cathode potential for the hydrogen evolution reaction (HER), I is the current, ΣR is total ohmic resistance, ΔE^{rev} is the reversible cell voltage, η_{a} is the anode overpotential and, η_{c} is the cathode overpotential [36].

$$V_{cell} = |E_c - E_a| + I \times \sum R = \Delta E^{rev} + |\eta_a| + |\eta_c| + I \times \sum R \quad (2.16)$$

The total ohmic resistance caused by the presence of the gas bubbles in the solution and at the electrode surface and flow of current in ionic electrolyte [35] of water electrolysis is expressed in equation (2.17) [36].

$$\sum R = R_e + R_m + R_b + R_c \quad (2.17)$$

where, R_{e} is the electrolyte resistance, R_{m} is the membrane or separator resistance, R_{b} is the bubble resistance, and R_c is the circuit resistance. R_{m} and R_{c} are constant in an electrolytic cell, which can be minimized by optimizing the wire connection and production process of the membrane or separator. The dispersion of the bubbles in the solution decreases the electrolyte conductivity and increases R_{e}. In addition, the bubble coverage on the electrode surface acts as a shield for the electric field, leading to high bubble resistance (R_{b}) [36, 37].

2.2.2 Kinetics of HER

The kinetics of the HER is simply based upon microkinetic analyses and can be described by: (i) the dependence of the Tafel slope (b); and, (ii) the Butler-Volmer equation

(BVE) [38]. Theoretically, simple electrochemical redox reactions can be described by the Butler-Volmer equation (2.18) [38, 39].

$$j = j_o \left\{ \exp\left[(1-\alpha)\frac{F}{RT}\eta\right] - \exp\left(-\alpha\frac{F}{RT}\eta\right)\right\} \quad (2.18)$$

where, η is the overpotential, which is the difference between the electrode (E_{app}) and reversible potentials (E^{rev}) expressed as $\eta = E_{app} - E^{rev}$, j is the net current density (A cm^{-2}), α is the transfer coefficient, F is the Faraday's constant (96,489 C mol^{-1}), R is the universal gas constant (8.314 J mol^{-1}K^{-1}), T is the absolute temperature (K); and, j_o is the exchange current density (A cm^{-2}). Equation 2.16 represents the total currents from both the reduction and oxidation reactions.

For practical purposes, it is convenient to consider the limiting behaviour of the BVE for small and large values of the arguments of the exponential terms. Experimentally, two limiting forms of Butler-Volmer equation are used to obtain Tafel equations [39, 40]. For small values of overpotential (i.e., when $\eta \to 0$), the exponential terms can be written as Taylor expansions (i.e., $\exp(x) \to (1+x)$). Therefore, the BVE becomes:

$$j = j_o(\frac{F}{RT})\eta \quad (2.19)$$

At large positive overpotentials (i.e., when $\eta \to +\infty$ i.e., $\exp\left[\left(\frac{-\alpha F}{RT}\right)\eta\right] \to 0$), then the Butler-Volmer equation can be approximated to:

$$j = j_o \left\{ exp\left[\left((1-\alpha)\frac{F}{RT}\right)\eta\right]\right\} \quad (2.20)$$

or

$$\log(j) = \log(j_o) + \frac{(1-\alpha)F}{(2.303RT)}\eta \quad (2.21)$$

or

$$\eta = -2.303\,\frac{RT}{(1-\alpha)F}\log(j_o) + 2.303\frac{RT}{(1-\alpha)F}\log(j) \quad (2.22)$$

At large negative overpotentials (i.e., $\eta \to -\infty$), the Butler-Volmer equation can be approximated to:

$$j = -j_o \left\{ exp\left[\left((-\alpha) \frac{F}{RT} \right) \eta \right] \right\} \quad (2.23)$$

or

$$\log(|j|) = \log(j_o) - \frac{\alpha F}{(2.303RT)} \eta \quad (2.24)$$

or

$$\eta = 2.303 \frac{RT}{\alpha F} \log(j_o) - 2.303 \frac{RT}{\alpha F} \log(|j|) \quad (2.25)$$

The plot of the logarithm of the current density vs. the overpotential (log j vs. η) is called a Tafel plot (equation 2.26). The slope allows the determination of the transfer coefficient (α) and the intercept at $\eta = 0$ gives the exchange current density (j_o).

$$\eta = a + b \log(j) \quad (2.26)$$

The Tafel slope provides insight into the reaction mechanism, and the exchange current density are known as descriptors of the catalytic activity. Therefore, for analysing electrochemical performances, the Tafel analysis is conjugated with the Butler-Volmer equation in many studies [38]. Tafel slope is commonly used to discern the rate-determining step and possible HER reaction pathway as will be discussed in detail later.

2.2.3 Mechanisms of HER in acidic media

The HER kinetics are strongly influenced by its reaction pathway, which can be both catalyst-dependent and potential-dependent. Sometimes, more than one pathway can be simultaneously operative on a single electrocatalyst owing to the existence of different surface crystalline facets. The HER is generally described in two ways. The first is hydronium ion reduction (equation 2.27):

$$2H_3O^+ + 2e^- \rightleftharpoons H_2 + 2H_2O \qquad (E^o = 0.000 \text{ V } \textit{vs.} \text{ SHE}) \quad (2.27)$$

and the second is water reduction (equation 2.28):

$$2H_2O + 2e^- \rightleftharpoons H_2 + 2OH^- \qquad (E^o = -0.828 \text{ V } \textit{vs.} \text{ SHE}) \quad (2.28)$$

Hydronium ion reduction consists of three steps: the Volmer, Heyrovsky and Tafel steps [35, 38, 41]. There is a general agreement that HER in acidic media consists of two elementary steps. In the first step, a proton-coupled electron transfer at the catalyst surface yields an intermediate adsorbed hydrogen atom. This step is known as the discharge reaction or Volmer step:

$$H_3O^+ + e^- + M \rightleftharpoons M - H_{ads} + H_2O \qquad \text{(Volmer step)} \qquad (2.29)$$

where M denotes as an active site on the catalyst surface; and H_{ads} is adsorbed hydrogen. Subsequent hydrogen desorption proceeds through two possible pathways. The adsorbed hydrogen atom can react with another proton from the solution accompanied by a second electron transfer to form molecular hydrogen. This step is known as the electrochemical desorption reaction or Heyrovsky step:

$$M - H_{ads} + H_3O^+ + e^- \rightleftharpoons M + H_2 + H_2O \qquad \text{(Heyrovsky step)} \qquad (2.30)$$

The recombination reaction or Tafel step is the combination of two adsorbed hydrogen atoms to form molecular hydrogen:

$$2\,M - H_{ads} \rightleftharpoons 2M + H_2 \qquad \text{(Tafel step)} \qquad (2.31)$$

Although it is challenging to illustrate the exact mechanism on different HER electrocatalysts, the Tafel slope can be usually taken as an indicator of the rate-determining step (*rds*) and may provide some valuable insight into possible reaction pathways [35].

2.2.4 Mechanisms of HER in alkaline media

The activity of HER in alkaline media is about 2–3 orders of magnitude lower than that in acidic media, and the reaction is sensitive to the surface structures of catalysts [42]. One of the main differences between alkaline and acidic HER is that the proton concentration is drastically decreased so that the Volmer and Heyrovsky steps are likely to include water-dissociation step [42]:

$$H_2O + e^- + M \rightleftharpoons M - H_{ads} + OH^- \qquad \text{(Volmer step)} \qquad (2.32)$$

$$H_2O + e^- + M - H_{ads} \rightleftharpoons H_2 + OH^- \qquad \text{(Heyrovsky step)} \qquad (2.33)$$

where M is an active site on the catalyst surface; and, H_{ads} is an adsorbed hydrogen atom on an active site. In alkaline media, breaking the strong covalent H–O–H bond is mandatory rather than the weak covalent bond of H_3O^+. The rational design of electrocatalysts with good ability to dissociate water and binding hydrogen species can effectively improve alkaline HER performances. Based on the reaction pathway involved in the Volmer and Heyrovsky steps, four major factors might influence the alkaline HER performance, including [42]:

1. Water adsorption on active sites;
2. Water dissociation ability;
3. Hydrogen binding energy; and,
4. Adsorption strength of hydroxide ions (OH^-).

Water adsorption is the first step of hydrogen evolution in alkaline media, which is much weaker than H_3O^+ adsorption in acidic media. Therefore, an enhanced metal–H_2O bond can improve the subsequent HER performance.

2.3 HER on Platinum (Pt)

The HER kinetics is strongly dependent on various parameters such as the electrode material, the nature of the electrolyte and the crystalline nature and orientation of the electrode (i.e., single-crystal, polycrystalline or amorphous) [41]. Hydrogen adsorption and desorption on the electrode surface are two successive steps in HER electrocatalysis. However, these two steps compete in nature: a catalyst surface having too weak bonding strength with hydrogen atom cannot efficiently adsorb the reactant to initiate the HER; whereas a catalyst surface having too strong bonding strength would have difficulty in releasing the product toward the completion of the HER. Therefore, the "ideal" HER electrocatalysts should have well-balanced hydrogen adsorption and desorption properties [35]. This is entirely in line with the *Sabatier principle*, which states that in order to have high catalytic activity, the interaction between reactants and catalysts should neither be too strong nor too weak [43]. If the interaction is too weak, then there will be no reaction on the surface because it is difficult for the catalyst surface to bind the reactants. If the interaction is too strong, the catalyst active sites will be blocked by reactants, intermediates, or product molecules, leaving no active sites available for new reactant

molecules that would continue the reaction [35, 44]. The *Sabatier principle* usually gives rise to volcano curve when plotting the activity *versus* the M-H bonding energy for different metals. Figure 2.2 illustrates the relationship between the logarithm of the exchange current density ($\log(j_o)$) and the energy of hydride formation (E_{M-H}), which was observed by Trasatti [45] in the form of a "volcano" curve [44, 46]. According to Figure 2.2, the HER exchange current density changes by the electrode material, with Pt-group materials on the top of the volcano plot.

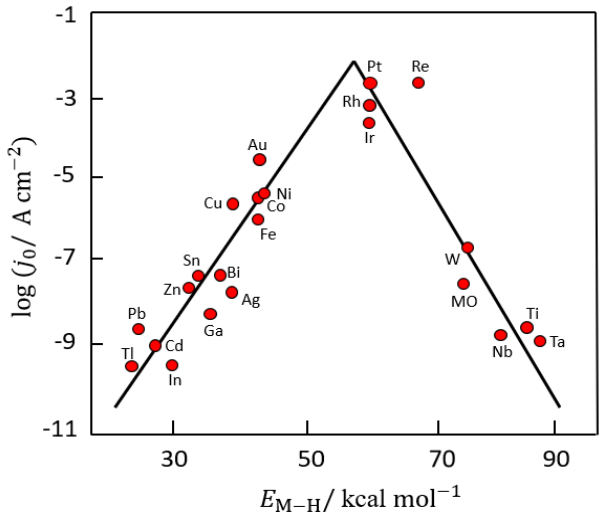

Figure 2.2. Trasatti's volcano plot for hydrogen evolution in acid solutions: dependence of the logarithm of the exchange current density (j_o) from the energy of hydride formation (E_{M-H}) [44, 46].

For platinum polycrystalline, experiments in acid solutions show that at low overpotentials the recombination reaction or Tafel step is rate-determining following the fast-initial discharge reaction or Volmer step. A Tafel slope b ~30 mV dec^{-1} is measured at this potential range. As the overpotential is increased, the coverage of absorbed hydrogen atoms approaches saturation. This leads to accelerated atom-atom recombination. As a result, the discharge reaction or Volmer step becomes rate-determining with a measured Tafel slope b ~120 mV dec^{-1} [35].

Based upon Conway *et al.* [47], Tafel slopes of 36–68 mV dec^{-1} at low overpotentials ($\eta \leq 0.05$) followed by 125 mV dec^{-1} at high overpotentials ~ $\eta > 0.075\ V$ in 0.5 M H_2SO_4 electrolyte for bulk Pt electrode have been reported. This indicates the Tafel slope is indeed

potential-dependent and, in turn, coverage dependent. Conway *et al.* [47] also showed that the Pt electrode becomes a poorer electrocatalyst for the HER as the cathodic polarization time increases. In the same paper, the Tafel plot for the same Pt electrode after 30 min cathodic polarization at ~ η = 0.050 V in 0.5 NaOH is a straight line with a slope of 125 mV dec^{-1} throughout the potential range measured. According to Conway *et al.* [47], the decrease of activity of the Pt electrode with time in alkaline solution is appreciably more rapid than in acid solution. Shinagawa *et al.* [38] confirmed that the Tafel slope measured for Pt electrodes in alkaline solutions is around 120 mV dec^{-1}, indicating that the Volmer or the Heyrovsky step is the *rds*.

2.4 HER on Nickel (Ni), NiO and $Ni(OH)_2$

Although Pt-based metals and alloys have been proven to show the best electrocatalytic activity towards the HER, their high cost and low abundance restrict their use in the industry on a large scale. Recently, many low-cost and effective electrocatalyst materials have been developed in order to reduce electrolysis cost [48-51]. Among these materials, Ni and its alloys exhibit excellent electrocatalytic activities and stabilities in alkaline solutions [48, 50, 51]. However, the reaction mechanism is not clear [50] due to the lack of a reliable *in-situ* method to directly measure the coverage of the hydrogen intermediate at the electrode/electrolyte interface, and oxidation of Ni in aqueous media [48]. Therefore, in the polarization curve, the "true" HER current is not easily differentiated from the overlapping electrochemical reduction of the oxide.

Furthermore, there are two crucial disadvantages associated with Ni-based electrodes in alkaline electrolysis: the first is a high operating cell voltage; and, the second is the decrease in cathodic activity with time [50]. Also, Ni has a weak ability to desorb OH^- species from the surface of the catalyst, which blocks the active sites to obstruct further water dissociation, so it has never been considered as a suitable HER electrocatalyst in alkaline media.

Nevertheless, the oxides and hydroxides of Ni are effective materials for breaking the HO−H bond and desorbing OH^- group [52]. Liang *et al.* [48] reported the "true" current of the HER in alkaline solution (0.01 M KOH) and directly measured the coverage of adsorbed hydrogen on the Ni electrode by interrogation scanning electrochemical microscopy (SI-SECM), which ensured the validity of the mechanistic analysis. They also provided evidence of the electrocatalysis of the Ni hydroxide. They confirmed that the presence of the surface oxide of low-valence state promotes the HER (e.g., dissociative adsorption of water); therefore,

the *rds* in the potential range between −0.95 and −1.10 V *vs.* Ag/AgCl (i.e., − 0.04 V *vs.* RHE and −0.19 V *vs.* RHE) observed in their study is Volmer step [48]. In another study by Zhu *et. al* [53], the electrocatalytic activity of Raney-Ni and a Ni mesh towards the HER in 30 wt% KOH were investigated. They obtained Tafel slopes of −127 and −122 mV dec^{-1} for a pure Ni mesh and Raney-Ni, respectively, and proved that the Volmer reaction is the *rds* of HER for pure net Ni [53]. Faid *et al.* [50] synthesized Ni, NiFe and NiCo metal oxide catalysts of different compositions by a simple co-precipitation method, and investigated the electrocatalytic performance of these catalysts towards the HER in 0.10 M KOH. All the catalysts in their study showed the same Tafel slopes of around 120 mV dec^{-1}, which indicates that the *rds* is the electrochemical adsorption of hydrogen (Volmer step).

To understand the electro-oxidation of nickel in alkaline solutions, we can refer to Alsabet and Jerkiewicz's works [54-56]. Alsabet *et al.* [54] investigated the electrochemical oxide growth on nickel in 0.5 M KOH. Figure 2.3 retrieved from Alsabet's paper illustrates cyclic voltammograms (CV) of polycrystalline Ni in 0.50 M KOH, and different potential regions correspond to formation and reduction of different oxides and hydroxide on Ni surface. The first CV (the red line) covers the potential range between −0.15 V *vs.* RHE and +0.50 V *vs.* RHE and corresponds to the formation (anodic) and reduction (cathodic) of α-$Ni(OH)_2$. The potentials of the anodic and cathodic peaks are +0.30 V *vs.* RHE and −0.05 V *vs.* RHE, respectively. The other two CVs cover the potential range between −0.15 V *vs.* RHE and +1.55 V *vs.* RHE; the blue and black CVs correspond to the first (1^{st}) and tenth (10^{th}) cycles and show the irreversible formation of β-$Ni(OH)_2$ + NiO; the reversible formation of β-NiOOH; and the potential of the anodic and cathodic peaks associated with the formation and reduction of NiOOH are +1.45 V *vs.* RHE and +1.36 V *vs.* RHE, respectively. The irreversible formation of β-$Ni(OH)_2$ from α-$Ni(OH)_2$ corresponds to a phase transition. In addition to the phase transition, the thickness of β-$Ni(OH)_2$ also increases through direct oxidation of the underlying Ni [54].

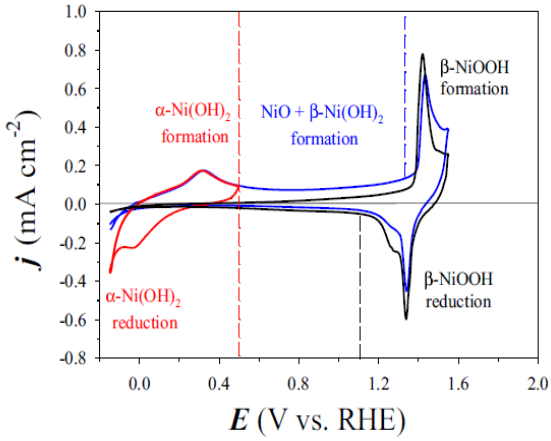

Figure 2.3. Three cyclic-voltammograms for Ni(poly) electrode in 0.5 M aqueous KOH solution obtained at a scan rate of 100 mV s^{-1} and T = 293 K. The first cyclic voltammogram (the red line) covers the potential range between –0.15 V and +0.50 V. The two other cyclic voltammograms cover the potential range between –0.15 V *vs.* RHE and +1.55 V *vs.* RHE; the blue and black cyclic voltammograms refer to the first (1^{st}) and tenth (10^{th}) cycles. The profiles correspond to the regions of reversible formation of α-$Ni(OH)_2$, irreversible formation β-$Ni(OH)_2$ + NiO, and reversible formation β-NiOOH [54].

Alsabet and his co-workers [54-56] proposed a general scheme illustrating relationships between metallic Ni and various O-containing surface compounds formed during anodic oxidation of polycrystalline Ni in aqueous alkaline media (Figure 2.4). Mild anodic polarization of metallic Ni results in the reversible formation of α-$Ni(OH)_2$; moderate anodic polarization results in the irreversible conversion of α-$Ni(OH)_2$ into β-$Ni(OH)_2$ as well as in the direct oxidation of Ni to β-$Ni(OH)_2$; and, this process is accompanied by the development of NiO that is sandwiched between Ni and β-$Ni(OH)_2$ (marked as a NiO sandwich in Figure 2.4). The purple lines and the formation of γ-NiOOH were suggested by Bode [57].

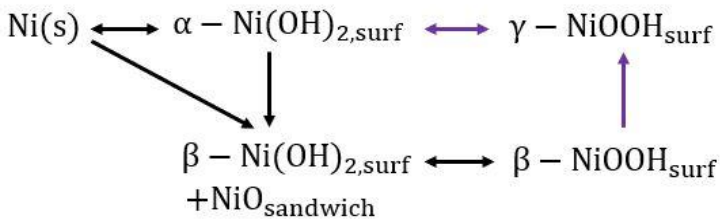

Figure 2.4. Schematic diagram of relationships between metallic Ni and various O containing surface compounds formed during anodic oxidation of polycrystalline Ni in aqueous alkaline media [54].

Krstajic *et al.* [58] observed that the mechanism of the HER in 1.0 M NaOH can switch from the Volmer-Tafel mechanism at $-0.200 < \eta < 0.000$ V *vs.* SHE ($-1.026 < \eta < -0.826$ V *vs.* RHE) to the Volmer-Heyrovsky one at $\eta < -0.200$ V *vs.* SHE ($\eta < -1.026$ V *vs.* RHE). The changing of the mechanism in different overpotential regions most likely reflects the changes in the surface composition of the Ni electrode at different hydrogen overpotentials [59]. In this regard, Oshchepkov *et al.* [60] investigated the effect of the oxidation of polycrystalline Ni electrodes on the kinetics of HOR and HER in alkaline solution (0.10 M NaOH) by combining cyclic voltammetry studies with microkinetic and X-ray photoelectron spectroscopy (XPS). They observed an increase of almost 10 times the activity of Ni in the HOR/HER after its oxidation under air atmosphere and assigned to the presence of NiO species on the surface of metallic Ni. Based upon their observations, the presence of a surface oxide affects not only the rate of HER/HOR, but also its mechanism. While on metallic Ni the HER/HOR follows the Heyrovsky-Volmer mechanism; however, on the activated electrode where Ni metal sites co-exist with the "irreversible" surface oxide species, the HER/HOR follows the Tafel-Volmer mechanism. We can explain this feature by the theory that hydrogen is strongly adsorbed on Ni, which may be considered as one of the reasons for its lower HOR/HER activity compared to Pt [60, 61]. However, the presence of adsorbed oxygen atoms leads to a decrease in the binding energies of Ni–H_{ad} and Ni–OH_{ad} [60, 62]. So the presence of NiO on the surface may enhance the activity of Ni towards the HOR/HER by decreasing the hydrogen adsorption energy [60]. It has also been confirmed that several layers of NiO covered by α-$Ni(OH)_2$ form on metallic Ni after contact with air [63]. They found that by applying a potential where hydrogen evolution occurs, air-formed NiO/α-$Ni(OH)_2$ can be easily reduced. However,

prolonged contact of α-$Ni(OH)_2$ with alkaline or even water solution leads to its transformation into β-$Ni(OH)_2$, which cannot be fully reduced even by applying a strong cathodic polarization. Therefore, β-$Ni(OH)_2$ blocks the surface and leads to a decrease in the activity of Ni electrodes toward the HOR/HER [63]. Jerkiewicz and Greden [64], investigated the effect of chemical etching on the kinetics of the HER on bulk and porous nickel materials. Interestingly, their results are inconclusive with regard to the influence of the surface roughness of Ni materials on the kinetics of the HER. They suggested that the surface oxide/hydroxide is catalytically less active than the metallic Ni, since it imposes a barrier to the charge transfer and changes the adsorption behaviour of the reaction intermediates and products. As chemical etching removes surface oxide/hydroxide layer, they observed better electrocatalytic performance of chemically etched Ni toward the HER, compared to a polished Ni rod and a Ni foam. In the case of Ni foam, the surface treatment also affects the activation energy.

2.5 Parameters affecting the HER

The hydrogen evolution reaction depends upon different parameters for instance effect of concentration, pH, temperature, etc. Many researchers have investigated their influences on the electrocatalytic activity of HER on Pt, Ni, and their oxides [65-70]. In this section, we are only reviewing very recent works on the topic.

2.5.1 Effect of pH on the HER

The effect of pH on the catalytic activity of proton−electron transfer reactions (such as HER/HOR), is a long-standing question. Lamoureux *et al.* [71] presented a microkinetic model that shows with increasing pH, the proton donor changes from hydronium to water (Figure 2.5). Their model suggests that the intrinsically larger barriers for the splitting of water with respect to hydronium are the cause of HER kinetics being slower in alkaline than in acidic media. Because an increase in pH corresponds to a decrease in hydronium activity and an increase in hydroxide activity, the activation barriers for steps with H_3O^+ as a reactant increase with increasing pH, while activation barriers for steps with OH^- as a reactant decrease with increasing pH [71].

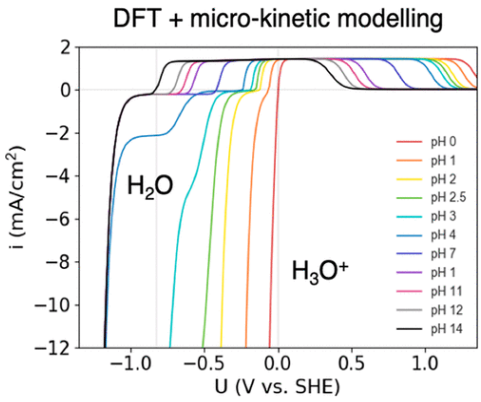

Figure 2.5. Computed HER/HOR polarization curves using the DFT and microkinetic modelling [71].

It has been suggested that the hydrogen binding energy (HBE) changed with pH and the origin of the pH-dependent HOR/HER activity was related to the increase of the HBE energy with pH [72]. The pH-dependent peaks in the underpotential deposition (H-upd) region of cyclic voltammetry (CV) measurements on polycrystalline Pt were taken as a measure of the HBE to establish this hypothesis [72]. In this regard, Sheng *et al.* [72] correlated the HER/HOR activity to HBE on polycrystalline Pt at different pH. They determined the HBE of Pt from cyclic voltammograms and found them to increase with pH, while the HOR/HER activity decreases with pH. They propose that the alkalinity (i.e., OH^- in the solution) changes the HBE and consequently affects the HOR/HER activity. Figure 2.6 [72] illustrates the CVs of Pt in selected buffered electrolytes in their study with solution pH ranging from 0 to 13. The peak at the lower potential in the H-upd region (E_{peak}) corresponds to the H-adsorption/desorption at the Pt(110) surface region (weakly bonded H), and the one at higher potential relates to the same process at Pt(100) (strongly bonded H) [73]. Both peaks shifted positively by +0.15 V *vs.* RHE when the solution pH changed from 0 to 13 [72]. Zheng *et al.* [74] also observed a common linear correlation between hydrogen binding energy (HBE) and pH for four platinum-group metal catalysts (Pt/C, Ir/C, Pd/C, and Rh/C) over a wide pH range (0 to 13) suggesting that the pH dependence of HBE is independent of metal type. They also indicated that the $\log(j_o)$ of all four catalysts decreases monotonically with pH. Since the HBE of the four metals increases with pH, it can be confirmed that higher HBE leads to lower HOR/HER activities; therefore, providing strong evidence supporting HBE as the dominant performance descriptor for HOR/HER catalysts [74].

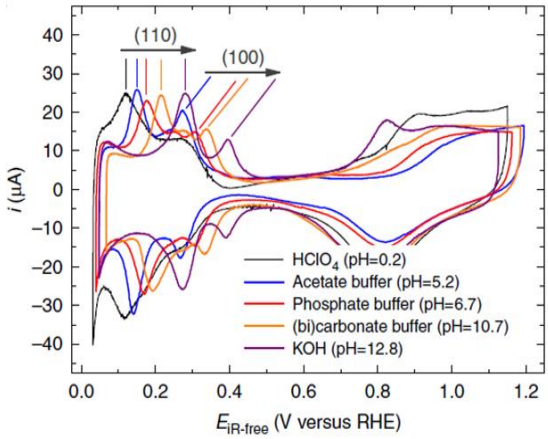

Figure 2.6. Cyclic voltammograms of Pt in Ar-saturated electrolytes at a scan rate of 50 mVs^{-1} [72].

Koper *et al.* [75, 76] proposed the potential of zero free charge (pzfc) theory for the pH-dependent HER rates of all Pt surfaces. Based upon this theory, the E_{peak} shifts with pH the same way as the pzfc for both extended and stepped Pt surfaces. As the pzfc shifts positively with increasing pH, the HER potential is more negative to the pzfc, leading to larger reorganization energy of interfacial water to reshuffle OH^- throughout the double layer. Subsequently, the energy barrier of the Volmer step for Pt surfaces increases with pH. The pzfc theory is in agreement with the Frumkin effect [77], wherein the adsorption of cations positively shifts the potential of the outer Helmholtz layer, thereby promoting the reactions involving the transport of anions, such as the Volmer step in the base [78].

In another study, Markovic *et al.* [79, 80] proposed the bifunctional theory and attributed the Ni-induced enhancement of the HER rate of Pt(111) to the bifunctional mechanism wherein the surface Ni species enhance H_2O dissociation for the HER. Unlike the HBE theory, both the bifunctional and the pzfc theories require the second metal to be present on the surface to promote the alkaline HER [78].

In contrast to noble metals, non-noble metals are chemically unstable in acidic media and investigations of the pH-dependence of the HOR/HER kinetics can be carried out only in a restricted pH window. Therefore, the influence of pH on the HOR/HER rate was rarely studied on non-noble metal electrodes such as Ni, which is considered as one of the most promising catalysts for HER in alkaline media [81]. Kuznetsov *et al.* [82] presented a kinetic study of the HOR/HER on Ni electrodes in the pH range from 12 to 14. They illustrated that

on pure metallic Ni, the experimental current-potential curves remain almost unchanged with pH when plotted on the RHE scale. In contrast, they observed a HOR/HER activity decrease with pH on partially oxidized Ni electrodes similar to noble metal electrodes. The analysis of the current-potential curves and kinetic modelling suggests that pH does not affect the H_{ad} and OH_{ad} binding energies on Ni. Therefore, the pH effect on HER/HOR activity on partially oxidized Ni cannot be explained by a change of the H_{ad} and OH_{ad} binding energies, but it can be explained by a decrease of the rates of Volmer and Heyrovsky steps with pH [83]. Faid *et al.* [50] also investigated HER activity of $NiFe_2O_4$ and $NiCo_2O_4$ compositions at different pH from 11 to 14. They observed that the polarization curves are dependent on the solution pH, and the current consistently increases with decreasing pH at a constant potential.

2.5.2 Effect of Acidic and Base Concentrations on the HER

Koster *et al.* [84] used dynamic multi-frequency analysis (DMFA) to investigate the reaction kinetics of HER at polycrystalline Pt electrodes in different concentrations of diluted $HClO_4$ (from 2 to 20 mM). They investigated the kinetic parameters and their quantification by an equivalent circuit based upon the Volmer-Tafel mechanism. Figure 2.7 [84], illustrates CVs of polycrystalline Pt at different $HClO_4$ concentrations. As can be seen in Figure 2.7, the maximum of the cathodic current densities linearly increases with the concentration of the acid, which is due to the diffusion limitation in solution. After the current peak, the rate of HER is fully controlled by mass transport phenomena. At a potential of +0.03 V *vs.* RHE, an anodic current density peak is observed, where the electro-oxidation current increases with increasing electrolyte concentrations due to the presence of the larger amounts of previously formed H_2.

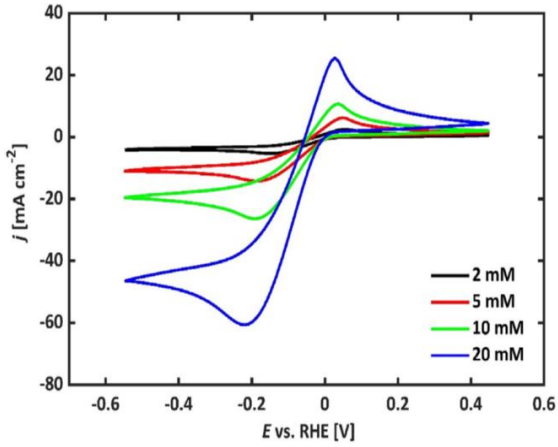

Figure 2.7. Cyclic voltammograms of Pt polycrystalline in different concentration of $HclO_4$ at a scan rate of 100 mV s^{-1} [84].

Figure 2.8, from Koster's paper [84], shows the measured (dots) and fitted (lines) impedance spectra in the different electrolyte concentrations in a potential range between −0.2 and 0.0 V *vs.* RHE (cathodic scan direction), where H_2 evolution occurs. The intermediate semi-circle was attributed to the Volmer step (adsorption resistance), which decreases in radius with higher electrolyte concentrations and more cathodic potentials. At low frequency, all spectra show a straight line that can be attributed to the diffusion-controlled adsorption of hydronium ions. The higher the concentration of the electrolyte and the more negative the potential, the steeper the slope because of the lower effect of diffusion on the electro-sorption process. The high-frequency region is a fraction of a semicircle that cannot be related to a specific phenomenon. This feature becomes particularly dominant when the electrolyte concentration is low and partially overlaps with the Volmer step. In general, with increasing the electrolyte concentration, the overall impedance decreases due to an increase in ionic conductivity.

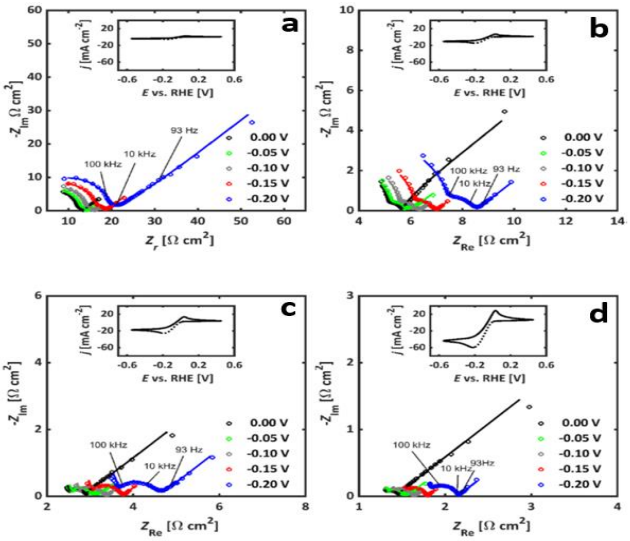

Figure 2.8. Dynamic impedance spectra of Pt polycrystalline in different concentration of $HClO_4$ (squares) and their corresponding fitted spectra (solid lines) at different potentials in the HER region. (a) 2 mM $HClO_4$; (b) 5 mM $HClO_4$; (c) 10 mM $HClO_4$ and (d) 20 mM $HClO_4$ [84].

2.5.3 Effect of Temperature on the HER

2.5.3.1 Effect of Temperature on the Kinetics of HER on Nickel

The temperature effect on HER has been discussed by many groups [58, 85-88], and the common observation is that the HER rate increases when the temperature is increased. A suitable parameter to determine the catalytic activity is the apparent activation energy (E_a) at equilibrium potential. The lower the activation energy is, the lower the energy requirements for hydrogen production [89]. The exchange current density is related to the activation energy by the *Arrhenius' law* as represented in equation (2.34) [89]:

$$\log(j_o) = A' - \frac{E_a}{2.303R} \times \frac{1}{T} \tag{2.34}$$

where j_o is the exchange current density (A cm^{-2}); A' is the *Arrhenius* pre-exponential factor; R is the universal gas constant (8.314 J mol^{-1} K^{-1}); T is the absolute temperature (K); and E_a is the apparent activation energy (J mol^{-1}). Equation (2.74) shows that $\log(j_o)$ can be plotted against $1/T$. If a straight line is obtained, the activation energy (E_a) can be determined from the slope [89].

The apparent activation energies for HER on polycrystalline Ni reported by various researchers differ strongly due to the differences in the electrode pre-treatment procedures as they ignore the influence of the (partial) oxidation of the Ni electrode on the HER kinetics [85]. The influence of the temperature on the Ni oxidation kinetics should be considered since the latter significantly affects the HOR/HER kinetics even at small overpotentials [85]. Alsabet *et al.* [54] investigated the electrochemical growth of surface oxide on Ni as a function of temperature. Figure 2.9 [54] shows CVs for polycrystalline Ni electrode obtained at the potentials between +0.50 and +1.55 V *vs.* RHE in 0.5 M KOH at four temperatures in the 281 $\leq T \leq$ 313 K range. As it can be observed, the increase of temperature by 32 K shifts the anodic peak towards lower potentials; however, this does not affect the cathodic peak potential. The results also illustrate that the current density of the anodic peak increases significantly, while the current density of the cathodic peak rises only slightly. The significant increase in the anodic peak corresponds to the formation of β-NiOOH, possibly due to two phenomena occurring concurrently in this potential range (i.e., the formation of β-NiOOH and the OER).

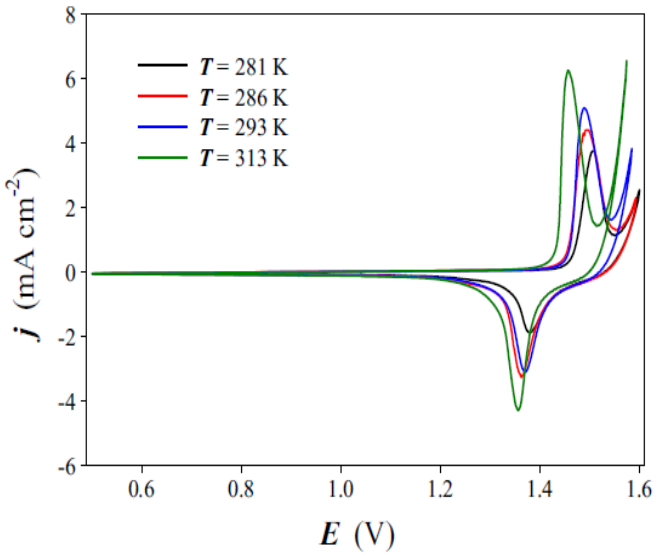

Figure 2.9. Cyclic voltammograms for polycrystalline Ni electrode in 0.5 M KOH at a scan rate of 100 mV.s^{-1} and in the 0.50–1.55 V vs RHE range at four temperatures in the 281 ≤ T ≤ 313 K range [54].

Oshchepkov *et al.* [85] studied the influence of the temperature on the kinetics of the HOR/HER for a freshly polished metallic Ni rod (non-activated Ni) and an electrochemically partially oxidized Ni rod (EC-activated Ni) electrodes. The surface of EC-activated Ni rod is partially covered by NiO or β-Ni(OH)$_2$. They investigated the complex interaction between the hydrogen electrode reactions and Ni hydroxide adsorption/desorption overlapping in a wide range of potentials as a function of temperature. Figure 2.10 [85] shows the cyclic voltammograms of non-activated Ni and EC-activated Ni at different temperatures. The anodic a_1 and the cathodic c_1 peaks correspond to the Ni/α-Ni(OH)$_2$ redox transition [56, 90] and the a_2 peaks related to the existence of metallic Ni sites on the surface of EC-activated Ni rod.

It can be seen that the maximum of the anodic a_1 peak shifts towards negative potentials with temperature for both electrodes, although this shift is much more pronounced in the case of EC-activated Ni compared to non-activated Ni. The maximum of the cathodic c_1 peak shifts towards positive potentials in the case of EC-activated Ni electrode while it is almost constant for non-activated Ni. Based upon their study, on non-activated Ni rod, the Tafel slope of the HER increases from 115 to 129 mV dec^{-1}, which is related to the change in the (RT/F) term in the Tafel equation [58, 91]. The value of the apparent charge transfer coefficient for the HER on a non-activated Ni rod is almost independent of the temperature, varying between 0.51 and

0.54 over the temperature range of their study. In contrast, the Tafel slopes of the EC-activated Ni rod are slightly influenced by the temperature, lying in the range of 125-130 mV dec^{-1} for the HER and the apparent charge transfer coefficient ranging from 0.47 to 0.51.

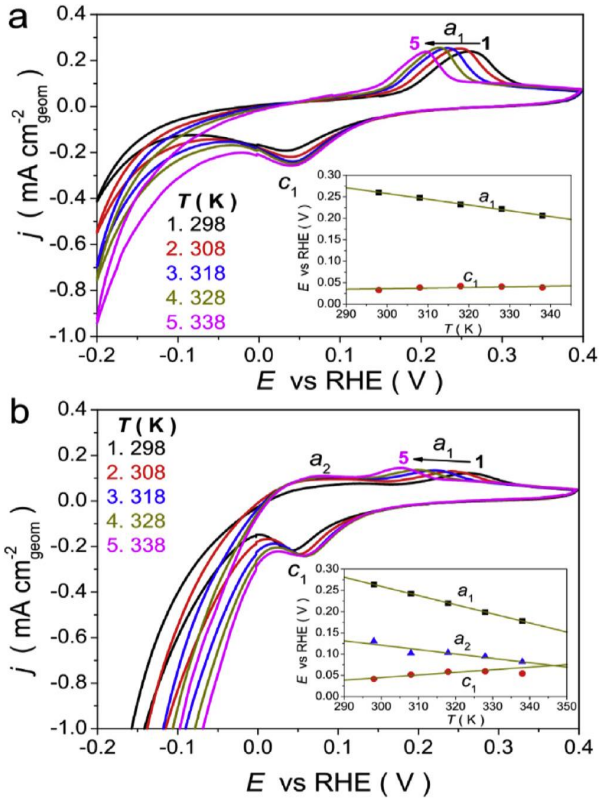

Figure 2.10. Cyclic voltammograms for the (a) non-activated and (b) EC-activated Ni rod were obtained in N_2-saturated 0.10 M NaOH at scan rate of 20 mV s^{-1} and various temperatures. Insets represent the shift of the potential of anodic (a_1: black squares, a_2: blue triangles) and cathodic (c_1: red circles) peaks with the temperature [85].

2.5.3.2 Effect of Temperature on the Kinetics of the HER on Platinum

Jerkiewicz *et al.* [92, 93] studied the temperature dependence of the cyclic voltammetry response for the Pt(hkl) electrodes in aqueous H_2SO_4 solution. Figure 2.11 [92, 93] indicates the following results. Figure 2.11a shows the CV transients for Pt(111) at temperature range $275 \leq T \leq 328$ K in 0.5 M H_2SO_4 solution. It can be seen that all three CV features (I, II and III) shift towards less-positive potentials upon T increase. The peak potential (E_P) of the sharp peak in the anion adsorption region is a linear function of T, and the slope of the relation is -0.27×10^{-3} V K^{-1} (inset in Figure 2.11a). Figure 2.11b shows the CV scans for Pt(100) at

temperature range $293 \leq T \leq 328$ K in 0.5 M H_2SO_4 solution. According to Figure 2.11b, the CV features shift towards less positive potentials upon T increase. The shift of the peak potential, E_P, of the CV feature corresponding to the anion adsorption, is linear as a function of T and its slope is -1.34×10^{-3} V K^{-1} (inset in Figure 2.11b). Figure 2.11c shows CV profiles for Pt(110) in 0.5 M H_2SO_4 solution at different temperatures in the $273 \leq T \leq 333$ K range (the temperature interval is $\Delta T = 10$ K). It was observed that upon increasing T, the peak at +0.114 V *vs.* SHE displaces towards less positive potentials and its current density decreases slightly and the voltammetric wave at +0.170 V *vs.* SHE becomes less pronounced upon increasing T and eventually disappears at 328 K. Inset in figure 2.11c reveals that E_p shifts towards less positive potentials upon an increase in temperature; the E_p versus T relation is linear and its slope, equals to -4.64×10^{-4} V K^{-1}.

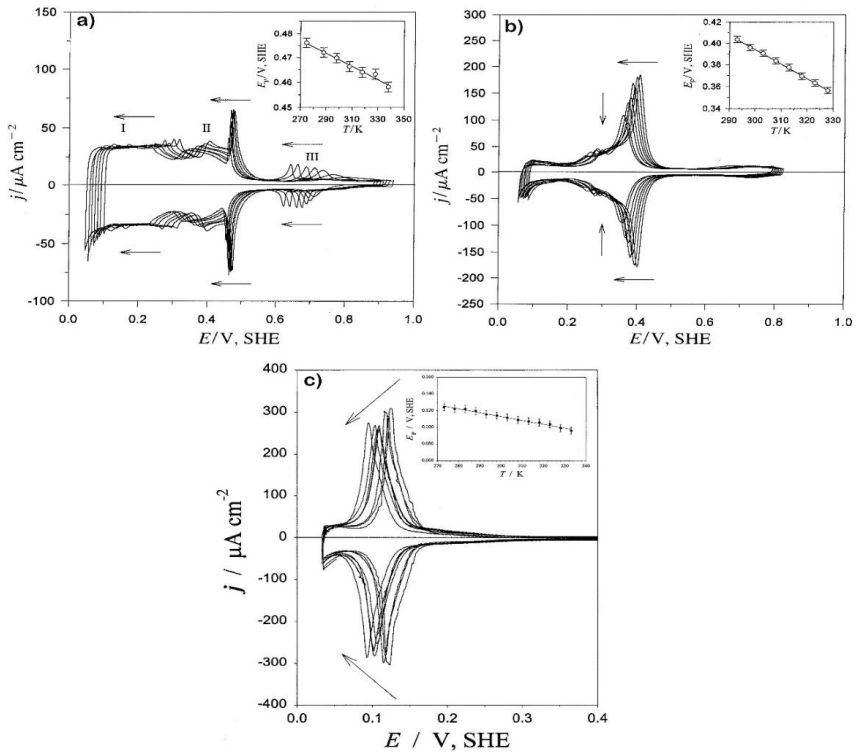

Figure 2.11. CV profiles for a) Pt(111) at $275 \leq T \leq 328$ K with the first interval equal to 13 K and the subsequent ones being 10 K, b) Pt(100) at $293 \leq T \leq 328$ K with an interval equal to 5 K, c) Pt(110) at $273 \leq T \leq 333$ K with an interval of 10 K; in 0.5 M aqueous H_2SO_4 solution at scan rate of 50 mV s^{-1}. Arrows indicate changes in the CVs associated with T increase. Inset shows the relation between the potential of the sharp peak (Ep) [92, 93].

2.6 Oxygen evolution reaction

2.6.1 Mechanisms of OER in acidic media

The reaction mechanism of oxygen evolution reaction (OER) is complicated, and it is known as a 2- or 4-electron step [38]. Basically, a four-electron pathway occurs on noble metals, and a two-electron pathway predominates on carbonaceous materials [94]. There are different proposed mechanisms for the OER on heterogeneous electrocatalysts, based upon kinetic studies or density function theories (DFT) calculations [95]. However, *rds* cannot be identified only based upon the Tafel slopes. Different *rds* in different mechanisms may result in similar Tafel slopes [16]. Furthermore, the Tafel slope itself is a somewhat unspecific measure that can be changed by different factors such as electrode material properties besides the electroanalytic reaction [95]. Bockris in 1956 [96] made up the kinetics model based upon the kinetics of activation controlled electrode reactions for different possible OER mechanisms, some of them are shown in equation (2.35) – (2.44). Each step in his model can be a *rds*.

a) The oxide path is as follows:

$$H_2O + M \rightleftharpoons MOH + H^+ + e^- \quad (2.35)$$

$$2MOH \rightleftharpoons MO + M + H_2O \quad (2.36)$$

$$2MO \rightleftharpoons 2M + O_2 \quad (2.37)$$

b) The electrochemical oxide path:

$$H_2O + M \rightleftharpoons MOH + H^+ + e^- \quad (2.38)$$

$$MOH \rightleftharpoons MO + H^+ + e^- \quad (2.39)$$

$$2MO \rightleftharpoons 2M + O_2 \quad (2.40)$$

c) The electrochemical metal peroxide path:

$$H_2O + M \rightleftharpoons MOH + H^+ + e^- \quad (2.41)$$

$$2MOH \rightleftharpoons MO + M + H_2O \quad (2.42)$$

$$MO + H_2O \rightleftharpoons MOOH + H^+ + e^- \quad (2.43)$$

$$2MOOH \rightleftharpoons MO + H_2O + O_2 + M \quad (2.44)$$

where M is a site on the surface.

Another possible mechanisms of OER in acid solutions based upon Suen's work is as follows [97]:

$$M + H_2O(l) \rightleftharpoons MOH + H^+ + e^- \quad (2.45)$$

$$MOH + OH^- \rightleftharpoons MO + H_2O(l) + e^- \quad (2.46)$$

$$2MO \rightleftharpoons 2M + O_2(g) \quad (2.47)$$

$$MO + H_2O(l) \rightleftharpoons MOOH + H^+ + e^- \quad (2.48)$$

$$MOOH + H_2O(l) \rightleftharpoons M + O_2(g) + H^+ + e^- \quad (2.49)$$

The similarity between all the mechanisms is the same intermediates such as MOH and MO, while the major difference among them is the reaction that forms oxygen. According to Suen's paper and Figure 2.12 [97], there are two different ways to form oxygen from MO intermediate. The first one is the green route in which two MO intermediates combine to produce O_2 (g), and the other one is the black route which involves the formation of MOOH following by the decomposition of MOOH to O_2 (g). Therefore, it is obvious that bonding reactions (M-O) within the intermediates (MOH, MO and MOOH) are critical for the overall electrocatalytic activity [97].

2.6.2 Mechanisms of OER in Alkaline Media

Alkaline OER is also a 4-electron–proton transfer process which makes the reaction sluggish with high overpotential and complex reaction mechanisms [42, 97]. Generally, mechanism of alkaline OER follow several steps. The schematic illustration is shown in Figure 2.12 [42, 97]. Firstly, M–OH forms from the 1-electron oxidation of adsorbed hydroxide anions on the active site. Then, M–OH converts to M–O after removals of electron and a couple of protons. After that, there are two possible pathways for M–O to produce O_2 molecules. On the one hand, two M–O species can combine and be transferred into O_2 and M active sites. On the other hand, M–O transferred into M–OOH after a hydroxyl anion is coupled, under 1-electron oxidation and then starts another proton-coupled electron transfer process, producing O_2 and the initial active sites [98]. Understanding details of this interaction between catalysts surface and OER intermediates is crucial for the overall OER performance improvement. However, it is difficult to completely understand the *rds* and confirm the kinetics of the OER due to the above multiple intermediates [42, 97].

Suen *et al.* propose a mechanism for OER in alkaline solution as following [97]:

$$M + OH^- \rightleftharpoons MOH \quad (2.50)$$

$$MOH + OH^- \rightleftharpoons OH + H_2O(l) \quad (2.51)$$

$$2MO \rightleftharpoons 2M + O_2(g) \quad (2.52)$$

$$MO + OH^- \rightleftharpoons MOOH + e^- \quad (2.53)$$

$$MOOH + OH^- \rightleftharpoons M + O_2(g) + H_2O(l) \quad (2.54)$$

Figure 2.12 demonstrates mechanisms of OER in both acidic (blue lines) and alkaline (red lines) solutions based upon Suen's paper [97]. By comparing the mechanisms of oxygen evolution in acid and base media, it is evident that the reactions in both acid and base involve similar intermediates and number of protons and electrons.

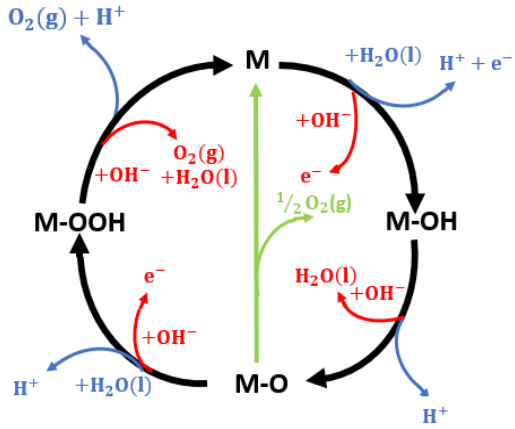

Figure 2.12. The OER mechanism in acid (blue line) and alkaline (red line) solutions. The black line illustrates the oxygen evolution involves the formation of a peroxide (M–OOH) intermediate, while another possible route for producing oxygen is the direct reaction of two adjacent oxo (M–O) intermediates (green line) [97].

2.7 OER on Pt

While Pt-based materials are the best ORR catalysts, they do not have good catalytic activity towards the OER, due to the formation of Pt oxides on the catalyst surface at high overpotentials [94]. According to the observation of Heitbaum *et al.* [99] only two-dimensional Pt surface oxide ($O = O$), which is a thin oxide layer, participates in the OER, while Pt(II) and/or Pt(IV) oxide layer does not take part in the OER in both acidic and basic media. Damjanovic in 1991 [100] proved that the OER activity of Pt is strongly dependent on the thickness of Pt oxide film. He also confirmed at any thickness and all potentials, the Tafel slopes of OER should always be greater than 120 mV dec^{-1} in acid solutions. Reier *et al.* [101] also investigated the OER activity of Pt bulk and Pt nanoparticles in 0.1 M $HClO_4$ and obtained

Tafel slopes of 145 mV dec^{-1} and 210 mV dec^{-1} for Pt bulk and Pt nanoparticles, respectively. Their results are completely in agreement with Damjanovic's findings. The experimentally observed high Tafel-slope illustrates additional contributions from processes with exponential current−potential dependency, probably related to the formation of Pt oxide layers [101].

Damjanovic in 1992 [102] reported the OER at Pt in alkaline solutions follows two *E*-log(*j*) relationships (Tafel behaviour). At low current densities Tafel slope of Pt is close to 60 mV dec^{-1}, and at high current density to 120 mV dec^{-1}. In both current density regions, the slopes are independent of the electrode potential. In the high current density region where the slope is 120 mV dec^{-1}, the reaction rates are strongly affected by the thickness of the oxide film anodically formed during electrode pre-treatment at high current density or at high electrode potentials [102]. In contrast, in the low current density region where the slope is 60 mV dec^{-1}, the rates are not affected by the film thickness. According to his observation, the kinetics in both current density regions are related to the presence of an oxide film at the electrodes. In alkaline same as in acid solutions, an anodic oxide, or hydroxide, film, 8-15 Å thick covers an electrode in the potential region of the OER [102]. These oxide films are electronic insulators [102, 103] and electrons required for the OER are transferred through the films by an electron tunnelling process [102]. He observed a decrease in the thickness of the oxide film in the rates in alkaline solutions at high current densities [102]. Experimental parameters at high and low current densities based upon Damjanovic's observations are summarized in Table 2.2 [102].

Table 2.2. Summary of kinetic parameters for the OER at Pt [102].

	b **(mV dec^{-1})**	***z***
Acidic solutions	$2.3\left(\frac{2RT}{zF}\right)$	1
Alkaline solutions at low current density	$2.3\frac{RT}{zF}$	1
Alkaline solutions at high current density	$2.3\left(\frac{2RT}{zF}\right)$	1

2.8 OER on Ni-based Materials in Alkaline and Acidic Media

Nickel-based materials are promising candidates for OER catalysis. Nickel hydroxide, which is the active component of nickel-based batteries, has been known as an OER catalyst for a long time [104]. Conway suggested that OER on nickel oxide (NiO) electrode in dilute alkaline solutions has two Tafel slopes of $2.3\frac{2RT}{5F}$ (23 mV dec^{-1}) or $2.3\frac{RT}{3F}$ (20 mV dec^{-1}) at low overpotentials, followed by Tafel slopes between $2.3\frac{2RT}{3F}$ (38 mV dec^{-1}) and $2.3\frac{RT}{F}$ (59 mV dec^{-1}) at high overpotentials [105]. Drunen *et al.* [106] synthesized Pt-modified Ni foam (Pt/Ni foam) and investigated the electrocatalytic activity of Pt/Ni foams toward OER, HER, ORR and HOR in 0.5 M KOH. According to their study, the analysis of OER on Pt/Ni foams differs from those for HER, HOR, and ORR because Ni materials are known to be more effective electrocatalysts toward this reaction than Pt. The Tafel polarization plot for Ni foam shows that there are two Tafel slopes, at the low overpotential region shows a moderate slope of 40 mV dec^{-1}, which is attributed to the formation of β-NiOOH in the $+1.20 \leq E \leq +1.55$ V *vs.* RHE range occurring concurrently with OER and affecting its rate and at high overpotential region the slope is very high and amounted to 320 mV dec^{-1}.

Ni-(oxy)hydroxide-based materials are promising earth-abundant catalysts for electrochemical water oxidation in alkaline media [107]. In this regard, Stern *et al.* [108] investigated the electrocatalytic activity of bulk and nanoparticle NiO_x and $Ni(OH)_2$ towards the OER in 1.0 M KOH. They prepared bulk $Ni(OH)_2$ catalyst by cathodic electrodeposition using a nickel nitrate ($NiNO_3$) solution, and bulk NiO_x catalyst was prepared *in-situ* during the CV measurements using a pre-treated nickel electrode. They observed that both catalysts exhibited a small redox wave attributed to a Ni(II)/Ni(III) redox process at potentials lower than the OER potentials. The current densities at > +1.5 V vs. RHE were attributed to the oxygen evolution activity. For the bulk $Ni(OH)_2$ catalyst, continuous CV scans increased the activity slightly, and the maximum activity was reached after five (5) CV cycles. They suggested that the *as*-deposited $Ni(OH)_2$ was quickly converted to NiOOH, which is the active phase of this catalyst in the OER region [107]. However, the NiOOH-based catalysts are weak catalysts towards the OER and an additional metal impurity such as iron (Fe) are required to improve their activity [107, 109], while according to Boettcher *et al.* [110] very small amount of Fe impurity is enough to enhance the catalytic activity of $Ni(OH)_2$.

Klaus *et al.* [107] investigated the influence of Fe impurities in the electrolyte on the OER activity of $Ni(OH)_2$ in 1.0 M KOH. Based upon their study, at potentials below the onset

of the OER, the catalyst was present as $Ni(OH)_2$ form, and before the onset potential of oxygen evolution, this phase was oxidized to NiOOH via reaction (2.55) [111].

$$Ni(OH)_2 + 0H^- \rightarrow NiOOH + H_2O + e^- \quad (2.55)$$

Recently, Baranova and her group [112, 113] showed that Ni-Fe catalysts enhance activity towards OER, and cerium oxide (CeO_2) supports have shown positive effects on catalytic performance. In their study, the iron and ceria content of a bimetallic NiFe with and without ceria catalyst was optimized to produce a highly active oxygen evolution reaction catalysts for applications in alkaline water electrolysis. Firstly, they studied the iron content for $Ni_{100-x}Fe_x$ / 50 wt% CeO_2 (x = 0, 5, 10, 20, 40at%); then, the ceria content is studied for the best two iron compositions, namely, $Ni_{80}Fe_{20}$/y wt% CeO_2 and $Ni_{90}Fe_{10}$/ y wt%CeO_2 (y = 0, 5, 7, 10, 20, and 50 wt%). Electrochemical characterization in 1 M KOH showed that at 10 mA cm^{-2}, the $Ni_{80}Fe_{20}$ catalyst achieved the lowest overpotential for OER of 269 mV, which is better performing than the iridium black benchmark, as well as similar NiFe materials reported in literature. Stability testing indicated that the $Ni_{90}Fe_{10}$ catalyst is the most stable material with almost no change in overpotential over 12 h at 10 mA cm^{-2}. Their study showed that the addition of CeO_2 to the catalysts does not significantly improve or impede OER activity.

Dai *et al.* [114] prepared Ni/$Ni(OH)_2$ nanosheets and evaluated the electrocatalytic activity of this catalyst toward OER in 1.0 M KOH. The Tafel slope of 70 mV dec^{-1} was obtained which was smaller than the Tafel slope of pure Ni (212 mV dec^{-1}) and pure $Ni(OH)_2$ (138 mV dec^{-1}). The overpotential at +10 mA cm^{-2} of +270 mV vs. RHE, +390 mV *vs.* RHE and +455 mV vs. RHE were obtained for Ni/$Ni(OH)_2$, $Ni(OH)_2$ and Ni, respectively. Recently, some researchers worked on the electrochemical properties of α-$Ni(OH)_2$ and β-$Ni(OH)_2$ towards the OER in alkaline solutions. Table 2.3 summarizes some of these works.

Table 2.3. Comparison of OER performance of the Ni hydroxide catalysts in alkaline electrolyte.

Material	Electrolyte	Overpotential at 10 mA cm^{-2} (mV)	Tafel slope ($mV\ dec^{-1}$)	Ref
α-$Ni(OH)_2$-NP	1.0 M KOH	260	78.6	[115]
α-$Ni(OH)_2$-NB	1.0 M KOH	320	92.4	[115]
α-$Ni(OH)_2$-MS	1.0 M KOH	320	98.7	[116]
α-$Ni(OH)_2$-NF	1.0 M KOH	340	105	[117]
α-$Ni(OH)_2$-NF	1.0 M KOH	400	161.8	[118]
α-$Ni(OH)_2$ spheres	0.1 M KOH	331	42	[119]
β-$Ni(OH)_2$ hexagonal NPs	0.1 M KOH	444	111	[119]
β-$Ni(OH)_2$	1.0 M KOH	331	47	[120]

NP, NB, MS and NF stand for sheet like, bud like, microsphere and flower like Ni, respectively.

References

[1] Lamb, J.J. and B. Austbø, *Current Use of Bioenergy and Hydrogen*, in *Hydrogen, Biomass and Bioenergy: Integration Pathways for Renewable Energy Applications*. 2020, Academic Press.

[2] Rytter, E., et al., *Thermochemical Production of Fuels*, in *Hydrogen, Biomass and Bioenergy: Integration Pathways for Renewable Energy Applications*. 2020, Academic Press.

[3] Lamb, J.J., et al., *Traditional routes for hydrogen production and carbon conversion*, in *Hydrogen, biomass and bioenergy: The hydrogen and bioenergy nexus in a renewable context*. 2020, Elsevier.

[4] Coutanceau, C. and S. Baranton, *Electrochemical conversion of alcohols for hydrogen production: a short overview.* Wiley Interdisciplinary Reviews: Energy and Environment, 2016. **5**(4): p. 388-400.

[5] Lamb, J.J. and B.G. Pollet, *Future prospects of selected hydrogen and biomass energy technologies*, in *Hydrogen, Biomass and Bioenergy: Integration Pathways for Renewable Energy Applications*. 2020, Academic Press.

[6] Lamb, J.J., et al., *Emerging technology for hydrogen and bioenergy production*, in *Hydrogen, Biomass and Bioenergy: Integration Pathways for Renewable Energy Applications*. 2020, Academic Press.

[7] Lamb, J.J. and K.M. Lien, *Promising Selected Biohydrogen Solutions*, in *Hydrogen, Biomass and Bioenergy: Integration Pathways for Renewable Energy Applications*. 2020, Academic Press.

[8] Lamb, J.J., *Upgrading Biogas to Biomethane*, in *Anaerobic digestion - from biomass to biogas*. 2020, SCIO Publishing. p. 299–332.

[9] Lamb, J.J., O.S. Burheim, and B.G. Pollet, *Hydrogen Fuel Cells and Water Electrolysers*, in *Micro-Optics and Energy*. 2020, Springer. p. 61-71.

[10] Wei, C., et al., *Recommended practices and benchmark activity for hydrogen and oxygen electrocatalysis in water splitting and fuel cells.* Advanced Materials, 2019. **31**(31): p. 1806296.

[11] Lamb, J.J., B.G. Pollet, and O.S. Burheim, *Energy storage.* Energy-smart buildings design: construction and monitoring of buildings for improved energy efficiency. , 2020. **1**: p. 1-14.

[12] Islam, M.H., et al., *Novel fuel production based on sonochemistry and sonoelectrochemistry.* ECS Transactions, 2019. **92**(10): p. 1.

[13] Karunadasa, H.I., C.J. Chang, and J.R. Long, *A molecular molybdenum-oxo catalyst for generating hydrogen from water.* Nature, 2010. **464**(7293): p. 1329-1333.

[14] Grigoriev, S., V. Porembsky, and V. Fateev, *Pure hydrogen production by PEM electrolysis for hydrogen energy.* International Journal of Hydrogen Energy, 2006. **31**(2): p. 171-175.

[15] Xing, L., et al., *Platinum electro-dissolution in acidic media upon potential cycling.* Electrocatalysis, 2014. **5**(1): p. 96-112.

[16] Gagliardi, G.G., et al., *Composite Polymers Development and Application for Polymer Electrolyte Membrane Technologies—A Review.* Molecules, 2020. **25**(7): p. 1712.

[17] Grigoriev, S., P. Millet, and V. Fateev, *Evaluation of carbon-supported Pt and Pd nanoparticles for the hydrogen evolution reaction in PEM water electrolysers.* Journal of Power Sources, 2008. **177**(2): p. 281-285.

[18] Hao, S., et al., *Dopants fixation of Ruthenium for boosting acidic oxygen evolution stability and activity.* Nature communications, 2020. **11**(1): p. 1-11.

[19] Coutanceau, C., S. Baranton, and T. Audichon, *Hydrogen Production From Water Electrolysis*, in *Hydrogen Electrochemical Production*

2017, Academic Press. p. 17-62.

[20] Millet, P. and S. Grigoriev, *Water electrolysis technologies.* Renewable Hydrogen Technologies: Production, Purification, Storage, Applications and Safety, 2013: p. 19-41.

[21] Rosa, V., M. Santos, and E. Da Silva, *New materials for water electrolysis diaphragms.* International journal of hydrogen energy, 1995. **20**(9): p. 697-700.

[22] Ustolin, F., et al., *Energy and Safety of Hydrogen Storage*, in *Hydrogen, Biomass and Bioenergy: Integration Pathways for Renewable Energy Applications*. 2020, Academic Press.

[23] Godula-Jopek, A., *Hydrogen production: by electrolysis*. 2015: John Wiley & Sons.

[24] Hagesteijn, K.F., S. Jiang, and B.P. Ladewig, *A review of the synthesis and characterization of anion exchange membranes.* Journal of Materials Science, 2018. **53**(16): p. 11131-11150.

[25] Zheng, Y., et al., *Water uptake study of anion exchange membranes.* Macromolecules, 2018. **51**(9): p. 3264-3278.

[26] Seh, Z.W., et al., *Combining theory and experiment in electrocatalysis: Insights into materials design.* Science, 2017. **355**(6321): p. eaad4998.

[27] O'brien, J., et al., *Hydrogen production performance of a 10-cell planar solid-oxide electrolysis stack.* 2006.

[28] Jensen, S.H., P.H. Larsen, and M. Mogensen, *Hydrogen and synthetic fuel production from renewable energy sources.* International Journal of Hydrogen Energy, 2007. **32**(15): p. 3253-3257.

[29] Ji, H.-I., et al., *Protonic ceramic electrolysis cells for fuel production: a brief review.* Journal of the Korean Ceramic Society, 2020.

[30] Matsui, T., et al., *Performance deterioration of Ni–YSZ anode induced by electrochemically generated steam in solid oxide fuel cells.* Journal of The Electrochemical Society, 2010. **157**(5): p. B776-B781.

[31] Knibbe, R., et al., *Solid oxide electrolysis cells: degradation at high current densities.* Journal of the electrochemical society, 2010. **157**(8): p. B1209-B1217.

[32] Ni, M., M.K. Leung, and D.Y. Leung, *Technological development of hydrogen production by solid oxide electrolyzer cell (SOEC).* International Journal of Hydrogen Energy, 2008. **33**(9): p. 2337-2354.

[33] Iwahara, H., et al., *Proton conduction in sintered oxides and its application to steam electrolysis for hydrogen production.* Solid State Ionics, 1981. **3**: p. 359-363.

[34] Jerkiewicz, G., *Standard and reversible hydrogen electrodes: Theory, design, operation, and applications.* ACS Catalysis, 2020. **10**(15): p. 8409-8417.

[35] Zeng, M. and Y. Li, *Recent advances in heterogeneous electrocatalysts for the hydrogen evolution reaction.* Journal of Materials Chemistry A, 2015. **3**(29): p. 14942-14962.

[36] Islam, M.H., O.S. Burheim, and B.G. Pollet, *Sonochemical and sonoelectrochemical production of hydrogen.* Ultrasonics sonochemistry, 2018.

[37] Wang, M., et al., *The intensification technologies to water electrolysis for hydrogen production–A review.* Renewable and Sustainable Energy Reviews, 2014. **29**: p. 573-588.

[38] Shinagawa, T., A.T. Garcia-Esparza, and K. Takanabe, *Insight on Tafel slopes from a microkinetic analysis of aqueous electrocatalysis for energy conversion.* Scientific reports, 2015. **5**: p. 13801.

[39] Atkins, P.W., J. De Paula, and J. Keeler, *Atkins' physical chemistry*. 2018: Oxford university press.

[40] Burheim, O.S., *Engineering energy storage*. 2017: Academic press.

[41] Dubouis, N. and A. Grimaud, *The hydrogen evolution reaction: from material to interfacial descriptors.* Chemical Science, 2019. **10**(40): p. 9165-9181.

[42] Hu, C., L. Zhang, and J. Gong, *Recent progress made in the mechanism comprehension and design of electrocatalysts for alkaline water splitting.* Energy & Environmental Science, 2019. **12**(9): p. 2620-2645.

[43] Medford, A.J., et al., *From the Sabatier principle to a predictive theory of transition-metal heterogeneous catalysis.* Journal of Catalysis, 2015. **328**: p. 36-42.

[44] Gutić, S.J., et al., *Hydrogen Evolution Reaction-From Single Crystal to Single Atom Catalysts.* Catalysts, 2020. **10**(3): p. 290.

[45] Trasatti, S., *Work function, electronegativity, and electrochemical behaviour of metals: III. Electrolytic hydrogen evolution in acid solutions.* Journal of Electroanalytical Chemistry and Interfacial Electrochemistry, 1972. **39**(1): p. 163-184.

[46] Quaino, P., et al., *Volcano plots in hydrogen electrocatalysis–uses and abuses.* Beilstein journal of nanotechnology, 2014. **5**(1): p. 846-854.

[47] Conway, B. and L. Bai, *Determination of adsorption of OPD H species in the cathodic hydrogen evolution reaction at Pt in relation to electrocatalysis.* Journal of electroanalytical chemistry and interfacial electrochemistry, 1986. **198**(1): p. 149-175.

[48] Liang, Z., H.S. Ahn, and A.J. Bard, *A study of the mechanism of the hydrogen evolution reaction on nickel by surface interrogation scanning electrochemical microscopy.* Journal of the American Chemical Society, 2017. **139**(13): p. 4854-4858.

[49] Zeng, K. and D. Zhang, *Evaluating the effect of surface modifications on Ni based electrodes for alkaline water electrolysis.* Fuel, 2014. **116**: p. 692-698.

[50] Faid, A.Y., et al., *Optimized Nickel-Cobalt and Nickel-Iron Oxide Catalysts for the Hydrogen Evolution Reaction in Alkaline Water Electrolysis.* Journal of The Electrochemical Society, 2019. **166**(8): p. F519-F533.

[51] Faid, A.Y., et al., *Highly active nickel-based catalyst for hydrogen evolution in anion exchange membrane electrolysis.* Catalysts, 2018. **8**(12): p. 614.

[52] Vij, V., et al., *Nickel-based electrocatalysts for energy-related applications: oxygen reduction, oxygen evolution, and hydrogen evolution reactions.* Acs Catalysis, 2017. **7**(10): p. 7196-7225.

[53] Zhu, Y., et al., *Nickel-based electrodes as catalysts for hydrogen evolution reaction in alkaline media.* Ionics, 2018. **24**(4): p. 1121-1127.

[54] Alsabet, M., M. Grdeń, and G. Jerkiewicz, *Electrochemical growth of surface oxides on nickel. Part 3: Formation of β-NiOOH in relation to the polarization potential, polarization time, and temperature.* Electrocatalysis, 2015. **6**(1): p. 60-71.

[55] Alsabet, M., M. Grden, and G. Jerkiewicz, *Electrochemical growth of surface oxides on nickel. Part 2: formation of β-Ni (OH) 2 and NiO in relation to the polarization potential, polarization time, and temperature.* Electrocatalysis, 2014. **5**(2): p. 136-147.

[56] Alsabet, M., M. Grden, and G. Jerkiewicz, *Electrochemical growth of surface oxides on nickel. Part 1: formation of α-Ni (OH) 2 in relation to the polarization potential, polarization time, and temperature.* Electrocatalysis, 2011. **2**(4): p. 317-330.

[57] Bode, H., K. Dehmelt, and J. Witte, *Zur kenntnis der nickelhydroxidelektrode—I. Über das nickel (II)-hydroxidhydrat.* Electrochimica Acta, 1966. **11**(8): p. 1079-IN1.

[58] Krstajić, N., et al., *On the kinetics of the hydrogen evolution reaction on nickel in alkaline solution: Part I. The mechanism.* Journal of Electroanalytical Chemistry, 2001. **512**(1-2): p. 16-26.

[59] Oshchepkov, A., *Investigation of the hydrogen electrode reactions on Ni electrocatalysts in alkaline medium*. 2017.

[60] Oshchepkov, A.G., et al., *Exploring the influence of the nickel oxide species on the kinetics of hydrogen electrode reactions in alkaline media.* Topics in Catalysis, 2016. **59**(15-16): p. 1319-1331.

[61] Mohsenzadeh, A., T. Richards, and K. Bolton, *DFT study of the water gas shift reaction on Ni (111), Ni (100) and Ni (110) surfaces.* Surface Science, 2016. **644**: p. 53-63.

[62] Che, F., et al., *Catalytic water dehydrogenation and formation on nickel: Dual path mechanism in high electric fields.* Journal of Catalysis, 2015. **332**: p. 187-200.

[63] Oshchepkov, A., et al., *Hydrogen Electrode Reactions over Nickel-Based Catalysts in Alkaline Medium: Influence of Composition and Structure of Ni Particles*. 2015, 12th European Congress on Catalysis – EuropaCat-XII, Kazan, Russia.

[64] Grdeń, M. and G. Jerkiewicz, *Influence of surface treatment on the kinetics of the hydrogen evolution reaction on bulk and porous nickel materials.* Electrocatalysis, 2019. **10**(2): p. 173-183.

[65] Shen, J., D. Lan, and T. Yang, *Influence of supporting electrolyte on the electrocatalysis of CO2 reduction by cobalt protoporphyrin.* Int. J. Electrochem. Sci, 2018. **13**: p. 9847-9857.

[66] Merrill, M.D. and B.E. Logan, *Electrolyte effects on hydrogen evolution and solution resistance in microbial electrolysis cells.* Journal of Power Sources, 2009. **191**(2): p. 203-208.

[67] Le, J.M., et al., *Tuning Mechanism through Buffer Dependence of Hydrogen Evolution Catalyzed by a Cobalt Mini-enzyme.* Biochemistry, 2020.

[68] Bentley, C.L., et al., *Electrochemical Proton Reduction and Equilibrium Acidity (p K a) in Aprotic Ionic Liquids: Protonated Amines and Sulfonamide Acids.* The Journal of Physical Chemistry C, 2015. **119**(38): p. 21828-21839.

[69] Bentley, C.L., et al., *Electrochemical Proton Reduction and Equilibrium Acidity (p K a) in Aprotic Ionic Liquids: Phenols, Carboxylic Acids, and Sulfonic Acids.* The Journal of Physical Chemistry C, 2015. **119**(38): p. 21840-21851.

[70] Kahyarian, A., A. Schumacher, and S. Nesic, *Mechanistic investigation of hydrogen evolution reaction from multiple proton donors: The case of mildly acidic solutions containing weak acids.* Journal of The Electrochemical Society, 2019. **166**(8): p. H320-H330.

[71] Lamoureux, P.S., A.R. Singh, and K. Chan, *pH effects on hydrogen evolution and oxidation over Pt (111): Insights from first-principles.* Acs Catalysis, 2019. **9**(7): p. 6194-6201.

[72] Sheng, W., et al., *Correlating hydrogen oxidation and evolution activity on platinum at different pH with measured hydrogen binding energy.* Nature communications, 2015. **6**(1): p. 1-6.

[73] Markovic, N., H. Gasteiger, and P.N. Ross, *Kinetics of oxygen reduction on Pt (hkl) electrodes: implications for the crystallite size effect with supported Pt electrocatalysts.* Journal of the Electrochemical Society, 1997. **144**(5): p. 1591-1597.

[74] Zheng, J., et al., *Universal dependence of hydrogen oxidation and evolution reaction activity of platinum-group metals on pH and hydrogen binding energy.* Science advances, 2016. **2**(3): p. e1501602.

[75] Van Der Niet, M.J., et al., *Water dissociation on well-defined platinum surfaces: The electrochemical perspective.* Catalysis today, 2013. **202**: p. 105-113.

[76] Ledezma-Yanez, I., et al., *Interfacial water reorganization as a pH-dependent descriptor of the hydrogen evolution rate on platinum electrodes.* Nature Energy, 2017. **2**(4): p. 17031.

[77] Frumkin, A., *Hydrogen overvoltage and the structure of the double layer.* Z. Physik. Chem. A, 1933. **164**: p. 121-133.

[78] Liu, E., et al., *Unifying the hydrogen evolution and oxidation reactions kinetics in base by identifying the catalytic roles of hydroxyl-water-cation adducts.* Journal of the American Chemical Society, 2019. **141**(7): p. 3232-3239.

[79] Subbaraman, R., et al., *Trends in activity for the water electrolyser reactions on 3 d M (Ni, Co, Fe, Mn) hydr (oxy) oxide catalysts.* Nature materials, 2012. **11**(6): p. 550-557.

[80] Zeng, Z., et al., *Stabilization of ultrathin (hydroxy) oxide films on transition metal substrates for electrochemical energy conversion.* Nature Energy, 2017. **2**(6): p. 1-9.

[81] Floner, D., C. Lamy, and J.-M. Leger, *Electrocatalytic oxidation of hydrogen on polycrystal and single-crystal nickel electrodes.* Surface science, 1990. **234**(1-2): p. 87-97.

[82] Kuznetsov, A.N., et al., *Influence of the NaOH Concentration on the Hydrogen Electrode Reaction Kinetics of Ni and NiCu Electrodes.* ChemElectroChem, 2020. **7**(6): p. 1438-1447.

[83] Salmazo, D., et al., *On the feasibility of bifunctional hydrogen oxidation on Ni and NiCu surfaces.* Electrochimica Acta, 2019. **305**: p. 452-458.

[84] Koster, D., et al., *Extracting the kinetic parameters of the hydrogen evolution reaction at Pt in acidic media by means of dynamic multi-frequency analysis.* Electrochimica Acta, 2019. **308**: p. 328-336.

[85] Oshchepkov, A.G., et al., *On the effect of temperature and surface oxidation on the kinetics of hydrogen electrode reactions on nickel in alkaline media.* Electrochimica Acta, 2018. **269**: p. 111-118.

[86] Bockris, J.O.M. and E. Potter, *The mechanism of hydrogen evolution at nickel cathodes in aqueous solutions.* The Journal of Chemical Physics, 1952. **20**(4): p. 614-628.

[87] Miles, M., et al., *Effect of temperature on electrode kinetic parameters for hydrogen and oxygen evolution reactions on nickel electrodes in alkaline solutions.* Journal of the Electrochemical Society, 1976. **123**(3): p. 332.

[88] Krstajić, N., et al., *On the kinetics of the hydrogen evolution reaction on nickel in alkaline solution: Part II. Effect of temperature.* Journal of Electroanalytical Chemistry, 2001. **512**(1-2): p. 27-35.

[89] González-Buch, C., et al., *Study of the catalytic activity of 3D macroporous Ni and NiMo cathodes for hydrogen production by alkaline water electrolysis.* Journal of Applied Electrochemistry, 2016. **46**(7): p. 791-803.

[90] Hall, D.S., C. Bock, and B.R. MacDougall, *The electrochemistry of metallic nickel: oxides, hydroxides, hydrides and alkaline hydrogen evolution.* Journal of The Electrochemical Society, 2013. **160**(3): p. F235.

[91] Makrides, A.C., *Hydrogen overpotential on nickel in alkaline solution.* Journal of The Electrochemical Society, 1962. **109**(10): p. 977.

[92] Radovic-Hrapovic, Z. and G. Jerkiewicz, *The temperature dependence of the cyclic-voltammetry response for the Pt (110) electrode in aqueous H2SO4 solution.* Journal of Electroanalytical Chemistry, 2001. **499**(1): p. 61-66.

[93] Zolfaghari, A. and G. Jerkiewicz, *Temperature-dependent research on Pt (111) and Pt (100) electrodes in aqueous H2SO4.* Journal of Electroanalytical Chemistry, 1999. **467**(1-2): p. 177-185.

[94] Huang, Z.F., et al., *Design of efficient bifunctional oxygen reduction/evolution electrocatalyst: recent advances and perspectives.* Advanced Energy Materials, 2017. **7**(23): p. 1700544.

[95] Reier, T., et al., *Electrocatalytic oxygen evolution reaction in acidic environments–reaction mechanisms and catalysts.* Advanced Energy Materials, 2017. **7**(1): p. 1601275.

[96] Bockris, J.O.M., *Kinetics of activation controlled consecutive electrochemical reactions: anodic evolution of oxygen.* The Journal of Chemical Physics, 1956. **24**(4): p. 817-827.

[97] Suen, N.-T., et al., *Electrocatalysis for the oxygen evolution reaction: recent development and future perspectives.* Chemical Society Reviews, 2017. **46**(2): p. 337-365.

[98] Marini, S., et al., *Advanced alkaline water electrolysis.* Electrochimica Acta, 2012. **82**: p. 384-391.

[99] Willsau, J., O. Wolter, and J. Heitbaum, *Does the oxide layer take part in the oxygen evolution reaction on platinum?: A DEMS study.* Journal of electroanalytical chemistry and interfacial electrochemistry, 1985. **195**(2): p. 299-306.

[100] Damjanovic, A., V. Birss, and D. Boudreaux, *Electron Transfer Through Thin Anodic Oxide Films during the Oxygen Evolution Reactions at Pt Electrodes I. Acid Solutions.* Journal of The Electrochemical Society, 1991. **138**(9): p. 2549-2555.

[101] Reier, T., M. Oezaslan, and P. Strasser, *Electrocatalytic oxygen evolution reaction (OER) on Ru, Ir, and Pt catalysts: a comparative study of nanoparticles and bulk materials.* Acs Catalysis, 2012. **2**(8): p. 1765-1772.

[102] Damjanovic, A., *Electron transfer through thin anodic films in oxygen evolution at Pt electrodes in alkaline solutions.* Electrochimica acta, 1992. **37**(13): p. 2533-2539.

[103] Vetter, K. and J. Schultze, *The kinetics of the electrochemical formation and reduction of monomolecular oxide layers on platinum in 0.5 M H2SO4: Part I. Potentiostatic pulse measurements.* Journal of Electroanalytical Chemistry and Interfacial Electrochemistry, 1972. **34**(1): p. 131-139.

[104] Jahangiri, S. and N.J. Mosey, *Computational Investigation of the Oxygen Evolution Reaction Catalyzed by Nickel (Oxy) hydroxide Complexes.* The Journal of Physical Chemistry C, 2018. **122**(45): p. 25785-25795.

[105] Conway, B. and P. Bourgault, *Electrochemistry of the nickel oxide electrode: part III. Anodic polarization and self-discharge behavior.* Canadian Journal of Chemistry, 1962. **40**(8): p. 1690-1707.

[106] Van Drunen, J., et al., *Electrochemically active nickel foams as support materials for nanoscopic platinum electrocatalysts.* ACS applied materials & interfaces, 2014. **6**(15): p. 12046-12061.

[107] Klaus, S., et al., *Effects of Fe electrolyte impurities on Ni (OH) 2/NiOOH structure and oxygen evolution activity.* The Journal of Physical Chemistry C, 2015. **119**(13): p. 7243-7254.

[108] Stern, L.-A. and X. Hu, *Enhanced oxygen evolution activity by NiOx and Ni (OH) 2 nanoparticles.* Faraday discussions, 2015. **176**: p. 363-379.

[109] Corrigan, D.A. and R.M. Bendert, *Effect of coprecipitated metal ions on the electrochemistry of nickel hydroxide thin films: cyclic voltammetry in 1M KOH.* Journal of The Electrochemical Society, 1989. **136**(3): p. 723-728.

[110] Trotochaud, L., et al., *Nickel–iron oxyhydroxide oxygen-evolution electrocatalysts: the role of intentional and incidental iron incorporation.* Journal of the American Chemical Society, 2014. **136**(18): p. 6744-6753.

[111] Lyons, M.E. and M.P. Brandon, *The oxygen evolution reaction on passive oxide covered transition metal electrodes in aqueous alkaline solution. Part 1-Nickel.* Int. J. Electrochem. Sci, 2008. **3**(12): p. 1386-1424.

[112] Cossar, E., et al., *Highly Active Nickel–Iron Nanoparticles With and Without Ceria for the Oxygen Evolution Reaction.* Electrocatalysis, 2021. **12**(5): p. 605-618.

[113] Cossar, E., et al., *The performance of nickel and nickel-iron catalysts evaluated as anodes in anion exchange membrane water electrolysis.* Catalysts, 2019. **9**(10): p. 814.

[114] Dai, L., et al., *Ultrathin Ni (0)-Embedded $Ni(OH)_2$ Heterostructured Nanosheets with Enhanced Electrochemical Overall Water Splitting.* Advanced Materials, 2020. **32**(8): p. 1906915.

[115] Luan, C., et al., *Structure effects of 2D materials on α-Nickel hydroxide for oxygen evolution reaction.* ACS nano, 2018. **12**(4): p. 3875-3885.

[116] Yu, J., et al., *Facile synthesis of monodispersed α-$Ni(OH)_2$ microspheres assembled by ultrathin nanosheets and its performance for oxygen evolution reduction.* Frontiers in Materials, 2019. **6**: p. 124.

[117] Wu, J., et al., *Facile assembly of $Ni(OH)_2$ nanosheets on nitrogen-doped carbon nanotubes network as high-performance electrocatalyst for oxygen evolution reaction.* Journal of Alloys and Compounds, 2018. **731**: p. 766-773.

[118] Liu, G., et al., *Vapor-phase hydrothermal transformation of a nanosheet array structure Ni (OH) 2 into ultrathin Ni 3 S 2 nanosheets on nickel foam for high-efficiency overall water splitting.* Journal of Materials Chemistry A, 2018. **6**(39): p. 19201-19209.

[119] Gao, M., et al., *Efficient water oxidation using nanostructured α-nickel-hydroxide as an electrocatalyst.* Journal of the American Chemical Society, 2014. **136**(19): p. 7077-7084.

[120] Stern, L.-A., et al., *Ni 2 P as a Janus catalyst for water splitting: the oxygen evolution activity of Ni 2 P nanoparticles.* Energy & Environmental Science, 2015. **8**(8): p. 2347-2351.

3 Basics of Sonochemistry

3.1 Fundamentals of Sonochemistry

Sonochemistry is the use of power ultrasound to enhance and modify chemical reactions. Power ultrasound is a well-defined sound wave in the range 20 kHz – 2 MHz (10 – 1,000 W/cm^2) and it is regarded as the effect of the sound wave on the medium [1]. The most important phenomena that arises from the propagation of an ultrasonic wave into a liquid is acoustic cavitation [2]. When an ultrasonic wave propagates through a liquid media such as water, many tiny gas bubbles are formed. The phenomenon of formation of bubbles and their subsequent violent collapse of the bubbles is known as *acoustic cavitation* [2]. The collapsing bubble can generate high temperatures up to 5,000 °C and high pressures up to 2,000 atm [3]. The cavitation bubble contains gas molecules such as N_2 and O_2 and vapour from the solvent. In the high temperature and pressure generated by bubble collapse, the solvent vapour and gas molecules generate various highly reactive radicals and other species such as $H^{\bullet}$ and $OH^{\bullet}$ radicals, O_3, H_2O_2 and O atoms through endothermic chemical reactions [2]. The hydroxyl radical ($OH^{\bullet}$) is the most dominant species in sonochemical reactions. The production of O_3 is negligible comparing to $OH^{\bullet}$ radicals and O atoms reacts with H_2O to produce H_2O_2. These species diffuse out from the interior of the bubble into the surroundings and react with solutes present in the aqueous solution [2]. A few possible reactions are shown in equations (3.1)-(3.4). The evolution of a cavitation bubble during ultrasonication is shown in Figure 3.1.

$$H_2O \rightarrow H^{\bullet} + OH^{\bullet} \quad (3.1)$$

$$H^{\bullet} + OH^{\bullet} \rightarrow H_2 + O \quad (3.2)$$

$$OH^{\bullet} + OH^{\bullet} \rightarrow H_2O_2 \quad (3.3)$$

$$H^{\bullet} + H^{\bullet} \rightarrow H_2 \quad (3.4)$$

Overall, it has been shown that ultrasound affects both heterogeneous systems (thermodynamic systems consisting of two or more phases) consisting of the electrode and the electrolyte and, homogeneous systems (systems whose chemical composition and physical properties are the same in all parts of the systems) that take place in the bulk electrolyte, which may experience extreme conditions by acoustic cavitation. The sonochemical effect caused by acoustic cavitation may lead to new reaction mechanisms [4].

There are several factors that affect the sonochemical reactions. Among them, the ultrasonic frequency (*f*) is the dominant factor that should be considered to obtain maximum efficiency in sonochemical reactions. The mechanical forces applied by ultrasonication are directly dependent upon the ultrasonic frequency. The lower frequency provides the largest

mechanical effect [1]. Another major factor that dominates the sonochemical reactions is the acoustic power (P_{acous}). The ultrasonic or acoustic power could be determined calorimetrically using the methods of Margulis *et al.* [5] and Contamine *et al*. [6] (equation 3.5):

$$P_{acous} = mC_{p,s}(\frac{dT}{dt}) \qquad (3.5)$$

where, m is the mass of the solution (g), $C_{p,s}$ is the specific constant pressure heat capacity of water (J g^{-1} K^{-1}) and $\frac{dT}{dt}$ is the temperature increase after ultrasonication time t. In addition, the number of active bubbles and the bubble size is also expected to increase with increasing acoustic power at a given frequency [1].

The bulk solution temperature influences the sonochemical reactions in various ways. The vapour pressure, as well as the internal pressure within the collapsing bubbles, increases with increasing bulk solution temperature. This leads to a decrease in the maximum collapse temperature yielding a decrease in the formation of primary radicals. In addition, the reaction kinetics may increase with increasing bulk solution temperature. Moreover, the gas concentration, surface tension and other physical properties of the liquid can be affected by bulk liquid temperature increases which can influence the cavitation phenomena [7].

It has been reported that a higher cavitation bubble temperature is obtained in low vapour pressure liquids [8]. This can be explained by equation (3.6) [9]:

$$T_{max} = T_0 \left[\frac{P_m(\gamma-1)}{P_v}\right] \qquad (3.6)$$

where T_0 is the ambient solution temperature, P_m is the pressure in the liquid (a sum the hydrostatic and acoustic pressures) ($\gamma = \frac{c_p}{c_v}$) is the polytropic index of gases, the C_p and C_v are the specific heats of an ideal gas at constant pressure and at constant volume, respectively and P_v is the pressure in the bubble at its maximum size, allows to calculate the maximum theoretical temperature within the bubble (T_{max}). A higher vapor pressure means weaker bubble collapse leading to a lower bubble temperature [10].

In addition, increasing temperature decreases the polytropic index of gases. When the liquid temperature increases, it causes less violent collapse of the cavitation bubble due to the decrease of the polytropic index. Less violent collapse leads to lower internal bubble temperatures. Lower internal bubble temperature lowers the formation of free radicals by the

decomposition of water i.e., sonolysis [1, 10]. It is also known that increasing temperature quenches the cavitation process and therefore, increasing temperature decreases the global cavitational activity of the system leading to the decrease in the sonochemical effect [10].

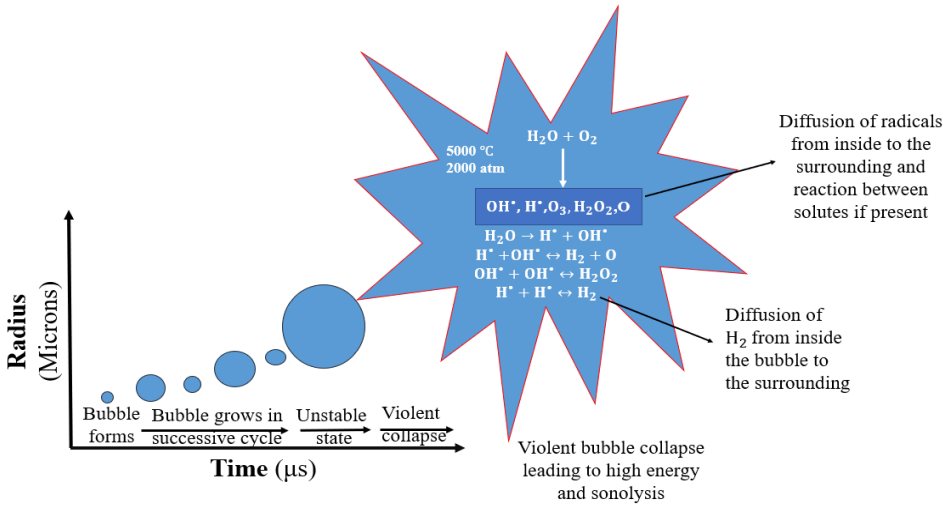

Figure 3.1. The evolution of a cavitation bubble during ultrasonication and the production of sonolysis species by acoustic cavitation.

The sonochemical efficiency (SE) of an ultrasonic reactor is commonly evaluated by measuring the yield of $OH^{\bullet}$. Several dosimetry methods have been developed for the quantification of $OH^{\bullet}$ generated by acoustic cavitation. *Weissler* reaction [11], TPPS (porphine tetra(p-phenylsulfonate) [12], *Fricke* [13], salicylic acid [14], terephthalate acid [15], titanyl sulfate dosimetry [16] and electron spin trapping [15] have been reported as possible options for radicals determination methods in the literature. The most commonly used methods are *Weissler* (potassium iodide, KI), *Fricke* and terephthalate acid (TA) [17].

When the generation of radicals are high, the *Fricke method* (Fe^{2+}/Fe^{3+}) is proved to be appropriate; however, in general, the yields are low [18]. The more direct evidence of OH radicals formation has been carried out by the terephthalate dosimetry method [18].

Terephthalic acid ($C_6H_4(CO_2H)_2$) generates terephthalate anions in an aqueous alkaline solution. When $OH^{\bullet}$ radicals react with terephthalate ions, they produce highly fluorescent 2-hydroxyterephthalate ions [19]. The fluorescence intensity can be used to quantify the number of hydroxyl radicals ($OH^{\bullet}$) [18].

Potassium iodide (KI) dosimetry is a simpler method for the quantitation of oxidants produced through acoustic cavitation. This method is also known as the *Weissler method* [20]. In this method, $OH^{\bullet}$ radicals oxidize KI giving rise to an iodine (I) atom (equation 3.7). This initiates a series of reactions presented from equations (3.7)-(3.10) [20]:

$$OH^{\bullet} + I^{-} \rightarrow OH^{-} + I \quad (3.7)$$

$$I + I^{-} \rightarrow I_2^{-} \quad (3.8)$$

$$2I_2^{-} \rightarrow I_2 + 2I^{-} \quad (3.9)$$

$$I_2 + I^{-} \rightarrow I_3^{-} \quad (3.10)$$

The absorbance of I_3^{-} can be measured using a UV-Vis spectrometer. It has been reported that the sonochemical yield measured by the TA dosimetry method is significantly lower compared to that measured by the Weissler and Fricke dosimetries [17].

3.2 Introduction to Sonoelectrochemistry

Sonoelectrochemistry is the use of power ultrasound in electrochemistry [4]. Figure 3.2 shows a schematic diagram of a sonoelectrochemical reactor set-up. Ultrasound is transmitted using either an ultrasonic bath, a probe (horn) or a transducer. The ultrasonic probe can be either directly immersed in the electrolyte or separated from it. When an ultrasonic probe is separated from the electrolyte, an inner electrochemical cell is used, as shown in Figure 3.2. In both cases, an ultrasonic horn should face the working electrode surface, known as “face-on” geometry.

It is well-known that the use of power ultrasound in electrochemistry offers many advantages including [4]:

1. Gas bubble removal at the electrode surface;
2. Solution degassing;
3. Disruption of the *Nernst* diffusion layer (δ);
4. Enhancement of mass transport of electroactive species through the double layer; and,
5. Activation and cleaning of the electrode surface.

Table 3.1 summarises the major influencing factors of power ultrasound in electrochemistry.

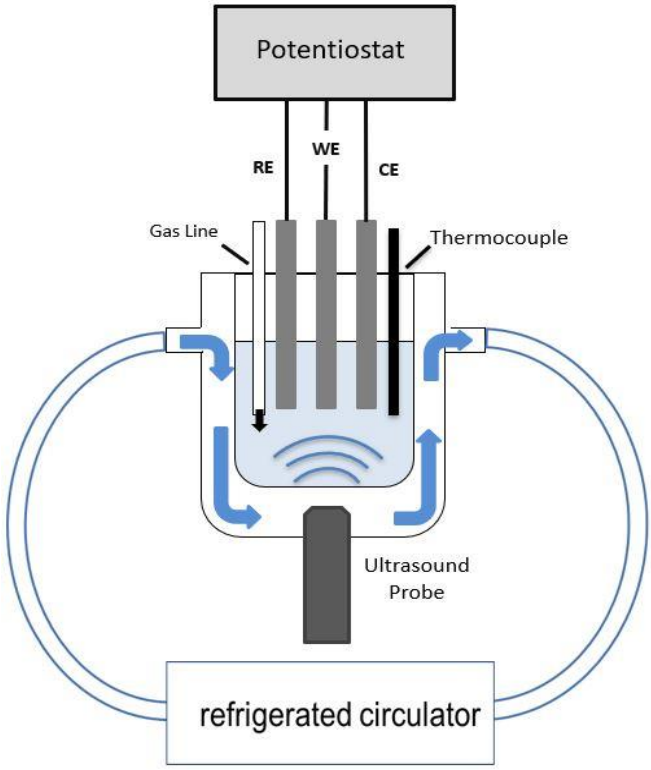

Figure 3.2. Schematic diagram of a sonoelectrochemical reactor experimental set-up. CE, counter electrode; WE, working electrode; and RE, reference electrode.

Table 3.1. Summarizes of major influencing factors of ultrasound on electrochemistry

Influencing factors of ultrasound on electrochemistry						Ref
	Acoustic streaming	**Turbulent flow**	**Microjets and Microstreaming**	**Shock waves**	**Chemical effects**	[4, 7, 21-23]
Cause	• The power of acoustic streaming is directly proportional to the intensity of ultrasound, the surface area of the ultrasonic emitting device and the attenuation coefficient of the medium. • It is inversely proportional to the bulk solution viscosity and the speed of sound.	• The movement of the acoustic cavitation bubble	• The collapsing of acoustic bubbles on a solid surface leads to the formation of microjets being directed towards the surface of the solid material at speeds of up to 200 m/s.	• Produced at the end of the strong collapse of bubbles	• "Sonolytic" effects in electrochemistry due to acoustic cavitation in aqueous media	
Effect	• The enhancement of the movement of the solution • Reducing the diffusion boundary layer • Promoting the mass transfer of electroactive species to the electrode surface	• Increases the mass transport process within the solution and the electrode surface similar to acoustic streaming	• If the surface is an electrode, the combined effects of the microjet and microstreaming enhance mass transport to the electrode surface • Electrode and surface cleaning that prevents fouling of the electrode surface (and accumulation of gas bubbles at the electrode surface) • Enhance the electrodeposition process	• Erosion of the electrode surface leading to an increase in the current	• Formation of highly reactive radicals such as OH•, H_2O_2•, and O•	

Despite its promising applications, sonoelectrochemistry has not been used widely. There are some difficulties in carrying out experiments using both ultrasound and electrochemical processes including positioning of the electrode, cell geometry, and ultrasonic horn tip/electrode distance. Furthermore, the impacts of ultrasound parameters such as frequency and acoustic power should be considered. However, recently, this field is regaining attention because of the advances made in ultrasonic equipment [24]. For example, the use of ultrasound in water electrolysis technology for hydrogen (and oxygen) production, has shown to improve the energy efficiency of the water electrolysis process [25, 26] (see next section).

Recently, the use of ultrasound for the synthesis of materials especially nanostructured materials for fuel cells, electrolysers, supercapacitors, and semiconductors catalysts has provided many advantages in terms of simplicity, efficiency, rapidity, and environmentally-friendliness [27-31]. Also, several studies have illustrated that the shape and size of particles can be easily controlled by ultrasonication time, power, and frequency [27, 28, 32, 33].

3.3 Sonoelectrochemical Production of Hydrogen

Developing cost-effective energy storage technologies to use low-cost electricity from renewable energy technologies is essential to meet the decarbonisation of our energy systems [34]. Large-scale energy storage plays an important role in resolving problems related to peak energy consumption and production typically being out of phase (known as the *duck curve*) [35, 36]. Energy storage is a feasible solution for smoothing out the *duck curve* that allows energy to be generated when it is available and sent out when and where it is needed [35].

Hydrogen energy systems are considered to be essential for long-term energy storage and conversion technology to solve global environmental problems [37]. Renewable energy can be used in relation to hydrogen in several ways [24]:

1. Converting excess electricity into hydrogen (energy carrier) and converting it back into electricity when and where required. This entails hydrogen storage for renewable electricity;
2. Mixing electrolytic hydrogen with natural gas or converting it to methane, as this allows for the hydrogen to be stored in the existing gas grid;
3. Converting excess electricity to hydrogen, which can be used for industrial processes; and,

4. Using excess electricity for hydrogen production and then using the hydrogen produced as a clean fuel for use in the transport sector.

Water electrolysis is one of the most important technologies in such a system. The cell voltage for water splitting is considerably higher than the thermodynamic decomposition voltage due to high overpotentials, especially for the OER. In addition to the anode and cathode overpotentials, the ohmic cell voltage drop from the presence of the gas bubbles in the solution and at the electrode surface contributes to high energy consumption [38, 39]. The total ohmic resistance of water electrolysis is shown in equation (3.11) [39].

$$\sum R = R_e + R_m + R_b + R_c \qquad (3.11)$$

where R_e is the electrolyte resistance, R_m is the membrane resistance, R_b is the bubble resistance and R_c is the circuit resistance. The R_m and R_c are constant in an electrolytic cell and can be reduced by optimizing the wire connection and production process of the membrane. The dispersion of the bubbles in the electrolyte decreases the electrolyte conductivity and in turns increases R_e. Besides, the bubble coverage on the surface of the electrode act as a shield for the electric field, leading to high bubble resistance R_b (also termed in the industry as bubble "overpotential") [39, 40].

The cathodic and anodic overpotentials can be reduced by applying an efficient electrocatalyst on to the electrodes and/or operating the cell at higher temperatures (65–80℃) [38]. The efficiency of water electrolysis can be increased by controlling the following factors: (a) more effective disengagement of gas bubbles from the electrodes and the membranes, thereby virtually eliminating gas blanketing; (b) making gas bubble removal more effective from the electrolyte, even with very small electrode spacing; and, (c) promoting faster removal of the gas bubbles at the electrode surface to increase the local heat/mass transfer coefficients [37].

Experimental observations have shown that the electrochemical production of hydrogen can be improved significantly by using power ultrasound through [1]:

- Enhancing mass transport in the bulk electrolyte and near the surfaces;
- Cleaning and activation of surfaces; and,
- Changing reaction pathways caused by sonochemical effects.

Figure 3.3 shows a simplified water electrolyser (containing a protonic conducting membrane) subjected to an ultrasonic field. Figure 3.3b illustrates the accumulation of hydrogen bubbles on the cathode and oxygen bubbles on the anode, leading to high ohmic resistance and cathodic and anodic overpotentials. Removal of hydrogen and oxygen bubbles from the electrode surfaces by applying ultrasound is shown in Figure 3.3c.

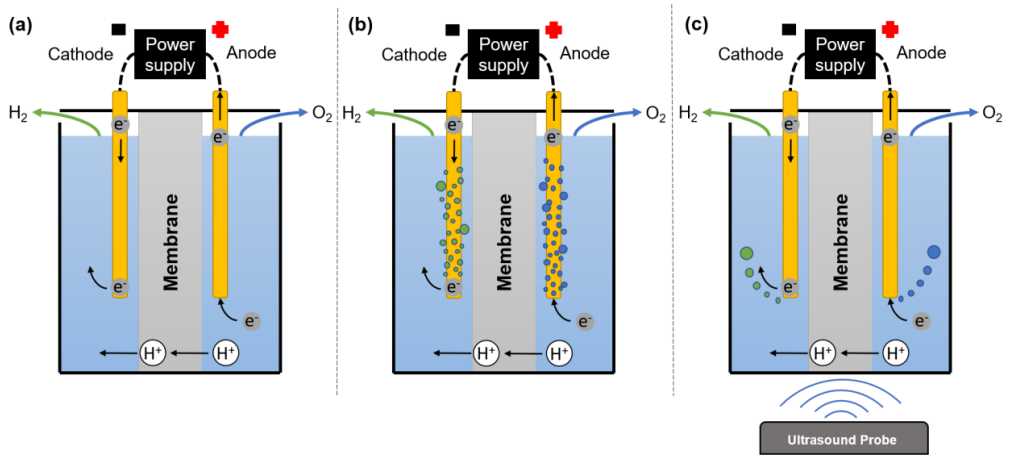

Figure 3.3. A simplified water electrolyser (containing a protonic conducting membrane) showing the HER at the cathode and the OER at the anode, subjected to ultrasound. (a) DC applied, (b) DC applied and oxygen and hydrogen bubbles produced at the anode and cathode respectively, (c) DC and ultrasonic applied leading to effective removal of gas bubbles from the electrode surfaces.

Up to now, there are some research studies on the sonochemical production of hydrogen [41-44] and promising results have been obtained through these studies for an efficient and clean production of hydrogen. For instance, Merouani et al. [44], Kerboua et al. [45] and Rashwan et al. [46] have lately presented interesting reviews on the sonochemical production of hydrogen and the different parameters affecting this mechanism. However, sonoelectrochemical production of Hydrogen and use of ultrasound in water electrolysis just limited to a few studies. Furthermore, a stated earlier works studying the effects of (power) ultrasound on water electrolysis are scarce. Water electrolysis in presence of ultrasound was first observed by Moriguchi in the 1930's using a platinum (Pt) electrode, which occurred at faster rates and lower cell voltages than under *silent* conditions [39, 47]. Sonoelectrochemical production of hydrogen was then continued by Pollet's research group at the Birmingham

Proton Exchange Membrane Fuel Cell in 2011 [24]. For example, Lepesant [48] and other researchers such as Zadeh [49] and Symes [50] under the supervision of Pollet, studied the influences of ultrasound on electrolytic hydrogen production from weak acidic (H_2SO_4) and alkaline (NaOH and KOH) solutions using various electrode materials including platinum (Pt), industrial carbon (C), glassy carbon (GC) and 316 stainless steel (316-SS).

Li *et al.* [37] studied the effects of power ultrasound on water electrolysis in different NaOH concentrations. They found that the energy efficiency of water electrolysis was considerably improved in the presence of an ultrasonic field. This was observed by measuring the cell voltage, the efficiency, and the energy consumption of the generated gas from the electrolytic process. A large reduction of the cell voltage was observed under the ultrasonic field, especially at high current densities and low electrolyte concentrations. At the same current density, the cell voltage difference under *silent* and ultrasonic conditions fell as the concentration of the electrolyte was increased. It was also observed that the efficiency of hydrogen production was enhanced by 5–18% at high current densities under acoustic conditions. Overall, the energy-saving for molecular hydrogen production by using an ultrasonic field was about 10–25% for specific electrolyte concentrations and when a high current density was employed. Lin *et al.* [26] investigated the ultrasonic effects on hydrogen production by water electrolysis. In their study, they carried out electrochemical impedance spectroscopy (EIS) to examine polarization impedance phenomena in ultrasonic water electrolysis (Figure 3.4). For the first time, EIS was used to analyse the electrochemical reaction during water electrolysis. They found that at a cell voltage of 2 V, ultrasound improved activity and concentration impedances and accelerated the detachment of hydrogen bubbles during water electrolysis. At room temperature, and with an electrode gap of 2 mm, a cell voltage of 4 V, and an electrolyte concentration of 40 wt%, the difference in current density between water electrolysis carried out in the absence and presence of ultrasound (225 W) was 240 mA cm^{-2}. They deducted that the power required for the sonoelectrolytic process showed a power saving of 3.5 kW and an efficiency saving of 15%.

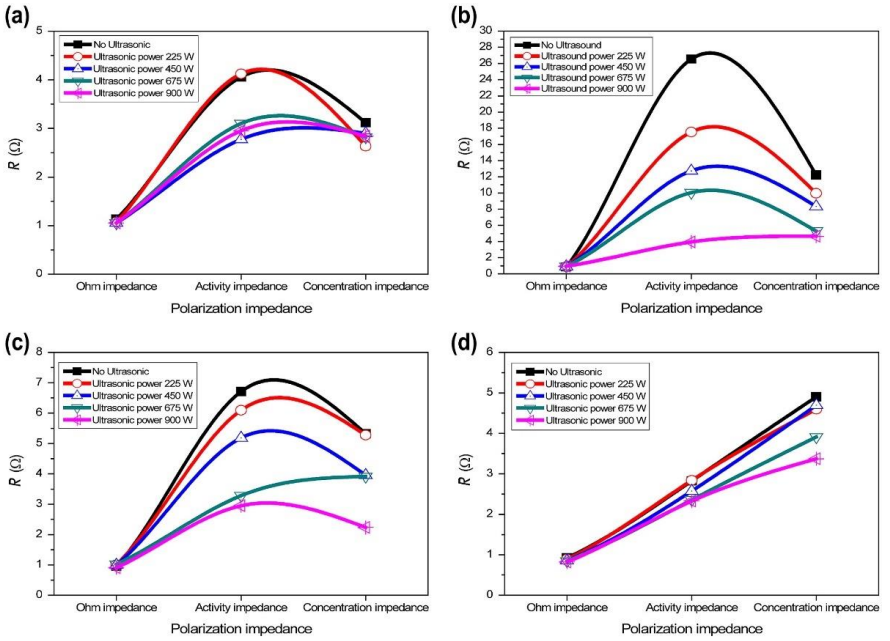

Figure 3.4. Polarization impedance of different electrolyte concentrations with a 2 V cell voltage and electrode distance of 2 mm. (a) 10 wt%; (b) 20 wt%; (c) 30 wt%; (d) 40 wt% KOH [26].

Budischak *et al.* [25] also studied the effects of ultrasound on HER in 2.0 M KOH using Pt as a working electrode. Their results illustrated that ultrasound can significantly improve the efficiency of an electrolyser, especially at intermediate current densities.

Until now, only a few fundamental investigations have been carried out in the field of sonoelectrochemical production of hydrogen. There has not been much focus on systematic investigations of the effects that various sonoelectrochemical experimental parameters have on processes, such as ultrasonic power, ultrasonic frequency, electrolyte type and concentrations, electrode materials and reactor design. Furthermore, the mechanism of the HER under ultrasonication is still ambiguous. A major problem for practical applications is the electrode erosion and material stability (e.g., the polymeric membrane for PEMWE and AEMWE) under ultrasonication, which may hinder the life of a sonoelectrochemical system. Moreover, an extended investigation on the integration of sonolysis and electrocatalysis processes for large scale hydrogen production via water splitting should be performed [24].

References

[1] Islam, M.H., O.S. Burheim, and B.G. Pollet, *Sonochemical and sonoelectrochemical production of hydrogen.* Ultrasonics sonochemistry, 2019. **51**: p. 533-555.

[2] Yasui, K., *Acoustic cavitation and bubble dynamics*. 2018: Springer.

[3] Suslick, K.S., *Sonochemistry.* science, 1990. **247**(4949): p. 1439-1445.

[4] Pollet, B., *Power Ultrasound in Electrochemistry: From Versatile Laboratory Tool to Engineering Solution*. 2012: John Wiley & Sons.

[5] Margulis, M. and I. Margulis, *Calorimetric method for measurement of acoustic power absorbed in a volume of a liquid.* Ultrasonics Sonochemistry, 2003. **10**(6): p. 343-345.

[6] Contamine, R.F., et al., *Power measurement in sonochemistry.* Ultrasonics Sonochemistry, 1995. **2**(1): p. S43-S47.

[7] Mason, T.J., *Sonochemistry*. 1990: Royal Society of Chemistry Cambridge, UK.

[8] Rae, J., et al., *Estimation of ultrasound induced cavitation bubble temperatures in aqueous solutions.* Ultrasonics sonochemistry, 2005. **12**(5): p. 325-329.

[9] Cherepanov, P.V., M. Ashokkumar, and D.V. Andreeva, *Ultrasound assisted formation of Al–Ni electrocatalyst for hydrogen evolution.* Ultrasonics sonochemistry, 2015. **23**: p. 142-147.

[10] Islam, M.H., et al., *Sonochemical conversion of CO2 into hydrocarbons: The Sabatier reaction at ambient conditions.* Ultrasonics Sonochemistry, 2021. **73**: p. 105474.

[11] Entezari, M.H. and P. Kruus, *Effect of frequency on sonochemical reactions. I: Oxidation of iodide.* Ultrasonics Sonochemistry, 1994. **1**(2): p. S75-S79.

[12] Nomura, H., et al., *Quantification of ultrasonic intensity based on the decomposition reaction of porphyrin.* Ultrasonics Sonochemistry, 1996. **3**(3): p. S153-S156.

[13] Mark, G., et al., *OH-radical formation by ultrasound in aqueous solution–Part II: Terephthalate and Fricke dosimetry and the influence of various conditions on the sonolytic yield.* Ultrasonics Sonochemistry, 1998. **5**(2): p. 41-52.

[14] Martínez-Tarifa, A., et al., *Salicylic acid dosimetry applied for the statistical determination of significant parameters in a sonochemical reactor.* Chemical Engineering Journal, 2010. **157**(2-3): p. 420-426.

[15] Ebrahiminia, A., M. Mokhtari-Dizaji, and T. Toliyat, *Correlation between iodide dosimetry and terephthalic acid dosimetry to evaluate the reactive radical production*

due to the acoustic cavitation activity. Ultrasonics sonochemistry, 2013. **20**(1): p. 366-372.

[16] Dalodière, E., et al., *Effect of ultrasonic frequency on H2O2 sonochemical formation rate in aqueous nitric acid solutions in the presence of oxygen.* Ultrasonics Sonochemistry, 2016. **29**: p. 198-204.

[17] Rajamma, D.B., et al., *Sonochemical dosimetry: A comparative study of Weissler, Fricke and terephthalic acid methods.* Ultrasonics sonochemistry, 2021. **72**: p. 105413.

[18] Mason, T.J., *Advances in sonochemistry*. 1996: Elsevier.

[19] Fang, X., G. Mark, and C. von Sonntag, *OH radical formation by ultrasound in aqueous solutions Part I: the chemistry underlying the terephthalate dosimeter.* Ultrasonics Sonochemistry, 1996. **3**(1): p. 57-63.

[20] Ashokkumar, M., et al., *Sonochemical degradation of sodium dodecylbenzene sulfonate in aqueous solutions.* Australian journal of chemistry, 2003. **56**(10): p. 1045-1049.

[21] Frenkel, V., et al., *Preliminary investigations of ultrasound induced acoustic streaming using particle image velocimetry.* Ultrasonics, 2001. **39**(3): p. 153-156.

[22] Kumar, A., et al., *Characterization of flow phenomena induced by ultrasonic horn.* Chemical engineering science, 2006. **61**(22): p. 7410-7420.

[23] Elder, S.A., *Cavitation microstreaming.* The Journal of the Acoustical Society of America, 1959. **31**(1): p. 54-64.

[24] Theerthagiri, J., et al., *Sonoelectrochemistry for energy and environmental applications.* Ultrasonics Sonochemistry, 2020. **63**: p. 104960.

[25] Budischak, C., C. Honsberg, and R.L. Opila. *Electroanalytic effects of ultrasound on a hydrogen evolution reaction in KOH*. in *2008 33rd IEEE Photovoltaic Specialists Conference*. 2008. IEEE.

[26] Lin, M.-Y. and L.-W. Hourng, *Ultrasonic wave field effects on hydrogen production by water electrolysis.* Journal of the Chinese Institute of Engineers, 2014. **37**(8): p. 1080-1089.

[27] Shen, Q., et al., *Morphology-controlled synthesis of palladium nanostructures by sonoelectrochemical method and their application in direct alcohol oxidation.* The Journal of Physical Chemistry C, 2009. **113**(4): p. 1267-1273.

[28] Shen, Q., et al., *Three-dimensional dendritic Pt nanostructures: sonoelectrochemical synthesis and electrochemical applications.* The Journal of Physical Chemistry C, 2008. **112**(42): p. 16385-16392.

[29] Pollet, B.G., *The use of ultrasound for the fabrication of fuel cell materials.* international journal of hydrogen energy, 2010. **35**(21): p. 11986-12004.

[30] Wang, C., et al., *Sonoelectrochemical synthesis of highly photoelectrochemically active TiO2 nanotubes by incorporating CdS nanoparticles.* Nanotechnology, 2009. **20**(29): p. 295601.

[31] Balasubramaniam, M. and S. Balakumar, *Ultrasonication-assisted fabrication of hierarchical architectures of copper oxide/zinc antimonate nanocomposites based supercapacitor electrode materials.* Ultrasonics sonochemistry, 2019. **56**: p. 337-349.

[32] Karousos, D.S., et al., *Sonoelectrochemical one-pot synthesis of Pt–Carbon black nanocomposite PEMFC electrocatalyst.* Ultrasonics sonochemistry, 2017. **35**: p. 591-597.

[33] Hansen, H.E., et al., *Two routes for sonochemical synthesis of platinum nanoparticles with narrow size distribution.* Materials Advances, 2021.

[34] Lewis, N.S. and D.G. Nocera, *Powering the planet: Chemical challenges in solar energy utilization.* Proceedings of the National Academy of Sciences, 2006. **103**(43): p. 15729-15735.

[35] Jalili, Z., et al., *Energy generation and storage by salinity gradient power: A model-based assessment.* Journal of Energy Storage, 2019. **24**: p. 100755.

[36] Denholm, P., et al., *Overgeneration from solar energy in california. a field guide to the duck chart*. 2015, National Renewable Energy Lab.(NREL), Golden, CO (United States).

[37] Li, S.-D., C.-C. Wang, and C.-Y. Chen, *Water electrolysis in the presence of an ultrasonic field.* Electrochimica Acta, 2009. **54**(15): p. 3877-3883.

[38] Cheng, H., K. Scott, and C. Ramshaw, *Intensification of water electrolysis in a centrifugal field.* Journal of The Electrochemical Society, 2002. **149**(11): p. D172-D177.

[39] Islam, M.H., O.S. Burheim, and B.G. Pollet, *Sonochemical and sonoelectrochemical production of hydrogen.* Ultrasonics sonochemistry, 2018.

[40] Wang, M., et al., *The intensification technologies to water electrolysis for hydrogen production–A review.* Renewable and Sustainable Energy Reviews, 2014. **29**: p. 573-588.

[41] Islam, M.H., et al., *The effects of power ultrasound (24 kHz) on the electrochemical reduction of CO2 on polycrystalline copper electrodes.* Ultrasonics Sonochemistry, 2021. **72**: p. 105401.

[42] Kerboua, K., O. Hamdaoui, and S. Al-Zahrani, *Sonochemical production of hydrogen: A numerical model applied to the recovery of aqueous methanol waste under o xygen-argon atmosphere.* Environmental Progress & Sustainable Energy, 2021. **40**(2): p. e13511.

[43] Kerboua, K., et al., *How do dissolved gases affect the sonochemical process of hydrogen production? An overview of thermodynamic and mechanistic effects–On the "hot spot theory".* Ultrasonics Sonochemistry, 2021. **72**: p. 105422.

[44] Merouani, S. and O. Hamdaoui, *The sonochemical approach for hydrogen production.* Sustainable Green Chemical Processes and their Allied Applications, 2020: p. 1-29.

[45] Kerboua, K. and O. Hamdaoui, *Energetic challenges and sonochemistry: A new alternative for hydrogen production?* Current Opinion in Green and Sustainable Chemistry, 2019. **18**: p. 84-89.

[46] Rashwan, S.S., et al., *The sono-hydro-gen process (ultrasound induced hydrogen production): challenges and opportunities.* International Journal of Hydrogen Energy, 2019. **44**(29): p. 14500-14526.

[47] Moriguchi, N., *The effect of supersonic waves on chemical phenomena,(III). The effect on the concentration polarization.* J. Chem. Soc. Jpn, 1934. **55**: p. 749-750.

[48] Lepesant, M., *Sonoelectrochemical Production of Hydrogen for PEM Fuel Cell Applications*. 2011.

[49] Zadeh, S.H., *Hydrogen production via ultrasound-aided alkaline water electrolysis.* Journal of Automation and Control Engineering Vol, 2014. **2**(1).

[50] Symes, D., *Sonoelectrochemical (20 kHz) production of hydrogen from aqueous solutions*. 2011, University of Birmingham.

4 Methodology

4.1 Electrochemical Characterization

4.1.1 Electrochemical Set-up Preparation

A three-electrode cell for studying electrocatalysis consists of a working electrode (WE), a counter electrode (CE), a reference electrode (RE) and a gas inlet. In this dissertation, all voltammetry work was performed using a specially designed sono-reactor (Figure 4.1a and 4.1b). This sono-reactor also called the *Besançon cell* [1, 2]. The sono-reactor shown in Figure 4.1a is designed for ultrasound horn and the sono-reactor shown in Figure 4.1b is designed for the plate transducer. In both reactors the ultrasound probe and ultrasound plate transducer are not directly in contact with the electrolyte in order to avoid any contamination. The working volume of the inner cells was 100 mL.

Extensive care was taken to ensure the electrochemical tests were performed with thoroughly cleaned electrolyte and cell since impurities within the system can undergo electrochemical reactions on the surface of the WE or adsorb on the surface of the WE and block surface sites [3]. The electrolyte could be contaminated if the cell was not well cleaned. Therefore, before using the cell, it was essential to establish extensive protocols for cleaning all components in contact with the electrolyte. The following cleaning procedure for glassware was used [4, 5]:

1. Preparation of $KMNO_4$ solution by dissolving 3–4 g of $KMnO_4$ (Sigma Aldrich, ≥ 99.0% in purity) in 1.50 L of ultra-high purity H_2O;
2. Preparation of an aqueous solution of H_2SO_4 by mixing 250 mL of concentrated H_2SO_4 (Sigma Aldrich, ≥ 99.9%) with 250 mL of ultra-high purity H_2O;
3. Allowing the H_2SO_4 solution to cool down and when it reaches the room temperature add to the aqueous $KMnO_4$ solution;
4. Soaking all glassware at least 24 hours in acidified $KMnO_4$ solution;
5. Rinsing of the electrochemical cell and glassware with a “piranha solution” (a solution prepared by mixing 300 mL of 30% by weight H_2O_2, 50 mL of concentrated H_2SO_4 and 50 mL of ultra-high purity H_2O; and,
6. Rinsing the glassware with ultra-high purity water at least 10 times followed by boiling 3 times in a fresh batch of ultra-high purity H_2O (kept at 100°C) at least for 2 hours.

It should be noted that before the six-step cleaning process, all *as*-received glassware needs to be degreased with hot acetone to remove any impurities originating from handling and shipping [5].

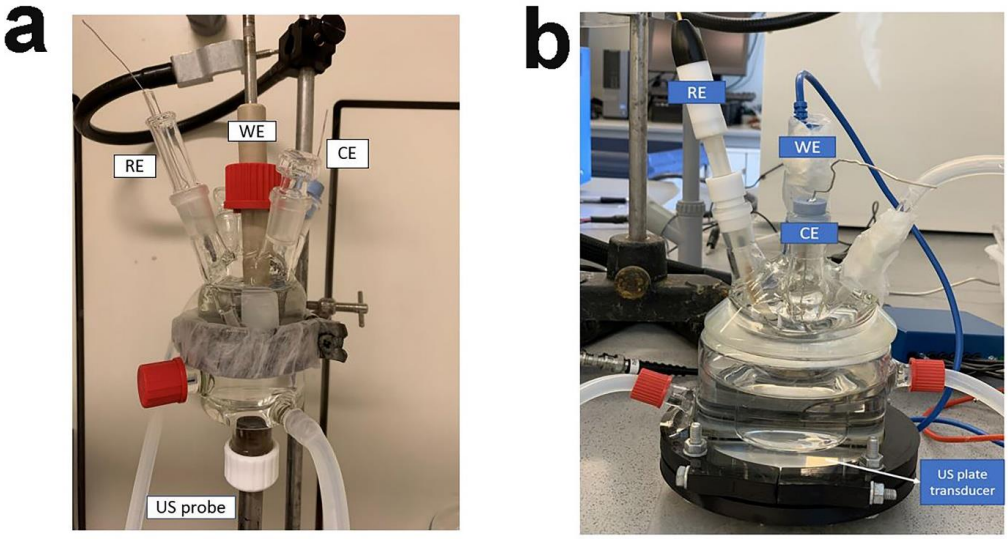

Figure 4.1. Sonoelectrochemical cell set-up for a) 24 kHz and b) 408 kHz ultrasound unit.

4.1.2 Electrochemical Techniques for Materials Testing

When analyzing the electrochemical and physical properties of electrode materials, a wide range of electrochemical, analytical, and materials science techniques was used. Often, electrochemical techniques are used in combination with other experimental techniques to provide a more complete understanding of the system under investigation. In this section, a general introduction to selected electrochemical techniques is presented to familiarize the reader with the experimental methods used in this work.

4.1.2.1 Cyclic Voltammetry

4.1.2.1.1 Cyclic Voltammetry and the Electrochemical Active Surface area of Platinum Electrode

Cyclic voltammetry (CV) profiles recorded in high-purity electrolytes allowed the determination of the potential regions corresponding to the double-layer charging, oxide growth and the under-potential deposition of hydrogen (H-upd). Also, the cleanliness of the

system, the quality of the electrode and electrochemical surface area were verified by recording a CV transient [6]. The term real surface area is equal to the electrochemically active surface area (A_{ecsa}) [7]. Figure 4.2. illustrates a cyclic voltammetric curve of a polycrystalline Pt electrode immersed in 0.5 M H_2SO_4. Three potential ranges can be distinguished here, namely [7]:

a) a region of hydrogen adsorption/desorption (+0.05 – +0.45 V *vs.* RHE);
b) a region of surface oxide formation/reduction (above +0.60 V *vs.* RHE); and,
c) a region free from faradaic processes or double layer region (+0.45 – +0.60 V *vs.* RHE).

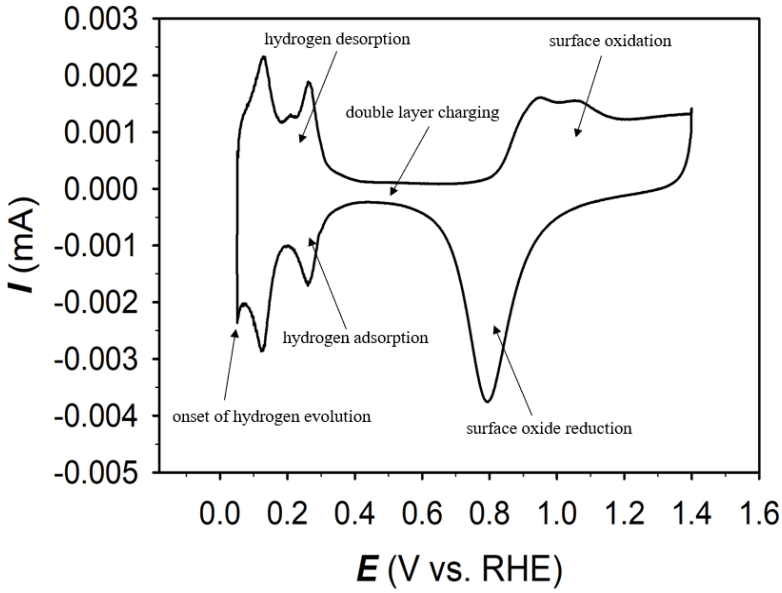

Figure 4.2. Cyclic voltammogram of polycrystalline Pt electrode in N_2-saturated 0.5 M H_2SO_4 at a scan rate of 50 mV s^{-1} (T = 298 K).

The determination of the number of electrons released during the oxidation of Pt for low potentials gives the number of hydrogen atoms (H) desorbed; and, therefore, the number of adsorption sites present on the surface of the electrode. This defines the real surface area or the electrochemical surface area (A_{ecsa}) [8]. The total charge corresponding to the hydrogen desorption can be related to the integral of the curve for a certain interval of potentials where the atoms are being desorbed [8]. This part of the curve is represented in Figure 4.3.

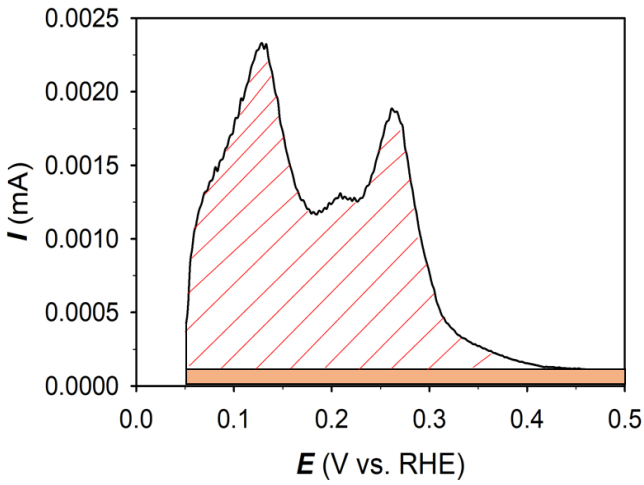

Figure 4.3. Zoom of the curve presented in Figure 4.2 for low potentials in oxidation. The red area corresponds to the desorption of hydrogen. The orange area corresponds to the capacitive current due to the double-layer capacitance.

The expression of the total charge of desorption (Q) can be written as follows [8]:

$$Q = \int_{t_1}^{t_2} I.dt = \frac{1}{v_b}\int_{E_1}^{E_2} I.dE \qquad (4.1)$$

where v_b is the scan rate (V s^{-1}); and I is the current (µA) recorded at potential E (in V *vs.* RHE) in the hydrogen desorption region and t is the time (s). However, the capacitive current due to the double layer capacitance should not be considered, and the corresponding area must be subtracted from the integral. Then the electrochemical surface area (A_{ecsa}) in cm^2 can be calculated as follows:

$$A_{\text{ecsa}} = \frac{Q}{Q_{\text{monolayer}}} \qquad (4.2)$$

where Q *is* the total charge of desorption (µC) determined by equation (4.1); $Q_{monolayer}$ is the coulombic charge related to the adsorption or desorption of a hydrogen monolayer on a polycrystalline Pt surface. In the literature, the electrical charge generally associated with monolayer adsorption/desorption of hydrogen is 210 µC cm^{-2} [9, 10].

4.1.2.1.2 Cyclic Voltammetry and the Electrochemical Active surface Area of Nickel

It has been shown that determining the electrochemical active surface area (A_{ecsa}) of Ni-based materials is challenging and is not as straightforward as Pt [11-13].

In this dissertation [11-13], three methods for determining A_{ecsa} of Ni electrodes have been employed. All tested methods were performed in an alkaline environment and were based upon:

1. the α-$Ni(OH)_2$ oxidation peak (the "Alpha Method");
2. the double layer capacitance obtained through non-faradaic charging by cyclic voltammetry (the "Capacitance Method") as well as the charge association; and
3. the β-NiOOH reduction peak (the "Beta Method")

Recently, Baranova and her group [12] compared these three methods for various Ni nanostructures. Each method has both advantages and disadvantages. For example, the "Alpha Method" provides an accurate determination of the A_{ecsa} but cannot be applied to Ni oxide electrodes. The "Beta Method" is only desirable when working on the OER because it requires the transition into the Ni^{3+} state. Moreover, like the "Alpha Method," it is not a suitable method for Ni oxide species. The "Capacitance Method" is the best to use for Ni composite materials because it does not change the nature of the electrode surface; there are no additional species required in the electrolyte, and it does not use any transition peaks specific to Ni to calculate the A_{ecsa}.

For the determination of A_{ecsa} of polycrystalline Ni by the "Alpha Method," it is required to form α-$Ni(OH)_2$ on the electrode surface and reduce it to metallic Ni [11]. Alsabet *et al.* [11] developed "Alpha Method" by recording CV profiles at T = 298 K and a scan rate of 100 mV s^{-1} between −0.15 and +0.5 V *vs.* RHE in 0.5 M KOH. The lower potential limit of −0.15 V vs. RHE and the scan rate of 100 mV s^{-1} is selected in order to minimise any additional current density due to the HER. Then, the value of A_{ecsa} for the Ni electrode is calculated by using equation (4.3) [11].

$$A_{ecsa} = \frac{Q_{ox}}{Q_{monolayer,ox}} \qquad (4.3)$$

where Q_{ox} is the experimentally determined charge of α-Ni(OH)$_2$ formation and reduction. The area is illustrated in Figure 4.4. $Q_{monolayer,ox}$ is the charge density associated with the formation of one monolayer of α-Ni(OH)$_2$, which is determined to 514 μC cm^{-2} in literature [14].

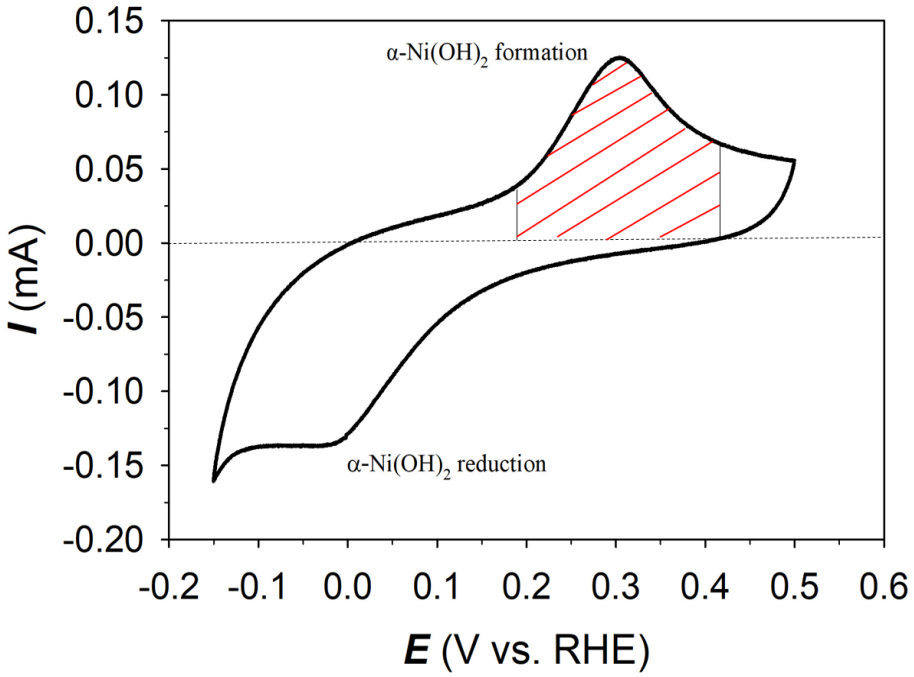

Figure 4.4. The Alpha Method: Example of the integration area for polycrystalline Ni from Cycle 10 of a CV in 1.0 M aqueous KOH solution recorded at a scan rate of v = 100 mV s^{-1}.

The real surface area of Ni electrodes can be calculated by the "Capacitance Method" in two ways [11]. The first way proposed by Alsabet *et al*. is [11] based upon double-layer capacitance (C_{dl}) measurements and employing electrochemical impedance spectroscopy (EIS) at a constant potential that is in the region of HER ($-0.20 \leq E \leq +0.25$ V *vs.* RHE) and at T = 298 K in 0.5 M KOH. The Ni electrode is free of any surface oxides under these conditions. The frequency of the AC signal is in the 0.5 Hz $\leq f \leq$ 100 kHz range. The obtained C_{dl} value is used to determine the electrode real surface area by using the specific capacitance to be 20 μF cm^{-2} [15]. In the second way suggested by Cossar *et al*. [12], the "Capacitance Method" consists of cycling the Ni-based electrodes at different scan rates in a non-faradaic charging

process. In their study, this method was performed on a freshly polished electrode in 0.10 M KOH. They carried out a series of CVs at different scan rates (5, 10, 20, 50, 100, 150, 200, 300 and 400 mV s^{-1}) ± 50 mV around the open circuit potential (OCP) that is particular for each electrode. With the data from the CVs, it is possible to determine the charging current (I_c) of the electrodes at each scan rates, as shown by equation (4.4) [12]:

$$I_c = (I_{anodic} - I_{cathodic})_{OCP} \qquad (4.4)$$

By plotting a graph of charging current (A) *vs.* scan rate (V s^{-1}) and calculating the slope, C_{dl} (F) can be obtained as shown by equation (4.5) [12]:

$$Slope = C_{dl} = \frac{\Delta I_c}{\Delta v} \qquad (4.5)$$

Finally, the real surface area can be calculated using the specific capacitance density (c) of 40 μF cm^{-2} [16] and equation (4.6) [12]:

$$A_{ecsa} = \frac{C_{dl}}{c} \qquad (4.6)$$

For all materials, the roughness factor (RF) can be measured by equation (4.7):

$$RF = \frac{A_{ecsa}}{A_{geom}} \qquad (4.7)$$

where A_{ecsa} (cm^2) is the electrochemical surface area; and A_{geom} (cm^2) is the geometric surface area.

The "Beta Method" consists of integrating the β-NiOOH reduction peak once steady state polarization is reached at a high scan rate. The "Beta Method" is carried out by running 10 CV cycles from $+0.50 \leq E_{app} \leq +1.60$ V *vs.* RHE at scan rate of $v = 100$ mV s^{-1} (Figure 4.5). The A_{ecsa} values for this method are calculated using the β-NiOOH reduction peak of the 10^{th} cycle (from +1.2 to +1.4 V *vs.* RHE) divided by the specific charge density of 420 μC cm^{-2} (equation 4.8) [12].

$$A_{\text{ecsa}} = \frac{Q_{ox}}{420} \qquad (4.8)$$

where Q is the charge associated with the β-NiOOH reduction peak.

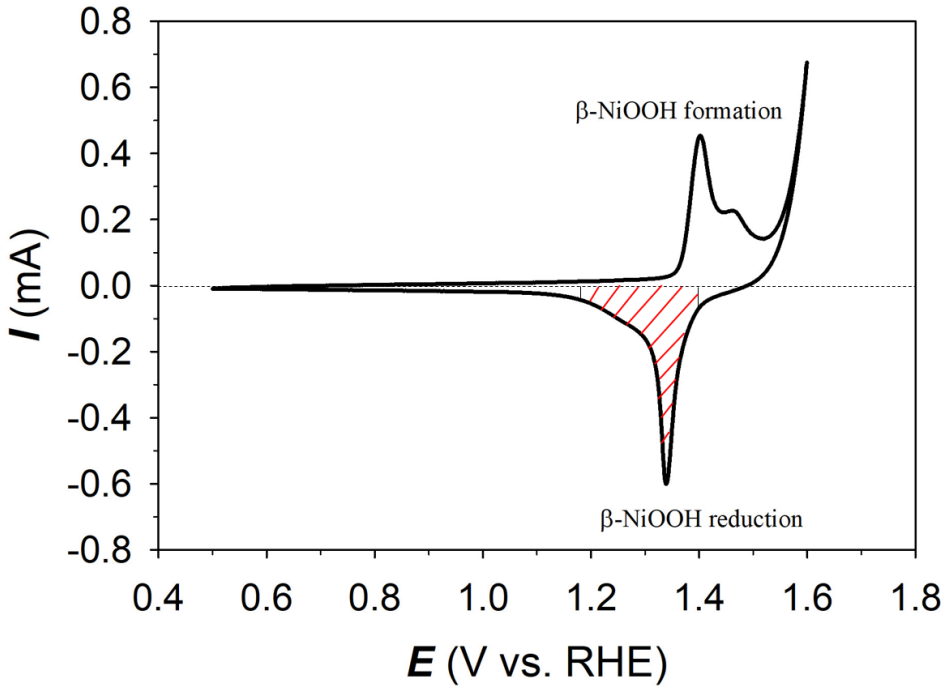

Figure 4.5. The "Beta Method": Example of the integration area for a polished polycrystalline Ni electrode from cycle 10 of a CV in 1.0 M aqueous KOH solution recorded at a scan rate of ν =100 mV s^{-1}.

4.1.2.2 Electrochemical Impedance Spectroscopy (EIS)

Among the various electrochemical techniques, electrochemical impedance spectroscopy (EIS) holds a special place. The classical electrochemical techniques present measurements of currents, electrical charges, or electrode potentials as functions of time (which can also be related to the electrode potential). In contrast, EIS presents the signal as a function of frequency at a constant potential. EIS is usually used for fine-tuning mechanisms and determining the kinetics of processes, resistances, and capacitances, and it allows for the determination of real surface areas in situ [17]. EIS has numerous applications. It is used in the following types of studies [17]:

1. Interfacial processes: redox reaction at electrodes, adsorption and electrosorption, kinetics of homogeneous reactions in solution combined with redox processes, forced mass transfer.
2. Geometric effects: linear, spherical, cylindrical mass transfer, limited-volume electrodes, determination of solution resistance, porous electrodes
3. Applications in power sources (batteries, fuel cells, supercapacitors, membranes), corrosion, coatings and paints, electrocatalytic reactions (e.g., water electrolysis, Cl_2 evolution), conductive polymers, self-assembled monolayers, biological membranes, sensors, semiconductors, and others.

Impedance measurements produce numerical results, usually as *real* impedance (Z') and *imaginary* impedance (Z'') or modulus $|Z|$ and phase angle φ as functions of frequency. Visual (graphical) inspection of the obtained results usually makes it possible to identify the electrical equivalent circuit containing resistance (R), capacitance (C), and inductance (L) elements [17].

There are two fundamental types of graph [17]:

1. Complex plane plots, also called Nyquist plots. They are plots of imaginary versus real impedance. In these plots $-Z''$ is plotted versus Z' as the imaginary impedances of the electrochemical systems are usually negative.
2. Bode plots. There are two types of Bode plot: (a) log $|Z|$ (magnitude) versus log f (frequency) (b) phase angle φ versus log f

4.1.2.3 Linear Sweep Voltammetry (LSV)

The catalytic activity of each electrocatalyst towards the HER and the OER can be measured by the LSV. To understand the "real" potential applied on the catalysts, it is required to correct the potential drop caused by ohmic losses [18] due to the ionic conduction in the electrolyte between the working and reference electrodes, in addition to any contact resistances. Although many Potentiostat offer the option to correct for the uncompensated resistance during the measurement (often dynamically), it is well-know that sometimes the Potentiostat may run into resonance, which could lead to unusable data and may even damage the hardware or electrodes if no voltage limits are set in the Potentiostat [19, 20]. Hence, it is highly recommended to use EIS to measure R and manually correcting IR according to the equation 4.9 [20].

$$E_{\text{IR-corrected}} = E_{app} - IR \qquad (4.9)$$

where I is the measured current and R is the electrolyte resistance. The R value was determined by electrochemical impedance spectroscopy (EIS) in the high frequency region from the value of the *real* impedance (Z') where the *imaginary* impedance (Z'') is zero in Nyquist plot.

After *IR*-correction, the extracted kinetic current is normalized by using the A_{ecsa} to yield the specific activity (j_s) or normalized by using the loading mass of catalyst materials to lead to the mass activity (j_m) [20].

The overpotential at ±10 mA cm^{-2} ($\eta_{\pm 10\text{ mA cm}^{-2}}$) are regarded as critical factors to assess HER and OER activity, which can be obtained from LSV [21]. The ±10 mA cm^{-2} value can be associated to the current drawn by a solar-to-fuel device with about 10% efficiency under the illumination of AM1.5G ("one sun") [20].

The activity can also be compared by the exchange current density (j_o) [20]. Exchange current density defines the current density that flows equally in equilibrium and in both directions. The exchange current represents the rates of both oxidation and reduction for a given single electrode at equilibrium [22]. The larger the exchange current density, the faster the reaction. The j_o of the HER is obtained by extrapolation of the Tafel plot to $\eta = 0.00$ V *vs.* RHE [20].

We should now consider the analysis of a "good" and a "poor" electrocatalyst using the Tafel plot method, *i.e.*, the plot of η *vs.* ln j (a generic plot is presented on Figure 4.6 to aid in the analysis). A good electrocatalyst is a material that exhibits large values of j_o and requires a small η for a significant increase in the value of j. Mathematically speaking, a good electrocatalyst shows a large y-axis intercept value and small linear slope. Conversely, a poor electrocatalyst is a material that exhibits small j_o values (small y-axis intercept value) and needs a large η for an increase in the value of j (large linear slope). In addition, it is desirable that an electrocatalyst is durable for long term applications, and that its bond strength with the reactant and product species is not too strong to the point that the active sites are permanently blocked, thus hindering the rate of the electrochemical reaction.

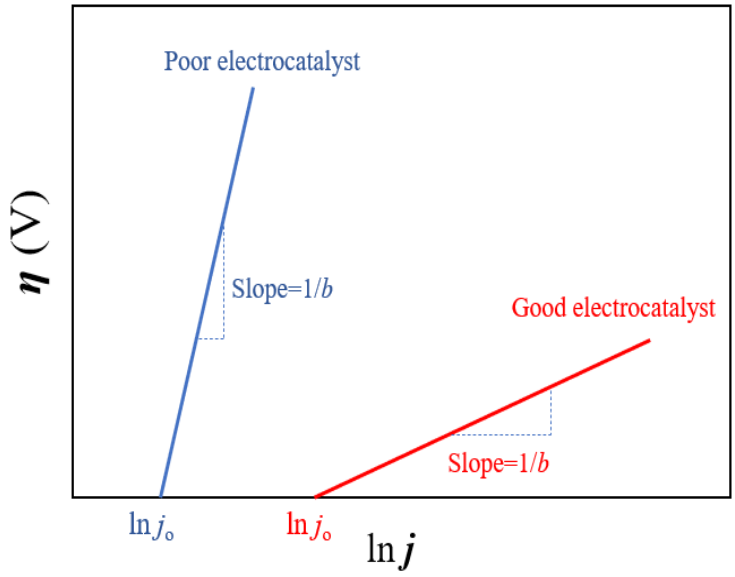

Figure 4.6. Schematic representation of Tafel polarization plots for a good (red line) and a poor (blue line) electrocatalyst.

4.2 Sonoelectrochemical Setup

Ultrasound can be applied into a system by either immersing the ultrasonic source in the reaction medium (direct ultrasonication) or by dipping a vessel containing the reaction mixture into a tank containing an ultrasonicated liquid, generally water (indirect ultrasonication). In either case, ultrasound must be generated through a piece of equipment whose design includes a transducer system based upon either a vibrating plate or a probe (which can have a variety of differently shaped horns to transmit the energy) [23].

In this study, ultrasonication was applied using ultrasonic probes (ultrasonic frequency f = 26 kHz, Hielscher UP200Ht, 200 W, tip ∅ = 7 mm, tip area = 38.48 mm^2) (Figure 4.7a), (ultrasonic frequency f = 24 kHz, Hielscher UP200S, 200 W, 24 kHz the tip diameter of ∅ = 14 mm, and the tip area = 153.9 mm^2) (Figure 4.7b), and a plate transducer vibrating at an ultrasonic frequency f = 408 kHz powered by a multi-frequency ultrasonic generator (Meinhardt Ultrasonics) shown in Figure 4.7c. The sono-reactors that attached to the ultrasound units are shown and described earlier in Figure 4.1.

A refrigerated circulator (JULABO, Germany) was connected to the reactors in order to keep the reactor at a constant temperature (Figure 4.8).

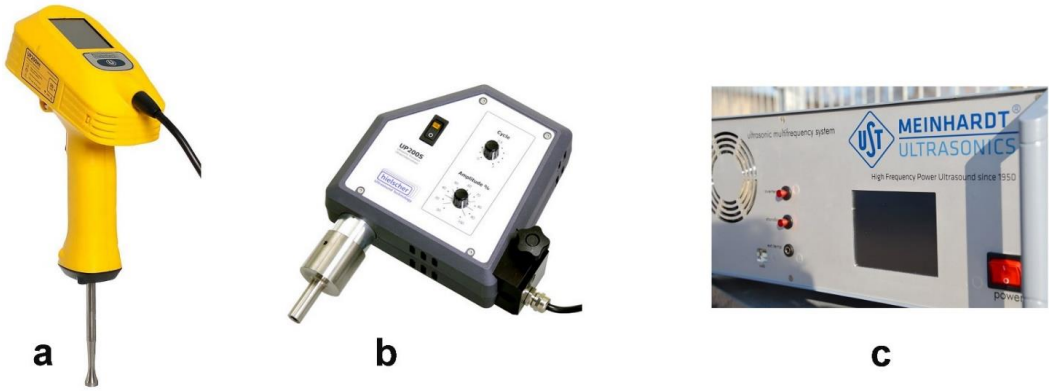

Figure 4.7. Ultrasonic probe transducers a) 26 kHz, b) 24 kHz and c) multi-frequency ultrasonic generator.

Figure 4.8. Refrigerator circulator**.**

4.2.1 Dosimetry

To characterise the sonochemical activity of our sono-reactor at certain conditions (24 kHz, 44 ± 1.40 W, 60% amplitude power, 298 K), a dosimetry experiment was performed [24]. In this experiment, 100 mL of 1.0 M aqueous KOH solution were sonicated for 105 minutes at the selected conditions. During sonication, a 0.5 mL aliquot of the solution was sampled every 15 min, and diluted with a 0.5 mL $TiOSO_4$ solution (2×10^{-2} M, sigma-Aldrich) [25]. The as-formed peroxotitanium(IV) complex exhibiting was then analysed by a Thermo Scientific Evolution UV-Visible absorption spectrophotometer.

4.2.1.1 **UV-Vis Spectroscopy**

A UV-Vis spectrophotometer (Thermo Scientific Evolution) was used to analyse the samples for the dosimetry. By determining the maximum absorption wavelength, λ_{max}, it was possible to determine the unknown concentration of the specific compound present in the solution by using the *Beer-Lambert law* (4.10).

$$A = \varepsilon l c \qquad (4.10)$$

where A is the absorption (dimensionless), ε is the molar absorption coefficient (M^{-1} cm^{-1}), l is the path length of light (cm), c is the concentration of the absorbing species (M). Here, a molar absorption coefficient of 787 M^{-1} cm^{-1} was used [26].

4.2.2 Acoustic Power Measurement

Transmitted acoustic power measurements were carried out by ultrasonicating 100 mL ultrapure water for 1 min. The temperature increase, due to the conversion of mechanical energy into heat, was recorded every second by using a National Instruments thermocouple controlled by a LabView software. The ultrasonic or acoustic power (P_{acous}) were determined calorimetrically using the methods of Margulis *et al.* [27] and Contamine *et al*. [28] (equation 4.11)

$$P_{US} = mC_{p,s}\left(\frac{dT}{dt}\right) \qquad (4.11)$$

where, m is the mass of water (g), $C_{p,s}$ is the specific constant pressure heat capacity of water (J g^{-1} K^{-1}) and $\frac{dT}{dt}$ is the temperature increase after sonication time t.

4.2.3 High-Speed Camera Imaging

All high-speed imaging water electrolysis experiments were performed using a Photron SA 5 camera, at a frame rate of 10,000 frames per second (fps) using diffused back-lit illumination (Figure (4.9)). The light source was a high-power single-chip LED (CBT 120) with light collimated onto an engineered diffusor (ThorlabsED1-C50) placed behind the sonoelectrochemical cell. A short exposure time of 1 ms was applied at a resolution of 896 x 848. The camera was fitted with a Nikon 60 microlens and the resulting region that could be imaged was approx. 25 mm^2 and a record length of 2 seconds.

Figure 4.9. Ultra-high speed camera (Photron SA 5).

4.3 Electrode Surface Characterisation

4.3.1 Raman Spectroscopy

Raman spectroscopy is a spectroscopic technique typically used to determine vibrational modes of molecules. Raman spectroscopy is commonly used in chemistry to provide a structural fingerprint by which molecules can be identified. Raman spectroscopy relies upon the inelastic scattering of photons, known as Raman scattering. A source of monochromatic light, usually from a laser in the visible, near-infrared, or near ultraviolet range is used, although X-rays can also be used. The laser light interacts with molecular vibrations, phonons, or other excitations in the system, resulting in the energy of the laser photons being shifted up or down. The shift in energy gives information about the vibrational modes in the system [29, 30].

In our study, *ex-situ* Raman spectroscopy analysis was performed using a WITec alpha 300 R Confocal Raman spectrometer equipped with a 532 nm laser with a power of 5.0 mW (Figure 4.10). The Raman spectrometer was coupled with a Zeiss EC Epiplan 10× objective

and G1: 600 g/mm BLZ = 500 nm grating. Raman spectra were obtained after 10 accumulations for 10 sec from 100 to 1,250 cm^{-1}.

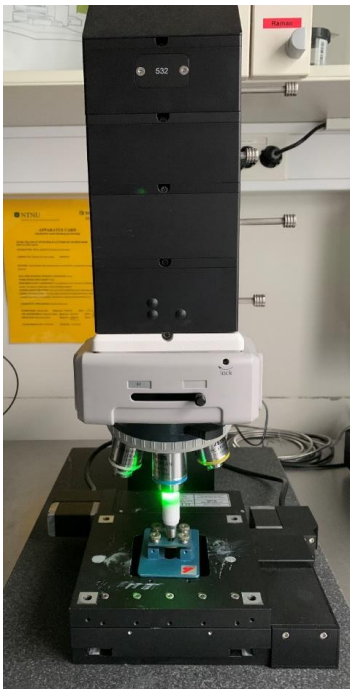

Figure 4.10. WITec alpha 300 R Confocal Raman spectrometer.

4.3.2 Scanning Electron Microscopy

The scanning electron microscope (SEM) uses a focused beam of high-energy electrons to generate a variety of signals at the surface of solid specimens. The signals that derive from electron sample interactions reveal information about the sample including external morphology (texture), chemical composition, crystalline structure and orientation of materials making up the sample. In most applications, data are collected over a selected area of the surface of the sample, and a 2-dimensional image is generated that displays spatial variations in these properties. Areas ranging from approximately 1 cm to 5 microns in width can be imaged in a scanning mode using conventional SEM techniques (magnification ranging from 20X to approximately 30,000X, spatial resolution of 50 to 100 nm). The SEM is also capable of performing analyses of selected point locations on the sample; this approach is especially useful in qualitatively or semi-quantitatively determining chemical compositions (using EDS) in which the characteristic X-rays are captured by an X-ray detector to perform energy

dispersive X-ray spectroscopy [31, 32]. In this dissertation, the surface morphology of the polycrystalline Ni electrode before and after ultrasound treatment were studied using Zeiss-Ultra 55-FEG-SEM operating at 10 kV accelerating voltage (Figure 4.11). For the inspection of the Raney-Ni electrodes' cross-section SEM measurements were performed at Fraunhofer IFAM using a Jeol JSM F100 equipped with a field emission gun coupled to a Bruker Quantax 200 EDS spectrometer.

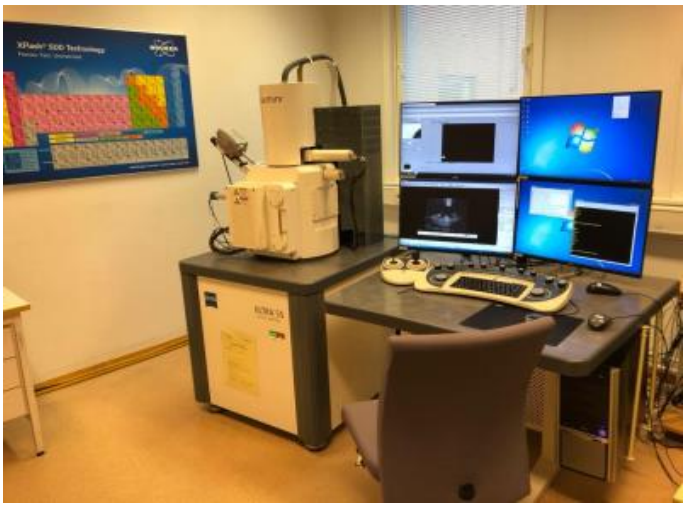

Figure 4.11. Zeiss - Ultra 55 - FEG-scanning electron microscope (SEM).

References

[1] Pollet, B.G., *Power ultrasound in electrochemistry.* Wiley Online Library, 2012.

[2] Pollet, B.G. and M. Ashokkumar, *Introduction to Ultrasound, Sonochemistry and Sonoelectrochemistry*. 2019: Springer Nature.

[3] Conway, B., et al., *Ultrapurification of water for electrochemical and surface chemical work by catalytic pyrodistillation.* Analytical Chemistry, 1973. **45**(8): p. 1331-1336.

[4] Sluyters-Rehbach, M., J. Sluyters, and E. Yeager, *Comprehensive treatise of electrochemistry.* by E. Yeager, J. O'M. Bockris, BE Conway, and S. Sarangapani, Plenum Press, New York, 1984. **9**.

[5] Arulmozhi, N., et al., *Design and Development of Instrumentations for the Preparation of Platinum Single Crystals for Electrochemistry and Electrocatalysis Research Part 3: Final Treatment, Electrochemical Measurements, and Recommended Laboratory Practices.* Electrocatalysis, 2018. **9**(1): p. 113-123.

[6] Jerkiewicz, G., et al., *Surface-oxide growth at platinum electrodes in aqueous H2SO4: Reexamination of its mechanism through combined cyclic-voltammetry, electrochemical quartz-crystal nanobalance, and Auger electron spectroscopy measurements.* Electrochimica Acta, 2004. **49**(9-10): p. 1451-1459.

[7] Łukaszewski, M., M. Soszko, and A. Czerwiński, *Electrochemical methods of real surface area determination of noble metal electrodes–an overview.* Int. J. Electrochem. Sci, 2016. **11**(6): p. 4442-4469.

[8] Doña Rodríguez, J.M., J.A. Herrera Melián, and J. Pérez Peña, *Determination of the real surface area of Pt electrodes by hydrogen adsorption using cyclic voltammetry.* Journal of Chemical Education, 2000. **77**(9): p. 1195.

[9] Daubinger, P., et al., *Electrochemical characteristics of nanostructured platinum electrodes–a cyclic voltammetry study.* Physical Chemistry Chemical Physics, 2014. **16**(18): p. 8392-8399.

[10] Zeng, M. and Y. Li, *Recent advances in heterogeneous electrocatalysts for the hydrogen evolution reaction.* Journal of Materials Chemistry A, 2015. **3**(29): p. 14942-14962.

[11] Alsabet, M., M. Grden, and G. Jerkiewicz, *Electrochemical growth of surface oxides on nickel. Part 1: formation of α-Ni (OH) 2 in relation to the polarization potential, polarization time, and temperature.* Electrocatalysis, 2011. **2**(4): p. 317-330.

[12] Cossar, E., et al., *Comparison of electrochemical active surface area methods for various nickel nanostructures.* Journal of Electroanalytical Chemistry, 2020: p. 114246.

[13] Stern, L.-A. and X. Hu, *Enhanced oxygen evolution activity by NiOx and Ni (OH) 2 nanoparticles.* Faraday discussions, 2015. **176**: p. 363-379.

[14] Machado, S.A. and L. Avaca, *The hydrogen evolution reaction on nickel surfaces stabilized by H-absorption.* Electrochimica acta, 1994. **39**(10): p. 1385-1391.

[15] Zoltowski, P., *The capacity of monocrystalline nickel electrode in potassium hydroxide solution at low hydrogen overpotentials.* Electrochimica acta, 1993. **38**(14): p. 2129-2133.

[16] McCrory, C.C., et al., *Benchmarking hydrogen evolving reaction and oxygen evolving reaction electrocatalysts for solar water splitting devices.* Journal of the American Chemical Society, 2015. **137**(13): p. 4347-4357.

[17] Lasia, A., *Electrochemical impedance spectroscopy and its applications*, in *Modern aspects of electrochemistry*. 2002, Springer. p. 143-248.

[18] van der Vliet, D., et al., *On the importance of correcting for the uncompensated Ohmic resistance in model experiments of the Oxygen Reduction Reaction.* Journal of Electroanalytical Chemistry, 2010. **647**(1): p. 29-34.

[19] Hong, W. and M. Risch, *K. a. Stoerzinger, A. Grimaud, J. Suntivich and Y. Shao-horn.* Energy Environ. Sci, 2015. **8**: p. 1404-1427.

[20] Wei, C., et al., *Recommended practices and benchmark activity for hydrogen and oxygen electrocatalysis in water splitting and fuel cells.* Advanced Materials, 2019. **31**(31): p. 1806296.

[21] Chen, Z., et al., *Recent advances in transition metal-based electrocatalysts for alkaline hydrogen evolution.* Journal of Materials Chemistry A, 2019. **7**(25): p. 14971-15005.

[22] Barbir, F., *PEM fuel cells: theory and practice*. 2012: Academic Press.

[23] Berlan, J. and T.J. Mason, *Sonochemistry: from research laboratories to industrial plants.* Ultrasonics, 1992. **30**(4): p. 203-212.

[24] Gong, C. and D.P. Hart, *Ultrasound induced cavitation and sonochemical yields.* The Journal of the Acoustical Society of America, 1998. **104**(5): p. 2675-2682.

[25] Dalodière, E., et al., *Effect of ultrasonic frequency on H2O2 sonochemical formation rate in aqueous nitric acid solutions in the presence of oxygen.* Ultrasonics sonochemistry, 2016. **29**: p. 198-204.

[26] Iida, Y., et al., *Sonochemistry and its dosimetry.* Microchemical Journal, 2005. **80**(2): p. 159-164.

[27] Margulis, M. and I. Margulis, *Calorimetric method for measurement of acoustic power absorbed in a volume of a liquid.* Ultrasonics Sonochemistry, 2003. **10**(6): p. 343-345.

[28] Contamine, R.F., et al., *Power measurement in sonochemistry.* Ultrasonics Sonochemistry, 1995. **2**(1): p. S43-S47.

[29] Graves, P. and D. Gardiner, *Practical raman spectroscopy.* Springer, 1989.

[30] Agostini, G. and C. Lamberti, *Characterization of semiconductor heterostructures and nanostructures*. 2011, Elsevier.

[31] Abd Mutalib, M., et al., *Scanning electron microscopy (SEM) and energy-dispersive X-ray (EDX) spectroscopy*, in *Membrane characterization*. 2017, Elsevier. p. 161-179.

[32] Kara, U., et al., *Scanning electron microscopy (SEM), energy-dispersive X-ray (EDX) spectroscopy and nuclear radiation shielding properties of [α-Fe3+ O (OH)]-doped lithium borate glasses.* Applied Physics A, 2020. **126**(7): p. 1-14.

5 PAPER 1: Does power ultrasound (26 kHz) affect the hydrogen evolution reaction (HER) on Pt polycrystalline electrode in a mild electrolyte?

Bruno G. Pollet[1*], Faranak Foroughi[1], Alaa Y. Faid[2], David R. Emberson[3] and Md. H. Islam[1]

[1] Hydrogen Energy and Sonochemistry Research Group, Department of Energy and Process Engineering, Faculty of Engineering, Norwegian University of Science and Technology (NTNU), NO-7491 Trondheim, Norway

[2] Electrochemistry Research Group, Department of Materials Science and Engineering, Faculty of Natural Sciences. Norwegian University of Science and Technology (NTNU), NO-7491 Trondheim, Norway

[3] Combustion Kinetics Group, Department of Energy and Process Engineering, Faculty of Engineering, Norwegian University of Science and Technology (NTNU), NO-7491 Trondheim, Norway

Authors to whom correspondence should be addressed: *bruno.g.pollet@ntnu.no

Abstract

In this study, we investigated the effects of power ultrasound (26 kHz, up to ~75 W/cm^2, up to 100% acoustic amplitude, ultrasonic horn) on the hydrogen evolution reaction (HER) on a platinum (Pt) polycrystalline disc electrode in 0.5 M H_2SO_4 by cyclic and linear sweep voltammetry at 298 K. We also studied the formation of molecular hydrogen (H_2) bubbles on a Pt wire in the absence and presence of power ultrasound using ultra-fast camera imaging. It was found that ultrasound significantly increases currents towards the HER i.e., a ~250% increase in current density was achieved at maximum ultrasonic power. The potential at a current density of -10 mA/cm^2 under *silent* conditions was found to be -46 mV and decreased to -27 mV at 100% acoustic amplitude i.e., a ΔE shift of ~+20 mV, indicating the influence of ultrasound on improving the HER activity. A nearly 100% increase in the exchange current density (j_o) and a 30% decrease in the Tafel slope (b) at maximum ultrasonic power, was observed in the low overpotential region, although in the high overpotential region, the Tafel slopes (b) were not significantly affected when compared to *silent* conditions. In our conditions, ultrasound did not greatly affect the "real" surface area (A_r) and roughness factor (R) i.e. the microscopic surface area available for electron transfer. Overall, it was found that ultrasound did not dramatically change the mechanism of HER but instead, increased currents at the Pt surface area through effective hydrogen bubble removal.

Keywords: Ultrasound; sonoelectrochemistry; hydrogen evolution reaction; platinum; bubble overpotential

5.1 Introduction

Electrochemical water splitting technologies for hydrogen generation will play a key role in meeting climate change targets [1]. Currently, ca. 4% of the global hydrogen production is produced through water electrolysis using water electrolysers, whilst 96% is produced through Steam Methane Reforming (SMR) [2]. Electrochemical water splitting is a process in which, a direct current (DC) is passed through two electrodes in an aqueous solution by applying a cell voltage (V_{cell}), whereby di-oxygen (O_2) and di-hydrogen (H_2) gases are generated at the anode and cathode, respectively [3-10].

Based upon the type of electrolytes, separators, working temperatures and pressures employed, there are currently four water electrolyser technologies, namely: (i) Alkaline Water Electrolyser (AWE, aqueous KOH or NaOH, NiO, <80 °C, <30 bar), (ii) Proton Exchange Membrane Water Electrolyser (PEMWE, liquid water, perfluorosulfonic acid (PFSA), <80 °C, <200 bar), (iii) Solid Oxide Water Electrolyser (SOWE, water steam, yttrium-stabilized zirconia (YSZ), 500-850 °C, atmospheric), and (iv) Molten Carbonate Water Electrolyser (MCWE, molten sodium and potassium carbonate, 600-700 °C, 1-8 bar) [3, 4, 10].

PEMWEs and AWEs are the most commercially available and used electrolysers for producing "green" hydrogen, as they both offer many advantages such as: well-established technologies, ease of use, compact system design, quick response, high dynamic operations, high current densities, greater H_2 production rate of acceptable purity (99.99%) and fairly high energy efficient (80–90% for PEMWE and 70–80% for AWE) [8]. However, they both suffer from molecular hydrogen and oxygen bubble accumulation at the electrode surfaces and in the electrolyte, leading to a high ohmic voltage drop (IR) and a large reaction overpotential (η), in turn yielding high operational energy consumption and costs [11, 12].

Unfortunately, H_2 and O_2 gas bubble evolutions during electrochemical water splitting are unavoidable phenomenon yielding electrochemical losses. This is due to the fact that the electrochemical reaction rates for both reactions are purely controlled by the interfacial phenomenon in the three-phase zone (TPZ) where H_2 and O_2 gas bubbles, electrolyte and electrode surface are in contact with each other [12].

V_{cell} for electrochemical water splitting technologies is shown in equation (5.1) [3, 4].

$$V_{cell} = |Ec - Ea| + I \times \sum R = E^{rev} + |\eta_a| + |\eta_c| + I \times (R_c + R_m + R_b + R_e) \quad (5.1)$$

where E_c (or E_{HER}) is the cathode potential for the hydrogen evolution reaction (HER), E_a (or E_{OER}) is the anode potential for the oxygen evolution reaction (OER), I is the applied current, $\sum R$ is total ohmic resistance, E^{rev} is the reversible potential (*Nernst*), η_a is the anode overpotential, η_c is the cathode overpotential, R_c is the circuit resistance, R_m is the membrane/separator resistance, R_b is the bubble resistance, and R_e is the electrolyte resistance [11].

Equation (5.1) shows that V_{cell} is greatly dependent upon the overpotential and ohmic voltage drop and therefore, minimizing η_a, η_c and $\sum R$ is paramount to minimise energy consumption. During water electrolysis, R_c and R_m are usually constant and can be reduced by better wire connection and membrane (or separator) optimisation. However, it is not the situation for R_b as many evolved gas bubbles generated on the electrode surface act as a "passivation layer" i.e., an insulating layer, which significantly reduces the effective electrode surface area (A_{eff}). In this case, the bubble coverage (Θ) on the electrode surface leads to increased bubble resistance, R_b. This fraction of the electrode surface covered with "sticking" gas bubbles is well-known to affect substantially: (i) the mass (m) and heat (h) transfer, (ii) the limiting current density (j_{lim}), (iii) the overpotential (η) and (iv) $\sum R$. In other words, when the evolved gas bubbles cover the electrode surface, they cause electrolyte access blockage and yield reactant starvation resulting to an exponential increase of V_{cell} with the current density (j). Additionally, the dispersion of the bubbles in the electrolyte decreases its conductivity and in turns increases R_e and thus, the current distribution on the electrode surface increases yielding high cell voltages [11-17].

In a typical low-temperature water electrolyser, V_{cell} is ca. 1.8 – 2.0 V at an operating current density of ca. 100 – 300 mA/cm^2, a value which is much higher than the theoretical cell voltage of 1.229 V, yielding a ($\Sigma\eta + \Sigma R$) of ca. +571 – +771 mV, mainly caused by H_2 and O_2 gas evolution processes. The gas bubbles should therefore be removed from the TBZ as rapidly as possible. There are several methods for reducing the total overpotential and total ohmic resistance in water electrolysis, for example, by either increasing the electrolyte flowrate, by using gravity, or by using a magnetic field on the gas-evolving electrodes [11, 12].

Another method is to apply power ultrasound. Power ultrasound (PUS) is a well-defined sound wave in the range 20 kHz – 2 MHz (10 – 1,000 W/cm^2) and it is regarded as the effect of the sound wave on the medium. It is now well-known that PUS used in electrochemistry causes: (a) an area of intense mixing at the vicinity of the ultrasonic transducer, (b) electrolyte degassing, (c) electrode surface activation, cleaning and erosion, (d) an increase in electrolyte

bulk temperature, (e) cavitation, (f) sonolysis (i.e. the production of highly reactive radicals) and (g) sono(electrochemi)luminescence [18-23].

In 2011, it was observed by Pollet and co-workers at the *Birmingham PEM Fuel Cell research group* that PUS could efficiently remove molecular hydrogen and oxygen bubbles from the electrolyte and electrode surfaces in turn enhancing hydrogen and oxygen electrochemical production rates [24, 25]. Lepesant [24] and other researchers such as Symes [25] and Zadeh [26] from the same research group, studied the effects of PUS on the sonoelectrolytic (20 kHz) hydrogen production from mild acidic and alkaline electrolytes on various electrode material types. They observed that PUS increased the hydrogen and oxygen production rates due to the efficient electrode cleaning, and electrode surface/solution degassing and enhanced mass transfer of electroactive species to the electrode surface. Recently Islam *et al.* [27] reviewed the area in a paper entitled "sonochemical and sonoelectrochemical production of hydrogen" and showed that PUS can be a powerful tool to overcome the limitations of electrochemical water splitting technologies for hydrogen production via: (i) electrode surface cleaning and activation, (ii) increased mass transfer in the bulk electrolyte and near the electrode surface, and (iii) efficient degassing at the electrode surface and electrolyte. They also showed that PUS can improve the electrolytic efficiency (up to 60%) caused by increased ion concentration and bubble removal at the electrode surface [27].

There are only a few reports in the literature dealing with the effects of PUS on the HER (and OER). For example, Banerjee *et al.* [28] found that the ultrasonication (25 kHz, 250 W) of aqueous mixtures consisting of Zn particles and $NiCl_2$ in HCl enhanced hydrogen evolution due to reduced mass transfer contribution yielding an ohmically controlled process. Walton *et al.* [29] showed that ultrasound (38 kHz) slightly affects the HER from 1 M H_2SO_4 at platinised platinum electrode due to improved removal of adherent product species on the electrode surface. McMurray *et al.* [30]demonstrated that the HER and OER are affected by ultrasound (20 kHz, 26 W/cm^2) on a titanium sonotrode (the vibrating ultrasonic horn acting as the working electrode) immersed in a neutral aqueous electrolyte (0.7 M Na_2SO_4 adjusted to pH7 using 0.1 M NaOH), and concluded that these observations were mainly due to enhanced mass transport as well as increased metallic corrosion rates induced by intense agitation and cavitation at the electrode surface. S.D. Li *et al.* [31] and J. Li *et al.* [32]investigated the effects of power ultrasound (25.3 kHz, 33.3 kHz, 60 kHz, <50 W) on a Pt electrode immersed in mild alkaline solutions (0.1 M, 0.5 M and 1.0 M NaOH). They found that ultrasound helped in removing the thin layer of bubbles at the electrode surface, especially at lower concentrations.

Lin and Hourng [33] showed by the aid of electrochemical impedance spectroscopy (EIS) that ultrasound (113 kHz, up to 900 W) improved the activity and concentration impedances and greatly improved the removal of hydrogen bubbles at the electrode surface and in the electrolyte. Since the bubble surface coverage (Θ) is proportional to the ohmic resistance (R) and overall cell overpotential [34] then PUS should, in theory, reduce V_{cell} [11].

However, in these studies, in-depth kinetic analyses were not undertaken in order to shed some lights on the effects of ultrasound on the HER mechanisms and Tafel parameters in mild acidic and alkaline electrolytes. The kinetics of the fundamental HER reactions (as well as the hydrogen oxidation reaction -HOR, oxygen reduction reaction ORR and oxygen evolution reaction - OER) are simply based upon "microkinetic analyses" and can be described by: (a) the dependence of the Tafel slope on the coverage of the formed surface species, e.g. M–H for the HER/HOR, M–OH, M–O, M–OOH and M–OO− for the ORR/OER, where M is the electrode surface site, and (b) the Butler-Volmer equation in explaining electrocatalytic kinetics [35].

Theoretically, simple electrochemical redox reactions can be described by the Butler-Volmer equation (BVE) shown in Equation 5.2 [35].

$$j = j_0 \left\{ \exp\left((1-\alpha)\frac{zF}{RT}\eta \right) - \exp\left[-\alpha \frac{zF}{RT}\eta \right] \right\} \quad (5.2)$$

where η is the overpotential, which is the difference between the electrode applied (E_{app}) and reversible potentials (E^{rev}) ($\eta = E_{app} - E^{rev}$), j is the current density (A/m^2), α is the transfer coefficient, z is the number of electrons transferred, F is the Faraday's constant (96,489 C/mol), R is the universal gas constant (8.314 J/mol/K), T is the absolute temperature (K), and j_o is the exchange current density (A/m^2). The equation represents the total currents from both the reduction and oxidation reactions. Experimentally, two limiting forms of the BVE are used to obtain the Tafel equations [35].

At large positive overpotentials, i.e. when $\eta \rightarrow +\infty$ i.e. $\exp\left[\left(\frac{-\alpha zF}{RT}\right)\eta\right] \rightarrow 0$, then the BVE can be approximated to:

$$j = j_0 \left\{ exp\left[\left((1-\alpha)\frac{zF}{RT} \right)\eta \right] \right\} \quad (5.3)$$

or

$$\log(j) = \log(j_0) + \frac{(1-\alpha)zF}{(2.303RT)}\eta \quad (5.4)$$

or

$$\eta = -2.303\ \frac{RT}{(1-\alpha)zF}\ \log(j_0) + 2.303\frac{RT}{(1-\alpha)zF}\log(j) \qquad (5.5)$$

At large negative overpotentials, i.e. $\eta \rightarrow -\infty$, the BVE can be approximated to:

$$j = -j_0\left\{exp\left[\left((-\alpha)\frac{zF}{RT}\right)\eta\right]\right\} \qquad (5.6)$$

or

$$\log(|j|) = \log(j_0) - \frac{\alpha zF}{(2.303RT)}\eta \qquad (5.7)$$

or

$$\eta = 2.303\ \frac{RT}{\alpha zF}\ \log(j_0) - 2.303\frac{RT}{\alpha zF}\log(|j|) \qquad (5.8)$$

The logarithmic relationships are known as Tafel equations in the form of:

$$\eta = a + b\log(j) \qquad (5.9)$$

where

$$a = -2.303\ \frac{RT}{(1-\alpha)zF}\ \log(j_0) \text{ for when } \eta \rightarrow +\infty \qquad (5.10)$$

or

$$a = +2.303\ \frac{RT}{\alpha zF}\ \log(j_0) \qquad \text{for when } \eta \rightarrow -\infty \qquad (5.11)$$

and

$$b = +2.303\ \frac{RT}{(1-\alpha)zF} \qquad \text{for when } \eta \rightarrow +\infty \qquad (5.12)$$

or

$$b = -2.303\ \frac{RT}{\alpha zF} \qquad \text{for when } \eta \rightarrow -\infty \qquad (5.13)$$

The Tafel slope (b) provides insight into the reaction mechanism, and the exchange current density (j_o) are known as descriptors of the catalytic activity. Thus, for analysing electrochemical performances, the Tafel analysis is conjugated with the Butler-Volmer equation in many studies.

In the case of the HER, there are two general possible pathways [4, 36]:

In acidic electrolyte:

$2H^+ + 2e^- \rightarrow H_2(g)$ $\qquad E^o = 0.000$ V vs. SHE $\qquad (5.14)$

In alkaline electrolyte:

$2H_2O(aq) + 2e^- \rightarrow H_2(g) + 2OH^-(aq)$ $E^o = -0.828$ V vs. SHE (5.15)

Under Standard Temperature and Pressure (*STP*) i.e. $T = 298.15$ K and $P_{H_2} = 1$ atm, the equilibrium or *Nernst* potential for the HER in acidic electrolyte is described by Equation (5.16):

$$E_{HER} = E^{\emptyset}_{H_2/H^+} + \frac{RT}{zF} \times \ln\left(\frac{P^{0.5}_{H_2}}{a_{H^+}}\right) = -0.059 \times pH \quad (5.16)$$

where E_{HER} is the *Nernst* potential (V vs. RHE), $E^{\emptyset}_{H_2/H^+}$ is the standard reduction potential for the redox couple H_2/H^+ (0.000 V vs. SHE), R is the ideal gas constant (8.3145 J/mol/k), T is the temperature (K), z is the number of electrons transferred, F is the Faraday number (96,489 C/mol), P_{H_2} is the hydrogen pressure (atm), and a_{H^+} is the activity of protons (mol/l).

There are three primary steps involved in the HER reaction in acidic media and each step has its character Tafel slope value [36]:

$H_3O^+ + e^- \rightarrow H_{ads} + H_2O$ Volmer reaction: $b = 120$ mV/dec (5.17)

$H_{ads} + H_3O^+ + e^- \rightarrow H_2 + H_2O$ Heyrovsky reaction: $b = 40$ mV/dec (5.18)

$H_{ads} + H_{ads} \rightarrow H_2$ (chemical) Tafel reaction: $b = 30$ mV/dec (5.19)

The first discharge step (Volmer reaction) is followed by either an electrochemical desorption step (Heyrovsky reaction) or a recombination step (Tafel reaction). The Tafel slope value is an inherent indicator of the electrocatalyst to show the rate-limiting step of HER.

In this study, we investigated the effects of power ultrasound on the HER on Pt polycrystalline electrode in 0.5 M H_2SO_4 by cyclic and linear sweep voltammetry at 298 K. We also studied the formation of molecular hydrogen bubble in the absence and presence of power ultrasound using ultra-fast camera imaging.

5.2 Experimental Methods

All electrochemical experiments were carried out using a potentiostat/galvanostat (BioLogic SP-150) in a 3-electrode configuration. In this study, two sonoelectrochemical cells were used as shown in Figure 5.1(a) and Figure 5.1(b).

All voltammetry work was performed using a specially designed sono-reactor placed in an *in-house* Faraday cage (Fig 5.1(a)). This sono-reactor also called the *Besançon cell* has been

fully characterized and well-described elsewhere [20, 21, 37, 38]. The working electrode (WE) was either a polycrystalline platinum (Pt-poly) disc (∅ = 0.182 cm) of geometric surface area (A_g) of 0.027 ± 0.002 cm^2 or a Pt-poly wire (L = 8 cm, ∅ = 0.1 cm). The reference electrode (RE) was a home-made standard hydrogen electrode (RHE). The counter electrode (CE) was a Pt wire (∅ = 0.5 mm, 99.95%, Alfa Aesar) sealed in a glass tube. The distance between the ultrasonic probe and the working electrode was ca. 3 cm. All working electrodes were electrochemically cleaned in sulfuric acid (1.0 mol/L) for 10 min prior to the experiments. They were then washed with ultrapure water (Millipore, 18.2 MΩ.cm). All 0.5 mol/L H_2SO_4 working electrolytes (pH = 0.3) were made from pure H_2SO_4 purchased from Merck (purity 96%). The temperature of the electrolyte was measured with a Fluke 51 digital thermometer fitted to a *K*-type thermocouple.

For all cyclic voltammetry (CV) and linear sweep voltammetry (LSV) experiments, the acquired potential values were modified by *IR* compensation correction based on the following Equation:

$$E_{\text{IR-corrected}} = E - IR \tag{5.20}$$

where I is the measured current density and R the resistance of electrolyte, which was measured in 0.5 mol/L H_2SO_4 solution. The R value was determined by electrochemical impedance spectroscopy (EIS) from the value of the *real* impedance (Z) where the *imaginary* impedance (Z') is zero in Nyquist plot. The EIS experiments (not shown here) were carried out from 100 kHz to 0.01 Hz with a voltage perturbation of +10 mV at an applied potential of -0.05 V vs. RHE and at T = 298 K [39].

The exchange current density (j_o) was obtained by the extrapolation method from the corresponding Tafel plot. According to Tafel equation: $\eta = a + b\log(j)$ (a and b are calculated from Tafel plot, see earlier), j_o can be obtained by extrapolating the Tafel plots to the x-axis or assuming η is zero [39, 40].

The onset potentials (E_{onset}) and overpotential (η) at a current density (j) of -10 mA/cm^2 were obtained from HER LSVs. Here, the onset potential is the applied potential with apparent cathodic currents. However, it should be emphasized that it is not a straight-forward method to determine a "precise" value. Usually, the onset overpotential is calculated at a current density of -1 mA/cm^2 [39, 41]. The (over)potential value for the current density of -10 mA/cm^2 (i.e. the current density expected for a 12.3% efficient solar water-splitting device) is also regarded as another critical factor to assess HER activity [41, 42]. In this study, we present both potential values i.e. E_{onset} and potential ($E_{\text{-10mA/cm}^2}$) at a current density of -10 mA/cm^2.

For all sonoelectrochemical experiments, ultrasound was provided by a 26 kHz (f) ultrasonic probe (Hielscher UP200Ht, 200 W @ 100% fixed amplitude, tip $\varnothing$ = 7 mm, tip area = 38.48 mm^2 (3.85 x 10^{-3} cm^2). The ultrasonic or acoustic powers were determined calorimetrically using the methods of Margulis *et al.* [43] and Contamine *et al*. [44] and using Equation 5.21:

$$P_{acous} = (dT/dt)_{t=0} \times m \times C_p \qquad (5.21)$$

where $(dT/dt)_{t=0}$ is the temperature slope per unit of ultrasonication time (at t = 0) in K/s; m is the mass of the water used in g and C_p is the specific heat capacity of water as 4.186 J/g/K. Here, the calorimetric method consists in measuring the heat dissipated in a known mass or volume of water, considering the water heat capacity (C_p) in which the acoustic energy is absorbed. This method assumes that all absorbed acoustic energy is transformed into heat. From the calorimetric experiments, the acoustic power, P_{acous} in W was determined. In our conditions, the acoustic power (P_{acous}) was found to be 4.65 W, 12.10 W, 18.30 W, 25.0 W and 29.20 W at 20%, 40%, 60%, 80% and 100% ultrasonic amplitude respectively.

All high-speed imaging water electrolysis experiments were performed in an *in-house* made perspex sonoelectrochemical cell – 50 mm x 50 mm x 150 mm with the ultrasonic horn inserted through the base and sealed with a silicon ring (Fig. 5.1(b)) using the sonoelectrochemical setup described in Figure 5.2. A platinum (Pt) wire was used as the working electrode (WE) placed horizontally in the sonoelectrochemical cell with the electrical connections made external to the cell. The reference (RHE, RE) and counter electrodes (Pt wire, CE) were inserted into the corners of the sonoelectrochemical cell in a vertical orientation. High speed images were captured using a Photron SA 5 camera, at a frame rate of 10,000 frames per second (fps) using diffused back-lit illumination. The light source was a high-power single chip LED (CBT 120) with light collimated onto an engineered diffusor (ThorlabsED1-C50) placed behind the sonoelectrochemical cell. A short exposure time of 1 ms was applied at a resolution of 896 x 848. The camera was fitted with a Nikon 60 micro lens and the resulting region that could be imaged was approx. 25 mm^2 and a record length of 2 seconds (see Figs. 5.1(b) and 5.2(b)). Prior to image collection, the ultrasonic probe was used to efficiently degas the solution to reduce imaging gas bubbles that were not associated with water electrolysis.

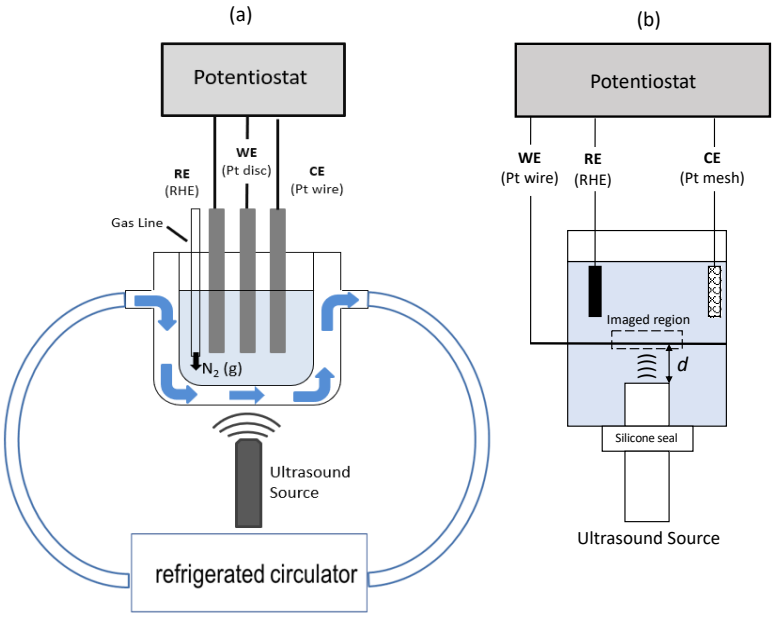

Figure 5.1. (a) Sonoelectrochemical cell used for the voltammetry study; (b) Sonoelectrochemical cell used for high-speed imaging.

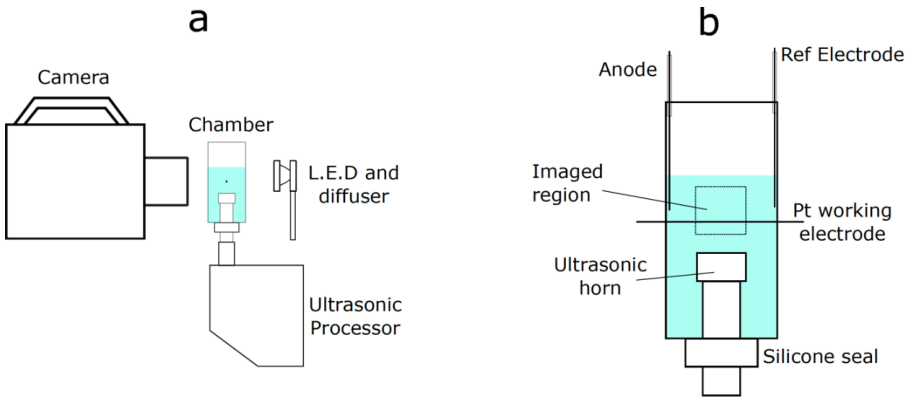

Figure 5.2. Sonoelectrochemical setup for high-speed imaging. (a) Camera set-up: Camera Photron SA5 with a Nikon 60mm Macro f2.8 lens. Maximum aperture used. Frame rate of 10,000 fps, 898 x 848 resolution, 33.26 µs exposure time, illuminated by a fibre optic illuminator (Cole Parmer Mod 41500-55). The light source was a high power single chip LED (CBT120) with light collimated onto an engineered diffusor (ThorlabsED1-C50) placed behind the sonoelectrochemical (SE) cell. (b) SE cell set up.

5.3 Results and Discussion

5.3.1 Study of the Underpotentially Deposited Hydrogen (UDH) in the absence and presence of ultrasound

Silent conditions

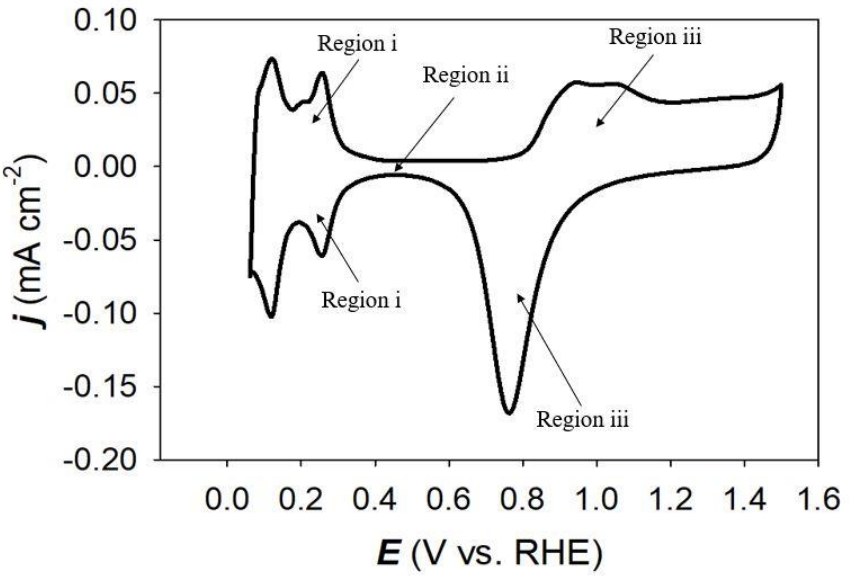

Figure 5.3. A typical cyclic voltammogram of 0.5 M H_2SO_4 on a polycrystalline Pt disc electrode at a scan rate of 50 mV/s and at T = 298 K after purging with N_2(g) for 30 minutes.

Figure 5.3 shows a cyclic voltammogram (CV) of a polycrystalline Pt disc electrode in 0.5 M H_2SO_4 at a scan rate of 50 mV/s and at 298 K after purging with N_2(g) for 30 minutes. The CV profile exhibits the typical electrochemical features of a pure Pt-poly surface in which three regions ([i], [ii] and [iii]) can be clearly distinguished, namely:

(i) Regions [i] - The underpotentially deposited hydrogen (UPD-*H*) region (+0.05 – +0.45 V vs. RHE) where adsorption (H_{upd}, negative current densities) and desorption peaks (H_{upd}, positive current densities) for UPD-*H* are observed between +0.05 and +0.40 V vs. RHE. The two pairs of redox peaks are usually attributed to strongly and weakly adsorbed *H* atoms at the Pt surface, respectively.

(ii) Region [ii] - The capacitive double-layer region (+0.45 – +0.60 V vs. RHE), in the centre of the CV, only represents capacitive processes [45].

(iii) Regions [iii] - The formation and reduction of Pt (hydr)oxide above +0.60 V vs. RHE. This pair of redox peaks appears during the positive and negative scans, which is normally attributed to the formation (positive current densities) and reduction (negative current densities) of Pt hydroxide/oxide ($PtOH/PtO_x$) at the Pt electrode surface [45, 46].

From the CV, the "real" surface area (A_r) of the Pt-poly electrode can be calculated by determining, after correction from the capacitive current density, the coulombic charge associated to the H_{upd} desorption in the +0.05 to +0.45 V vs. RHE potential region, according to Equation 5.22:

$$A_r = \frac{\frac{1}{v}\int i(E)\mathrm{d}E}{Q_{monolayer}} \quad (5.22)$$

where $i(E)$ is the current (μA) recorded at potential E (V vs. RHE) in the hydrogen desorption region, v is the linear potential variation or potential scan rate (V/s) and $Q_{monolayer}$ (μC/cm^2) is the coulombic charge related to the adsorption or desorption of a hydrogen monolayer on a polycrystalline Pt surface ($Q_{monolayer}$ = 210 μC/cm^2) [45, 46]. A value of 0.037 ± 0.001 cm^2 for the A_r was obtained against 0.027 ± 0.002 cm^2 for the geometric surface area (A_g), e.g. a roughness factor (A_r/A_g) ≈ 1.38.

Ultrasonic conditions

Figure 5.4 shows a series of cyclic voltammograms (CVs) of 0.5 mol/L H_2SO_4 on a polycrystalline Pt disc electrode at a scan rate of 50 mV/s and at 298 K after the Pt disc electrode was subjected to continuous ultrasonic irradiation (26 kHz) at various ultrasonic amplitudes (20%, 40%, 60%, 80% and 100%) for 6 minutes during the linear sweep voltammetry (LSV) experiments (see Fig 5.5). For clarification, all CVs were performed just after each LSV experiment i.e. the Pt disc electrode was kept in the electrolyte that was subjected to sonication. Table 5.1 shows the coulombic charges associated to (i) the H_{upd} adsorption (Q_{ads}), (ii) the H_{upd} desorption (Q_{des}), (iii) the formed PtO (Q_{PtO}), (iv) the PtO reduction (Q'_{PtO}), as well as the double layer capacitance (C_{dl}), the "real" Pt electrode surface area (A_r) and the roughness factor (R) under *silent* and after ultrasonic conditions (26 kHz) at various ultrasonic powers and at 298 K, determined and calculated from Figure 5.4 and Equation 5.22.

Figure 5.4 and Table 5.1 clearly show that ultrasound does not have a significant effect on the shape of the CVs and the charges associated with Pt surface reaction in 0.5 mol/L H_2SO_4. These observations are in good agreement with those found by Walton *et al.* [29], although in

their conditions, the CVs from 1 M H_2SO_4 at platinised platinum electrode were generated under continuous sonication (38 kHz, ultrasonic bath).

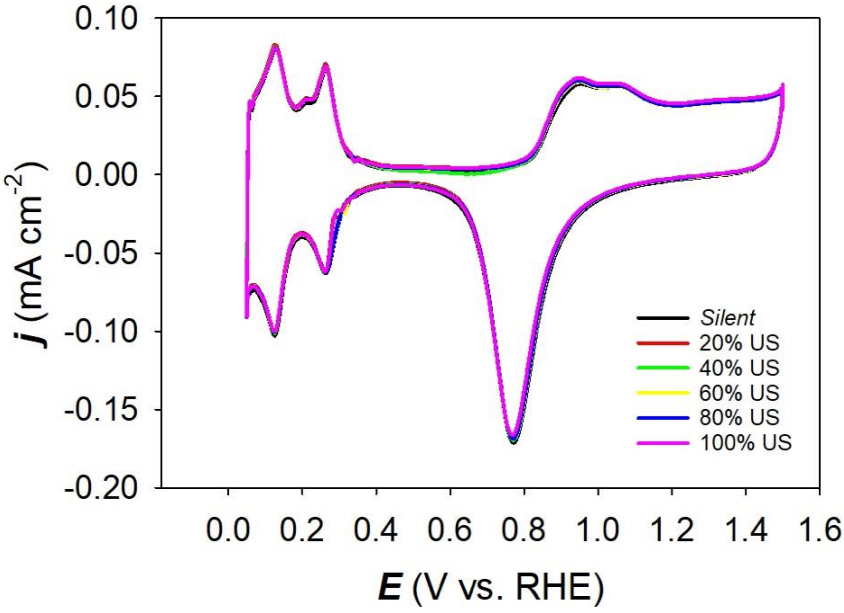

Figure 5.4. A series of cyclic voltammograms (CVs) of polycrystalline Pt disc electrode in 0.5 M H_2SO_4 at a scan rate of 50 mV/s and at T = 298 K after the Pt disc electrode was subjected to ultrasonic irradiation (26 kHz) at various ultrasonic amplitudes (20%, 40%, 60%, 80% and 100%) for 6 minutes.

Table 5.1. Coulombic charge associated to the H_{upd} adsorption (Q_{ads}), coulombic charge associated to the H_{upd} desorption (Q_{des}), coulombic charge associated to the formed PtO (Q_{PtO}), coulombic charge associated to the PtO reduction (Q'_{PtO}), double layer capacitance (C_{dl}), "real" Pt electrode surface area (A_r) and roughness factor (R) under *silent* and after ultrasonic conditions (26 kHz) at various ultrasonic powers and at 298 K.

Ultrasonic power, P_{acous} W (ultrasonic amplitude %)	**Q_{ads} μC/cm²**	**Q_{des} μC/cm²**	**Q_{PtO} μC/cm²**	**Q'_{PtO} μC/cm²**	**C_{dl} μF/cm²**	**A_r * cm²**	**R**
0 (*Silent*)	286.31	294.88	328.95	485.674	219.69	0.0374	1.38
4.65 (20)	273.51	284.88	322.28	456.26	226.32	0.0358	1.33
12.10 (40)	279.48	296.72	330.37	454.78	192.8	0.0370	1.37
18.30 (60)	285.86	284.11	326.04	482.66	227.42	0.0366	1.36
25.00 (80)	269.87	260.11	323.69	472.99	232.29	0.0340	1.26
29.20 (100)	278.61	279.99	328.40	463.20	249.98	0.0359	1.33

*Calculated from Equation 5.22 and using $Q_{monolayer}$ = 210 μC/cm².

Table 5.1 shows that as the ultrasonic amplitude increases from 0 to 100%, Q_{ads}, Q_{des}, Q_{PtO}, and Q'_{PtO} slightly decrease. The decrease in these charges could be due to changes in electrode surface morphology due to the collapse of cavitation bubbles which could influence the adsorbate coverage on the electrode surface as previously observed by Walton et *al.* [29].

For example, it can be observed that Q_{des} decreased from 294.88 μC/cm^2 to 279.99 μC/cm^2 as the ultrasonic amplitude was increased from 0 to 100% acoustic amplitude. However, the C_{dl} shows an adverse trend where C_{dl} increased from 219.69 μF/cm^2 to 249.98 μF/cm^2 as the acoutic amplitude increased from 0 to 100%. Similar observations were found by Zhang and Coury [47] who attributed this increase to an increased surface functionalisation (*pseudo-capacitance*) and slight changes in electrode surface area.

In our conditions, A_r and R i.e. the microscopic area available for electron transfer was not evidently affected by ultrasound for all acoustic powers used, indicating that the electrochemical surface area was not greatly modified due to erosion caused by the implosion of acoustic cavitation bubble on the electrode surface. For example, at maximum ultrasonic power, only a <5% decrease in A_r and R was observed when compared to *silent* conditions (Table 5.1). These findings are in very good agreement with those observed by Zhang and Coury [47] as well as Pollet [48] who showed that the electrode surface area and roughness factor was little affected by ultrasound. In some instances, they found that a slight increase in electrode surface area was observed after prolonged sonication (5 min, 20 kHz, 475 W) due to electrode activation, through possible removal of adsorbed species on the electrode surface i.e., surface cleaning. Overall, no significant enhancements under sonication were observed.

5.3.2 Study of the effect of ultrasonic power on the Hydrogen Evolution Reaction

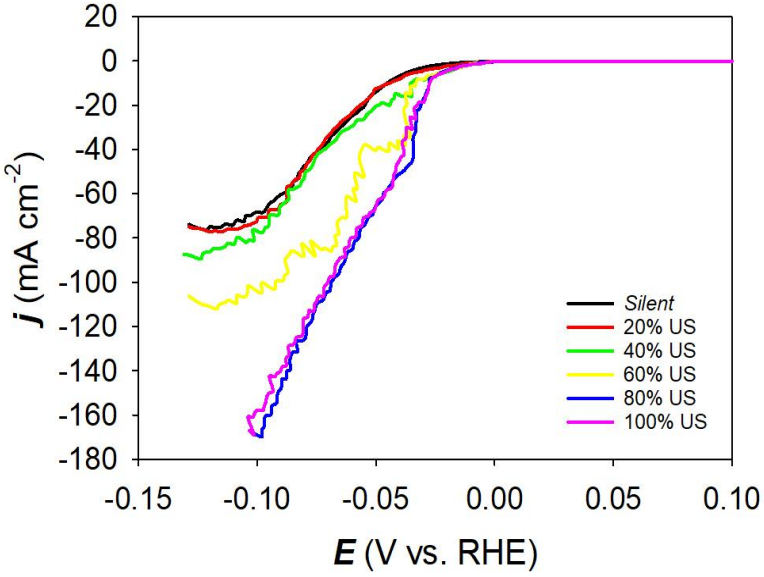

Figure 5.5. Linear sweep voltammograms (LSVs) on 0.5 mol/L H_2SO_4 on a polycrystalline Pt disc electrode at a scan rate of 1 mV/s and at T = 298 K after purging with N_2(g) for 30 minutes under (a) *silent* and (b) ultrasonic conditions (26 kHz, ultrasonic amplitude: 20%, 40%, 60%, 80% and 100%).

Figure 5.5 shows a series of LSVs on a Pt disc in 0.5 mol/L H_2SO_4 under *silent* and ultrasonic conditions up to 100% amplitude. To quantitatively compare the performance of an "ideal" HER (and OER) electrocatalyst, it should exhibit lower onset potentials and deliver higher current densities with lower overpotentials. From Table 5.2, it can be observed that the onset potentials gradually decreased from -17.6 mV vs. RHE under *silent* conditions to -5.7 mV vs. RHE at maximum ultrasonic power as the ultrasonic amplitude increased to 100% i.e. a ΔE shift of ~+10 mV was achieved. It can also be noted that the potential at -10 mA/cm^2 under *silent* conditions was found to be -46 mV and decreased to -27 mV at 100% i.e. a ΔE shift of ~+20 mV, indicating the influence of ultrasound on improving HER activity. The slopes of the LSV branches in the range [-0.05 V vs. RHE - -0.10 V vs. RHE] increased from 1.15 mA/cm^2/mV (*silent* conditions) to 1.93 mA/cm^2/mV (100% ultrasound), in other words, steeper LSV branches were obtained under sonication. Moreover, the current density at an

electrode potential of -0.10 V vs. RHE increased as ultrasound amplitude increased from 0% (~70 mA/cm^2) to 100% (~170 mA/cm^2) i.e. a ~250% increase in current density was achieved at maximum ultrasonic power. It is worth noting that the LSVs at 0, 20, 40, and 60% ultrasonic amplitude exhibited “plateaux” at high current densities due to hydrogen bubble accumulation on the electrode surface while LSVs at 80 % and 100 % ultrasound showed straight LSV branches in the same high current density region, confirming bubble removal under intense agitation (see later). All sono-LSVs also exhibited, at high current densities, current spikes in the range of [-0.07 V vs. RHE - -0.14 V vs. RHE], due to both hydrogen bubble accumulation and cavitation bubbles imploding at the electrode surface. Birkin *et al.* [49] and recently Islam *et al.* [37] showed that the current spikes were mainly attributed to the implosion of cavitation bubbles at the electrode surface. Overall, the electrochemical conditions under 100% ultrasound amplitude led to improved and superior HER activity.

Table 5.2 . Slopes of the LSV branches in the range [-0.05 - -0.10 V vs. RHE], onset potentials (E_{onset}), potentials at -10 mA/cm^2 (E_{-10mA/cm^2}), exchange current densities (j_o) and Tafel slopes (b) at low and high overpotentials under *silent* and ultrasonic conditions (26 kHz) at various ultrasonic powers (20%, 40%, 60%, 80% and 100%).

Ultrasonic power, P_{acous} W [US amplitude %]	Slopes of the LSV branches mA/cm^2/mV	Onset potentials, E_{onset} mV vs. RHE	Potential at -10 mA/cm^2 E_{-10mA/cm^2} mV vs. RHE	Tafel slope, b at low overpotentials mV/dec	Tafel slope, b at high overpotentials mV/dec	Exchange current density, j_o mA/cm^2
0 (*silent*)	1.15	-17.6	-46	30±2	123±3	0.27±0.07
4.65 [20]	1.28	-11.6	-44	32±2	123±3	0.39±0.07
12.10 [40]	1.20	-7.9	-34	25±4	121±4	0.43±0.11
18.30 [60]	1.27	-7.8	-33	23±5	141±3	0.47±0.05
25.00 [80]	2.11	-7.6	-27	18±6	113±6	0.36±0.03
29.20 [100]	1.93	-5.7	-27	21±4	124±2	0.50±0.19

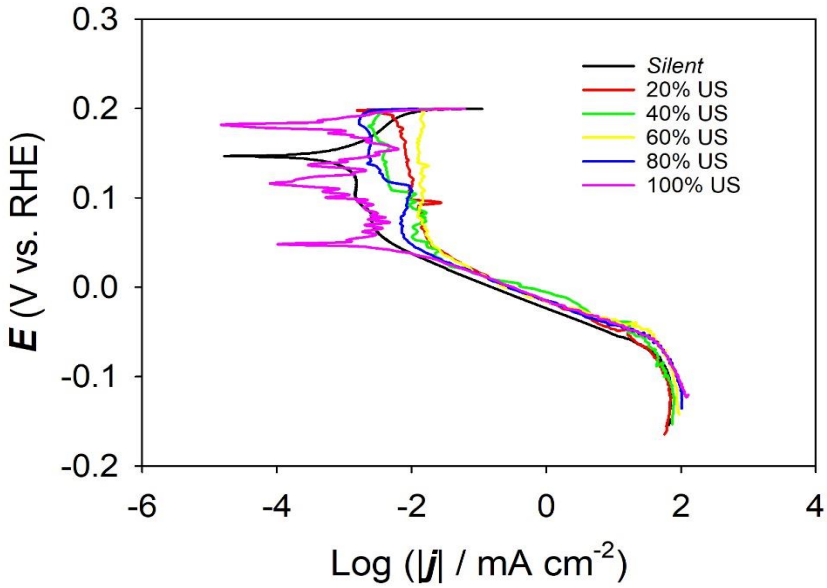

Figure 5.6. A series of Tafel plots for the HER occurring at a polycrystalline Pt disc electrode in 0.5 mol/L H_2SO_4 subjected to ultrasound at (a) 0 (*silent*) and (b) 20, 40, 60, 80 and 100 % power from LSVs carried out at a scan rate 1 mV/s and at T = 298 K after purging with N_2(g) for 30 minutes.

Figure 5.6 shows the Tafel plots of Pt-poly disc under *silent* and ultrasonic conditions. Table 5.2 shows that the Pt disc exhibited fairly similar Tafel slopes under these conditions at low and high overpotential regions. At the low overpotential region, the Pt disc displays Tafel slopes of b ~20-30 mV/dec suggesting that the Tafel recombination reaction is the rate-determining step, following the fast initial Volmer discharge step. However, it is worth noting that the Tafel slope value at maximum ultrasonic power (b = 21 mV/dec) was much lower than that under *silent* conditions (b = 30 mV/dec) i.e. a ~30% decrease. As the overpotential is increased i.e. in the high overpotential region, the sonicated and non-sonicated Pt disc shows Tafel slopes of b ~120 mV/dec i.e. the coverage of absorbed hydrogen approaches saturation. This leads to an accelerated Tafel recombination step and the Volmer discharge step becomes the rate-determining step [35, 47].

j_o is a key parameter to evaluate HER catalytic activity. Table 5.2 also shows that the j_o values for Pt disc under *silent* and ultrasonic conditions increased from +0.27 to +0.50 mA/cm^2 as the ultrasonic amplitude increased from 0 to 100 %, in other words, a nearly 100% increase in j_o was observed under maximum ultrasonic conditions. As the j_o value is proportional to the electrochemical active surface area (ECSA) or A_r, this finding indicates high electrode catalytic activity, and thus rapid electron transfer and improved HER kinetics. However, contrarily to our previous observations, it was found that the A_r was not afftected by the pre-sonicated Pt electrodes, suggesting that other processes might had occurred on the sonicated electrode surface during the sono-LSV experiments. Nonetheless, for a high-performance electrocatalytic process, a low b and a high j_o is required [35] and from this investigation, the best electrochemical conditions were found at 100% ultrasonic amplitude.

5.3.3 Study of the hydrogen bubbles in the absence and presence of ultrasound

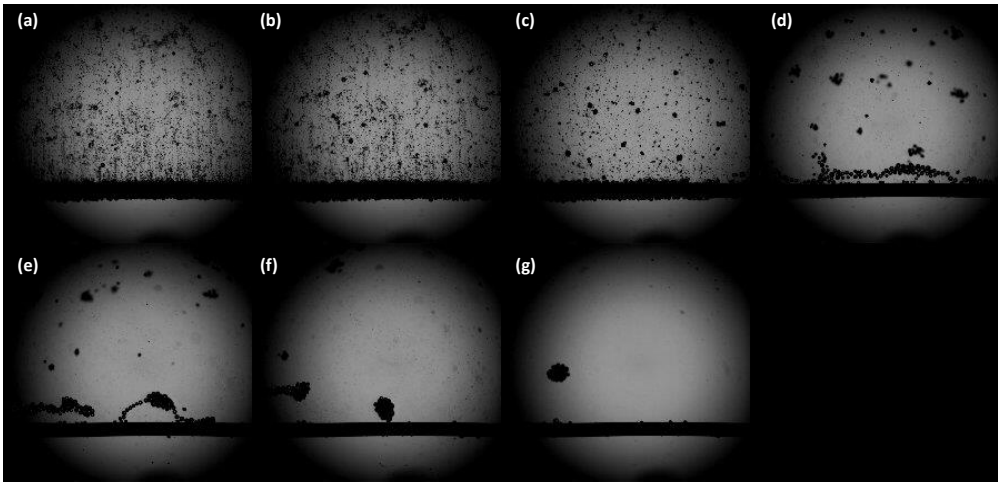

Figure 5.7. Hydrogen evolution on a Pt wire in the absence (top left corner) and presence of ultrasound (26 kHz, 100% ultrasonic amplitude). The applied potential was set at -1.30 V vs. RHE – (a) 0 μs, (b) 100 μs , (c) 200 μs, (d) 300 μs, (e) 400 μs, (f) 500 μs, (g) 600 μs. The time between each image is 10^{-4} s (100 μs) filmed at 10,000 frames per second. For the complete video see *Supplementary Information*.

Figure 5.7 shows a series of images for the hydrogen evolution on a Pt wire in the absence (Fig.5.7(a)) and presence of ultrasound (26 kHz, 100% ultrasonic amplitude - (Figs. 5.7(b)-(g)) by high-speed imaging. The time between each image was 100 μs. The applied

potential was set at -1.30 V vs. RHE with a current of +80 mA i.e. a current density of +31.62 mA/cm^2 (316.20 A/m^2). From the figure, it may be observed that under *silent* conditions (Fig.5.7(a)), the hydrogen bubbles are very small and similar in size, leaving the Pt wire electrode at a uniform velocity. Some larger hydrogen bubbles were observed which rose faster due probably to buoyancy and drag differences. Under ultrasonic conditions (Figs. 5.7(b)-(g)), it was found that the hydrogen bubbles formed above the Pt wire electrode agglomerated to form larger hydrogen bubbles possibly due to secondary Bjerknes forces [50] in turn removing small bubbles from the Pt wire surface. Moreover, and interestingly, it was observed that large hydrogen bubbles had uniform sizes and formed well-organised "chains" before forming larger hydrogen bubble clusters. After 0.5 s of continuous sonication, the Pt wire electrode was “cleaned” and a few or even no hydrogen bubbles above the Pt wire electrode were visible as they coalesced with larger ones running along the wire. It was previously found that the collection of pre-existing gas bubbles under sonication are due to 2nd Bjerknes effect which is an expected common effect. Small bubbles easily coalesce to macro-bubbles of larger sizes [31-33, 50, 51].

From the video (filmed at 10,000 frames per second – see file entitled “USMaxPower(100%).gif [Video Still]”), it can be observed that the hydrogen bubbles seem to migrate to nodes in the electrolyte via the so-called “primary radiation force” [31-33, 50]. This effect is known to be due to the difference in the density and compressibility between the gas bubbles as well as the electrolyte phase leading to an “acoustophoretic effect” in which the dispersed bubble migrates to these nodes. When the hydrogen bubble reaches the nodal areas, the secondary Bjerknes force acts between the bubbles to promote coalition [50]. The resulting increase in the size of the bubbles increases their buoyancy augmenting electrolyte hydrogen degassing. It has been previously shown that these processes take place sequentially and simultaneously under sonication [31-33, 50]. In our conditions, during the first few microseconds of ultrasonication, the hydrogen bubbles migrate towards the closest pressure nodes, and as they meet nearby bubbles, they hit, coalesce, and rise faster to the surface. In other words, under sonication, the hydrogen bubbles detach from the electrode surface when they move from the nucleation site parallel to the electrode surface, they either coalesce with adhering bubbles or collide and are pushed away from the electrode surface.

5.4 Conclusions

We studied the effects of power ultrasound (26 kHz, up to ~75 W/cm^2) on a platinum (Pt) polycrystalline disc electrode immersed in a 0.5 M H_2SO_4 solution by cyclic and linear sweep voltammetry at 298 K. We observed that, in our experimental conditions, a ~250% increase in current density towards the hydrogen evolution reaction (HER) was achieved at maximum ultrasonic power (100%), although no obvious changes in the "real" surface area (A_r) and roughness factor (R) were observed. It was found that the HER started earlier under sonication at maximum acoustic power i.e. a ΔE shift of ~+20 mV was observed, suggesting that ultrasound improves the HER activity on Pt. A nearly 100% increase in the exchange current density (j_o) at 100% ultrasonic amplitude was observed, although the Tafel slopes (b) at high overpotentials were not greatly affected when compared to *silent* conditions. Overall, it was found that ultrasound did not significantly modify the mechanism of HER but instead increased currents at the Pt disc surface area through effective hydrogen bubble removal as indicated by the ultra-fast camera imaging experiments. From this study, it can be postulated that the main contribution of ultrasound is the efficient gas bubble removal from the electrode surface and from the bulk electrolyte in turn reducing the bubble surface coverage and the void fraction of the bulk electrolyte, respectively.

Acknowledgements

The authors would like to thank Prof. Dr. Robert Mettin (Drittes Physikalisches Institut – Biophysik, Georg-August-Universität Göttingen, Germany), Prof. Gregory Jerkiewicz (Queen's University, Chemistry Department, Kingston, Canada) and Prof. Christophe Coutanceau (IC2MP, MediaCat, Université de Poitiers, France) for useful discussions.

References

[1]https://publications.jrc.ec.europa.eu/repository/bitstream/JRC115958/kjna29695enn.pdf. Visited on 23 April 2020].

[2] Nazir, H., et al., *Is the H2 economy realizable in the foreseeable future? Part I: H2 production methods.* International Journal of Hydrogen Energy, 2020.

[3] Lamy, C., C. Coutanceau, and S. Baranton, *Production of Clean Hydrogen by Electrochemical Reforming of Oxygenated Organic Compounds*. 2019: Academic Press.

[4] Coutanceau, C., S. Baranton, and T. Audichon, *Hydrogen electrochemical production*. 2017: Academic Press.

[5] Kumar, S.S. and V. Himabindu, *Hydrogen production by PEM water electrolysis–A review.* Materials Science for Energy Technologies, 2019. **2**(3): p. 442-454.

[6] Carmo, M., et al., *A comprehensive review on PEM water electrolysis.* International journal of hydrogen energy, 2013. **38**(12): p. 4901-4934.

[7] Zeng, K. and D. Zhang, *Recent progress in alkaline water electrolysis for hydrogen production and applications.* Progress in energy and combustion science, 2010. **36**(3): p. 307-326.

[8] Grigoriev, S., et al., *Current status, research trends, and challenges in water electrolysis science and technology.* International Journal of Hydrogen Energy, 2020. **45**(49): p. 26036-26058.

[9] Theerthagiri, J., et al., *Highly electroactive Ni pyrophosphate/Pt catalyst toward hydrogen evolution reaction.* ACS applied materials & interfaces, 2019. **11**(5): p. 4969-4982.

[10] Bessarabov, D. and P. Millet, *PEM Water Electrolysis*, in *Hydrogen and Fuel Cells Primers Series*, B. Pollet, Editor. 2018, Academic Press: Cambidge.

[11] Wang, M., et al., *The intensification technologies to water electrolysis for hydrogen production–A review.* Renewable and Sustainable Energy Reviews, 2014. **29**: p. 573-588.

[12] Angulo, A., et al., *Influence of bubbles on the energy conversion efficiency of electrochemical reactors.* Joule, 2020. **4**(3): p. 555-579.

[13] Mazza, B., P. Pedeferri, and G. Re, *Hydrodynamic instabilities in electrolytic gas evolution.* Electrochimica Acta, 1978. **23**(2): p. 87-93.

[14] Vogt, H., *The incremental ohmic resistance caused by bubbles adhering to an electrode.* Journal of Applied Electrochemistry, 1983. **13**(1): p. 87-88.

[15] Eigeldinger, J. and H. Vogt, *The bubble coverage of gas-evolving electrodes in a flowing electrolyte.* Electrochimica Acta, 2000. **45**(27): p. 4449-4456.

[16] Vogt, H. and R. Balzer, *The bubble coverage of gas-evolving electrodes in stagnant electrolytes.* Electrochimica acta, 2005. **50**(10): p. 2073-2079.

[17] Janssen, L., et al., *Bubble behaviour during oxygen and hydrogen evolution at transparent electrodes in KOH solution.* Electrochimica acta, 1984. **29**(5): p. 633-642.

[18] Pollet, B., et al., *Transport limited currents close to an ultrasonic horn: equivalent flow velocity determination.* Journal of the Electrochemical Society, 2007. **154**(10): p. E131.

[19] Pollet, B.G. and M. Ashokkumar, *Short introduction to sonoelectrochemistry*, in *Introduction to Ultrasound, Sonochemistry and Sonoelectrochemistry*. 2019, Springer. p. 21-39.

[20] Pollet, B., *Power Ultrasound in Electrochemistry: From Versatile Laboratory Tool to Engineering Solution*. 2012: John Wiley & Sons.

[21] Pollet, B.G. and M. Ashokkumar, *Introduction to Ultrasound, Sonochemistry and Sonoelectrochemistry*. 2019: Springer Nature.

[22] Theerthagiri, J., et al., *Sonoelectrochemistry for energy and environmental applications.* Ultrasonics Sonochemistry, 2020. **63**: p. 104960.

[23] Madhavan, J., et al., *Hybrid advanced oxidation processes involving ultrasound: an overview.* Molecules, 2019. **24**(18): p. 3341.

[24] Lepesant, M., *Sonoelectrochemical Production of Hydrogen for PEM Fuel Cell Applications*. 2011.

[25] Symes, D., *Sonoelectrochemical (20 kHz) production of hydrogen from aqueous solutions*. 2011, University of Birmingham.

[26] Zadeh, S.H., *Hydrogen production via ultrasound-aided alkaline water electrolysis.* Journal of Automation and Control Engineering Vol, 2014. **2**(1).

[27] Islam, M.H., O.S. Burheim, and B.G. Pollet, *Sonochemical and sonoelectrochemical production of hydrogen.* Ultrasonics sonochemistry, 2019. **51**: p. 533-555.

[28] Banerjee, S., R. Kumar, and K. Gandhi, *Analysis of ultrasonically enhanced hydrogen evolution for Zn-NiCl2 system.* Chemical engineering science, 1995. **50**(15): p. 2409-2418.

[29] Walton, D., L. Burke, and M. Murphy, *Sonoelectrochemistry: chlorine, hydrogen and oxygen evolution at platinised platinum.* Electrochimica acta, 1996. **41**(17): p. 2747-2751.

[30] McMurray, H., *Hydrogen evolution and oxygen reduction at a titanium sonotrode.* Chemical Communications, 1998(8): p. 887-888.

[31] Li, S.-D., C.-C. Wang, and C.-Y. Chen, *Water electrolysis in the presence of an ultrasonic field.* Electrochimica Acta, 2009. **54**(15): p. 3877-3883.

[32] Li, J., et al. *Ultrasound-Assisted Electrolysis in NaOH Solution for Hydrogen Generation*. in *EPD Congress 2011*. 2011. Wiley Online Library.

[33] Lin, M.-Y. and L.-W. Hourng, *Ultrasonic wave field effects on hydrogen production by water electrolysis.* Journal of the Chinese Institute of Engineers, 2014. **37**(8): p. 1080-1089.

[34] Qian, K., Z. Chen, and J. Chen, *Bubble coverage and bubble resistance using cells with horizontal electrode.* Journal of Applied Electrochemistry, 1998. **28**(10): p. 1141-1145.

[35] Shinagawa, T., A.T. Garcia-Esparza, and K. Takanabe, *Insight on Tafel slopes from a microkinetic analysis of aqueous electrocatalysis for energy conversion.* Scientific reports, 2015. **5**(1): p. 1-21.

[36] Theerthagiri, J., et al., *Fundamental aspects and recent advances in transition metal nitrides as electrocatalysts for hydrogen evolution reaction: A review.* Current Opinion in Solid State and Materials Science, 2020. **24**(1): p. 100805.

[37] Islam, M.H., et al., *The use of non-cavitating coupling fluids for intensifying sonoelectrochemical processes.* Ultrasonics Sonochemistry, 2020. **66**: p. 105087.

[38] Pollet, B.G., *Power ultrasound in electrochemistry.* Wiley Online Library, 2012.

[39] Wei, C., et al., *Recommended practices and benchmark activity for hydrogen and oxygen electrocatalysis in water splitting and fuel cells.* Advanced Materials, 2019. **31**(31): p. 1806296.

[40] Li, G. and W. Zhou, *Carbon-based Electrocatalysts for Water-splitting.* Flexible Energy Conversion and Storage Devices, 2018.

[41] Chen, Z., et al., *Recent advances in transition metal-based electrocatalysts for alkaline hydrogen evolution.* Journal of Materials Chemistry A, 2019. **7**(25): p. 14971-15005.

[42] Wu, Z.P., et al., *Non-noble-metal-based electrocatalysts toward the oxygen evolution reaction.* Advanced Functional Materials, 2020. **30**(15): p. 1910274.

[43] Margulis, M. and I. Margulis, *Calorimetric method for measurement of acoustic power absorbed in a volume of a liquid.* Ultrasonics Sonochemistry, 2003. **10**(6): p. 343-345.

[44] Contamine, R.F., et al., *Power measurement in sonochemistry.* Ultrasonics Sonochemistry, 1995. **2**(1): p. S43-S47.

[45] Daubinger, P., et al., *Electrochemical characteristics of nanostructured platinum electrodes–a cyclic voltammetry study.* Physical Chemistry Chemical Physics, 2014. **16**(18): p. 8392-8399.

[46] Zeng, M. and Y. Li, *Recent advances in heterogeneous electrocatalysts for the hydrogen evolution reaction.* Journal of Materials Chemistry A, 2015. **3**(29): p. 14942-14962.

[47] Zhang, H. and L.A. Coury, *Effects of high-intensity ultrasound on glassy carbon electrodes.* Analytical Chemistry, 1993. **65**(11): p. 1552-1558.

[48] Pollet, B., *The Effect of Ultrasound on Electrochemical Parameters.* 1998.

[49] Birkin, P.R. and S. Silva-Martinez, *A study of the effect of ultrasound on mass transport to a microelectrode.* Journal of Electroanalytical Chemistry, 1996. **416**(1-2): p. 127-138.

[50] Leighton, T., A. Walton, and M. Pickworth, *Primary bjerknes forces.* European Journal of Physics, 1990. **11**(1): p. 47.

[51] Gumerov, N., et al., *Robust acoustic wave manipulation of bubbly liquids.* Applied physics letters, 2016. **108**(13): p. 134102.

6 PAPER 2: *In-situ* Sonoactivation of Polycrystalline Ni for the Hydrogen Evolution Reaction (HER) in Alkaline Media

Faranak Foroughi[1], Alaa Y. Faid[2], Svein Sunde[2], Gregory Jerkiewicz[1,3], Christophe Coutanceau[1,4,5], Bruno G. Pollet[1,6*]*

[1]Hydrogen Energy and Sonochemistry Research Group, Department of Energy and Process Engineering, Faculty of Engineering, Norwegian University of Science and Technology (NTNU), NO-7491 Trondheim, Norway

[2]Electrochemistry Research Group, Department of Materials Science and Engineering, Faculty of Natural Sciences. NTNU, NO-7491 Trondheim, Norway

[3]Department of Chemistry, Queen's University, 90 Bader Lane, Kingston, Ontario, K7L 3N6, Canada

[4]Catalysis and Non-Conventional Medium group, IC2MP, UMR CNRS 7285, Université de Poitiers, 4 Rue Michel Brunet, 86073 Poitiers Cedex 9, France

[5]French Research Network on Hydrogen (FRH2), Research federation n°2044 CNRS, France

[6]Green Hydrogen Lab (GH2Lab), Pollet Research Group, Hydrogen Research Institute, Université du Québec à Trois-Rivières, 3351 Boulevard des Forges, Trois-Rivières, Québec G9A 5H7, Canada

[*] Corresponding authors: bruno.pollet@uqtr.ca (B.G.P.)
gregory.jerkiewicz@queensu.ca (G.J.)

Abstract

Nickel (Ni) and Ni-based materials have attracted great interest in the development of renewable energy technologies, including fuel cells and water electrolysers, due to their good stability, catalytic activity, abundance, and lower cost when compared to the currently used Platinum Group Metals (PGM)-based materials. In this work, we report on the design a facile and scalable approach for activating the surface of metallic Ni for the hydrogen evolution reaction (HER) in aqueous alkaline media through continuous and pulsed ultrasound (24 kHz, 44 W, 60% acoustic amplitude, ultrasonic horn). Sonoactivated Ni shows a remarkably enhanced HER activity with a much lower overpotential at −10 mA cm^{-2} of −277 mV *vs.* RHE when compared to non-sonoactivated Ni. It is revealed that the ultrasonic treatment mechanism is a time-dependent process that gradually oxidizes the Ni material and leads to the formation of $Ni(OH)_2$ and NiO when the treatment is 60 min in duration, while reducing Ni surface when the treatment time is 75 min. Furthermore, longer ultrasonication times (>75 min) resulted in higher HER activity. The outcome of our research offers a novel route for activating nickel-based materials by ultrasonic treatment to tune the chemical composition and electrocatalytic activity of the Ni surface for the electrochemical water splitting reaction.

Keywords: Polycrystalline nickel; Hydrogen evolution reaction; Alkaline water electrolysis; Ultrasound; Sonoelectrochemistry; Enhancement of electrocatalytic activity.

7 PAPER 3: Unveiling Hydrogen Evolution Dependence on KOH Concentration for Polycrystalline and Nanostructured Nickel-based Catalysts

Alaa Y. Faid[1*], Faranak Foroughi[1,2**], Svein Sunde[1], Bruno Pollet[2,3]

[1]Electrochemistry Research Group, Department of Materials Science and Engineering, Faculty of Natural Sciences. Norwegian University of Science and Technology (NTNU), NO-7491 Trondheim, Norway

[2]Hydrogen Energy and Sonochemistry Research Group, Department of Energy and Process Engineering, Faculty of Engineering, Norwegian University of Science and Technology (NTNU), NO-7491 Trondheim, Norway

[3]Green Hydrogen Lab, Pollet Research Group, Hydrogen Research Institute (HRI), Université Du Québec à Trois-Rivières (UQTR), 3351 Boulevard des Forges, Trois-Rivières, Québec G9A 5H7, Canada

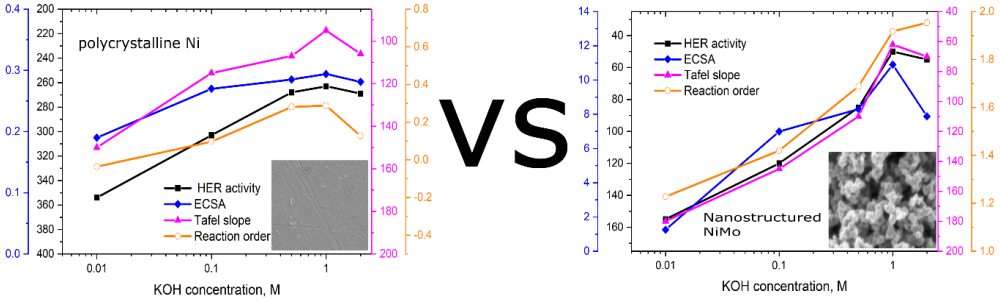

Authors to whom correspondence should be addressed:

* Alaa Y. Faid: alaa.faid@ntnu.no

** Faranak Foroughi: faranak.foroughi@ntnu.no

Abstract

Nickel-based hydrogen evolution reaction (HER) electrodes have been widely used in alkaline and anion exchange membrane (AEM) water electrolysis. Therefore, understanding the activity dependence on the KOH concentration (pH) of alkaline electrolytes is essential for designing durable and active HER catalysts. In this work, the HER activity and kinetics of polycrystalline and nanostructured nickel-based catalysts are evaluated in various pHs and KOH concentrations. The results for nanostructured NiMo catalyst indicate that both electrochemical active surface area (ECSA) and reaction order has a promoting region under various pH's and KOH concentrations (0.01 to 1.0 M, pH=12-14) accompanied with better HER activity (a lower overpotential for achieving -10 mA cm^{-2}) and Tafel slope decreases from around 180 mV dec^{-1} to 60 mV dec^{-1} in the same pH and KOH concentration range. The change in the Tafel slope indicates that HER rate-determining step for HER at NiMo/C changes with pH and KOH concentration. The polycrystalline Ni displays different behaviour where a promoting (0.01 to 0.10 M, pH = 12-13), stabilizing (0.1 to 1.0 M, pH 13-14), and an inhibiting region (2M, pH > 14) are present. However, Tafel slopes of around 120 mV dec^{-1} are obtained for polycrystalline Ni at all KOH concentrations. The HER characteristics are inhibited at 2.0 M KOH for both catalysts due to slower OH^- transport kinetics. The results confirmed the importance of tuning catalyst-pH/KOH concentration for better HER activity and kinetics.

Keywords: Hydrogen evolution reaction (HER); nickel; catalyst-electrolyte interaction; KOH effect; alkaline electrolysis.

8 PAPER 4: Sonoactivated Polycrystalline Ni Electrodes for Alkaline Oxygen Evolution Reaction

Faranak Foroughi[1,2*], Alaa Y. Faid[2], Svein Sunde[2], Bruno G. Pollet[1,3]

[1]Hydrogen Energy and Sonochemistry Research Group, Department of Energy and Process Engineering, Faculty of Engineering, Norwegian University of Science and Technology (NTNU), NO-7491 Trondheim, Norway

[2]Electrochemistry Research Group, Department of Materials Science and Engineering, Faculty of Natural Sciences. Norwegian University of Science and Technology (NTNU), NO-7491 Trondheim, Norway

[3]Green Hydrogen Lab (GH2Lab), Pollet Research Group, Hydrogen Research Institute, Université du Québec à Trois-Rivières, 3351 Boulevard des Forges, Trois-Rivières, Québec G9A 5H7, Canada

Authors to whom correspondence should be addressed: *faranak.foroughi@ntnu.no

Abstract

The development of cost-effective and active water-splitting electrocatalysts is an essential step towards the realization of sustainable energy. Its success requires an intensive improvement in the kinetics of the anodic half-reaction of the oxygen evolution reaction (OER), which determines the overall system efficiency to a large extent. In this work, we designed a facile and one-route strategy to activate the surface of metallic nickel (Ni) for the OER in alkaline media by ultrasound (24 kHz, 44 W, 60% acoustic amplitude, ultrasonic horn). Sonoactivated Ni showed enhanced OER activity with a much lower potential at +10 mA cm^{-2} of +1.594 V *vs.* RHE after 30 min ultrasonic treatment compared to +1.617 V *vs.* RHE before ultrasonication. In addition, lower charge transfer resistance of 11.1 Ω was observed for sonoactivated Ni as compared to 98.5 Ω for non-sonoactivated Ni. In our conditions, ultrasound did not greatly affect the electrochemical surface area (A_{ecsa}) and Tafel slopes however, the enhancement of OER activity can be due to the formation of free $OH^{\bullet}$ radicals resulting from cavitation bubbles collapsing at the electrode/electrolyte interface.

Keywords: Electrolysis; Oxygen evolution reaction; Alkaline; Nickel; Ultrasound

8.1 Introduction

The water electrolysis process occurs through two simultaneous half-cell reactions: the oxygen evolution reaction (OER) on the anode and the hydrogen evolution reaction (HER) on the cathode. The Alkaline OER is a 4-electron–proton transfer process which makes the reaction sluggish with high overpotential and complex reaction mechanisms [1, 2]. Nickel (Ni)-based compounds including Ni-based oxides and (oxy)hydroxides are among the most efficient precious-metal-free catalysts for alkaline OER due to their desirable advantages such as enhanced reaction kinetics and structure/performance stability [3]. Relationships between metallic Ni and various O-containing surface compounds formed during anodic oxidation of polycrystalline Ni in aqueous alkaline media can be described by the Bode diagram (Figure 8.1) [4]. Mild anodic polarization of metallic Ni results in the reversible formation of α-$Ni(OH)_2$; moderate anodic polarization results in the irreversible conversion of α-$Ni(OH)_2$ into β-$Ni(OH)_2$ as well as in the direct oxidation of Ni to β-$Ni(OH)_2$; and, this process is accompanied by the development of NiO that is sandwiched between Ni and β-$Ni(OH)_2$ (marked as a NiO sandwich in Figure 2). The purple lines and the formation of γ-NiOOH were suggested by Bode [5]. The γ-NiOOH phase is believed to be the highest-achievable Ni oxidation state [6]. It is most commonly assumed that the β-NiOOH oxidation phase is most active towards the OER [7].

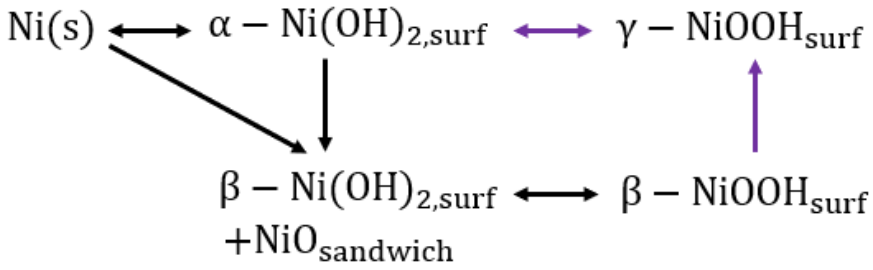

Figure 8.1. Schematic diagram of relationships between metallic Ni and various O containing surface compounds formed during anodic oxidation of polycrystalline Ni in aqueous alkaline media [4].

So far, much research efforts have focussed on improving the OER performance of Ni by the design and optimization of the catalyst structure [6, 8, 9].

Sonoelectrochemistry is the combination of ultrasound with electrochemistry. The use of ultrasound in electrochemistry offers many advantages including [10]: a) gas bubble removal

at the electrode surface; b) solution degassing; c) disruption of the *Nernst* diffusion layer; d) enhancement of mass transport of electroactive specious through the double layer; and, e) activation and cleaning of the electrode surface. Recently, it was reported that ultrasonication greatly enhances electrocatalytic properties of metallic surfaces [11-16]. Our group also investigated the effect of ultrasound on Ni(poly) in alkaline media and found that the rate of the HER was greatly enhanced.

In this work, we investigated the effects of ultrasound (24 kHz) on the OER on polycrystalline Ni(poly) immersed in 1.0 M aqueous KOH solution at room temperature. We applied ultrasound (i) during linear sweep voltammetry (LSV) experiments and (ii) for surface treatment of the Ni(poly) electrode for 30 min and then we conducted the LSV experiments under *silent* conditions (in the absence of ultrasound).

8.2 Experimental

All electrochemical experiments were carried out using a potentiostat/galvanostati (BioLogic-SP 150) in a three-electrode configuration. The voltammetry experiments were performed using a double-jacketed sonoelectrochemical cell. Ultrasonication was applied by a f = 24 kHz ultrasonic probe (Hielscher UP200S, 200 W @ 60% fixed amplitude, the tip ∅ = 14 mm, and the tip area = 153.9 mm^2 (1.5386 cm^2). The ultrasonic or acoustic power (P_{acous}) was found to be 44 ± 1.40 W by calorimetrically using the methods of Margulis *et al.* [17] and Contamine *et al*. [18]. In order to keep the temperature at T = 298±1 K a refrigerated circulator (JULABO, Germany) was connected to the sonoelectrochemical cell.

A polycrystalline nickel Ni(poly) disc (∅ = 5 mm) of geometric surface area (A_{geom}) of 0.196 cm^2 was used as a working electrode (WE). The WE was mechanically polished using alumina suspension (down to 0.05 μm, Buehler Micro polish) to obtain a mirror-like surface rinsed with UHP water, ultrasonicated in UHP water for ~30 s and finally rinsed in UHP water under ultrasonic conditions. The reference electrode (RE) was a homemade reversible hydrogen electrode (RHE) [19]. All potential values in this work are reported with respect to the RHE. Counter electrode (CE) was a Ni mesh (40 mesh woven from 0.13 mm diameter wire, 99.99% metal basis, Alfa Aesar, Germany) in a rectangle shape (20.67 × 10.76 mm^2). Its surface area was at least 10 times larger than that of the WE. The distance between the ultrasonic probe and the working electrode was ca. 3 cm. The experiments were carried out in

N_2 (g) (99.999%) saturated 1.00 M (pH = 13.7) aqueous KOH (Sigma-Aldrich, 99.99% in purity) solution prepared using ultra-high-purity water (Millipore, 18.2 MΩ cm in resistivity).

The performance of Ni(poly) towards the OER in aqueous alkaline electrolytes was investigated by a series of linear sweep voltammetry (LSV) in the potential region of $+1.10 \leq E_{app} \leq +1.70$ V *vs.* RHE at the potential scan rate of $\nu = 0.30$ mV s^{-1} in 1.0 M KOH aqueous solutions in the absence of ultrasound (*silent* conditions), during (with) ultrasound and after 30 min ultrasound.

The potential values from linear sweep voltammetry (LSV) experiments were *IR* corrected using the following equation (8.1):

$$E_{\text{IR-corrected}} = E_{app} - IR \qquad (8.1)$$

where I is the measured current and R the electrolyte resistance, measured for each electrolyte employed. The R value was determined by electrochemical impedance spectroscopy (EIS) in the high frequency region from the value of the *real* impedance (Z') where the *imaginary* impedance (Z'') is zero in Nyquist plot. The EIS experiments were carried in the 100 kHz to 0.1 Hz frequency (f) range with a voltage perturbation of +10 mV at an applied potential of +1.60 V vs. RHE at $T = 298$ K .

The surface structure and morphology of Ni(poly) electrode before and after ultrasound treatment were studied using a scanning electron microscope (SEM) Zeiss-Ultra 55-FEG-SEM operating at 10 kV accelerating voltage.

8.3 Results and Discussion

8.3.1 Study of the Effect of Ultrasound on the Electrochemical Surface Area of Polycrystalline Ni

In order to study the effects of power ultrasound on the electrochemical surface area of Ni(poly), the "capacitance" and "β-NiOOH" methods were used. The "Capacitance" method consists of cycling the Ni electrodes at different scan rates in a non-faradic charging process to determine the electrochemical surface area (A_{ecsa}) [20]. A series of cyclic voltammograms (CVs) on Ni(poly) in 1.0 M KOH were generated at different scan rates (5, 10, 20, 50, 100, 200, 300, 400 mV s^{-1}) in the potential region of +0.80 V *vs.* RHE to +0.90 V *vs.* RHE. The double-layer capacitance value (C_{dl}) was obtained by plotting the charging current (I_c, A) vs. scan rate (v, V s^{-1}) and by using equation (8.2):

$$Slope = C_{dl} = \frac{\Delta I_c}{\Delta v} \qquad (8.2)$$

The electrochemical surface area was calculated by using the specific capacitance density (c) of 40 μF cm^{-2} and equation (8.3) [20]:

$$A_{ecsa} = \frac{C_{dl}}{c} \qquad (8.3)$$

Figure 2a and 2b show the CVs of Ni(poly) electrode before and after 30 minutes of ultrasonication at different scan rates (5, 10, 20, 50, 100, 200, 300, and 400 mV s^{-1}) in the potential range of $+0.80 \leq E_{app} \leq +0.90$ V *vs.* RHE where non-faradic currents occur. Figure 2c shows plots of current *vs.* scan rate at a potential of +0.85 V *vs.* RHE before and after 30 mins of ultrasonic exposure.

The "β-NiOOH" method consisted of integrating the β-NiOOH reduction peak once steady-state polarization was reached at a high scan rate. The β-NiOOH method was carried out by running 10 CV cycles from $+0.50 \leq E_{app} \leq +1.60$ V vs. RHE at scan rate of $v = 100$ mV s^{-1} before and after 30 min US (Figure 2d). The A_{ecsa} values for this method were calculated using the β-NiOOH reduction peak of the 10th cycle (from 1.2 to 1.4 V *vs.* RHE) divided by the specific charge density of 420 μC cm^{-2} (equation 8.4) [20, 21]:

$$A_{\text{ecsa}} = \frac{Q_{ox}}{420} \qquad (8.4)$$

Where Q is the charge associated with the β-NiOOH reduction peak. The A_{ecsa} values before and after 30 min of ultrasonication treatment for both capacitance and beta methods are summarised in Table 8.1. It can be observed from Table 8.1 that ultrasound does not seem to affect the electrochemical surface area of Ni(poly) electrode, indicating that the electrochemical surface area was not significantly modified due to erosion caused by the

implosion of acoustic cavitation bubbles on the electrode surface [22]. Figures 8.2e and 8.2f shows the SEM images of Ni(poly) before and after 30 min US. Before US a smooth surface is seen except the scratches due to mechanical polishing. After 30 min US some irregular pits could be observed, however, it is unclear whether these arose from the actions of inter-facial ultrasound. Such features are sometimes found widely scattered across non-sonicated surfaces (see, for example some pits in non-sonicated electrode Figure 8.2e). These pits have a little influence on electrochemical measurements because there are very few of them and their contribution to total A_{ecsa} is relatively small. Aqueous ultrasonication did not significantly roughen electrode and the surface roughness remained almost unchanged [23].

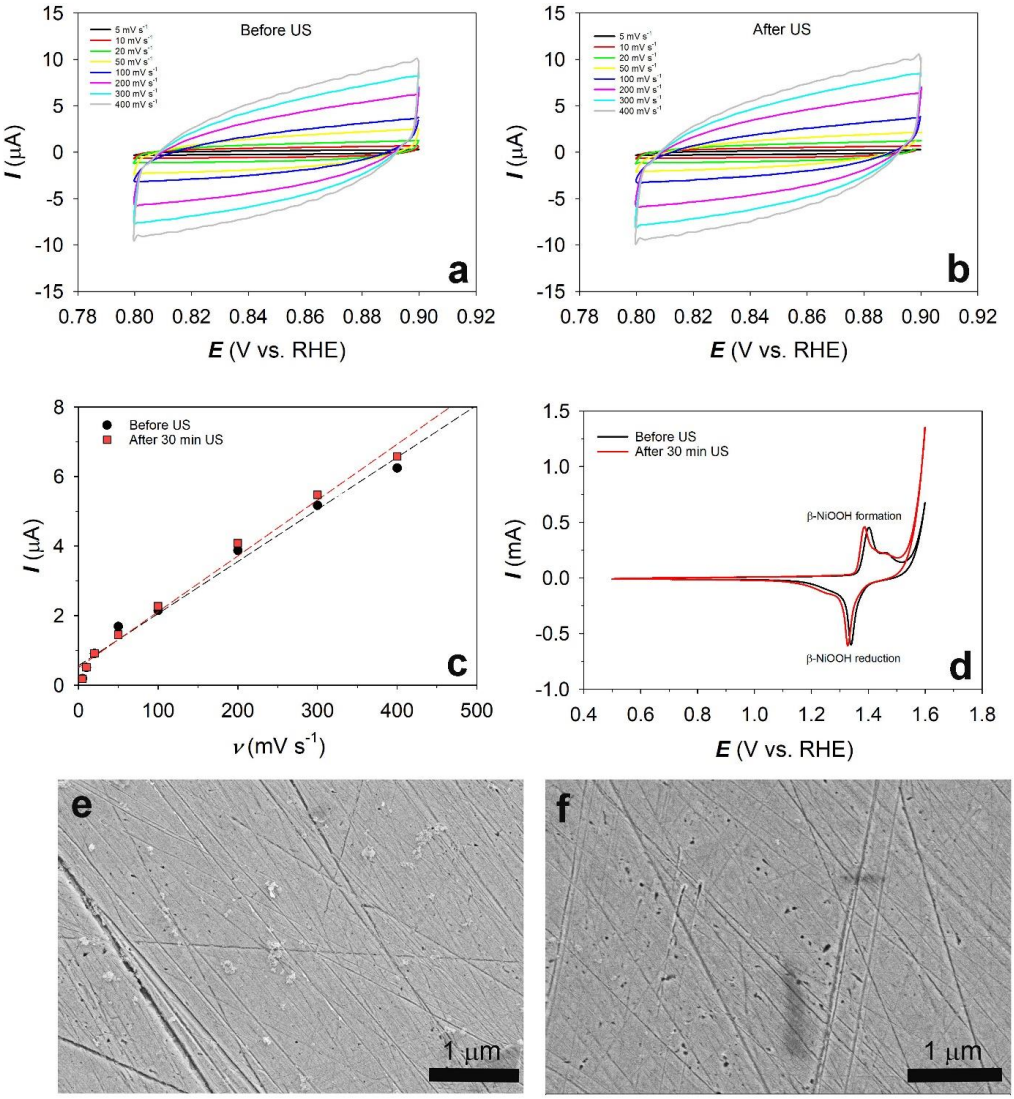

Figure 8.2. Cyclic voltammetry (CV) scans of Ni(poly) electrode in 1.0 M aqueous KOH solution at different scan rates (5, 10, 20, 50, 100, 200, 300 and 400 mV s^{-1}), $+0.80 \leq E_{app} \leq +0.90$ V *vs.* RHE and $T = 298$ K a) before and b) after ultrasonication for 30 minutes, c) The capacitance method: plots of current vs. scan rate as well as linear regressions of each data set (dotted lines), obtained from the CV experiments at an applied potential of +0.85 V *vs.* RHE before and after 30 min ultrasonication, d) CV profiles of Ni(poly) at $+0.5 \leq E_{app} \leq +1.60$ V *vs.* RHE and at scan rate of $\nu = 100$ mV s^{-1} before and after 30 min US. SEM images of the Ni(poly) electrode e) before and f) after 30 min ultrasonication.

Table 8.1. The electrochemical surface area (A_{ecsa}) of Ni(poly) electrode before and after 30 min ultrasonication in 1.0 M aqueous KOH solution and T = 298 K. (n=3)

Material	$A_{ecsa(capacitance)}$ (cm^2)	$A_{ecsa\ (beta)}$ (cm^2)
Ni (Before ultrasonication)	0.38 ± 0.009	0.88 ± 0.004
Ni (After ultrasonication)	0.40 ± 0.005	0.95 ± 0.035

8.3.2 Study of the Effect of Ultrasonic Power on the Oxygen Evolution Reaction

The effect of ultrasound on the oxygen evolution reaction (OER) at Ni(poly) in 1.0 M aqueous KOH solution was investigated by linear sweep voltammetry (LSV). Figure 8.3a shows the LSVs for the OER on Ni(poly) in N_2 saturated 1.0 M KOH aqueous solutions at a low scan rate of v = 0.3 mV s^{-1} before, during (with) and after 30 min ultrasonic treatment. It can be observed that the ultrasonic (US) treatment increases the OER activity. Figure 8.3b demonstrates the Tafel plots obtained from the LSV curves in the OER region. Tafel slopes (b) at low and high overpotentials and the potential at +10 mA cm^{-2} ($E_{+10\ mA\ cm^{-2}}$) are tabulated in Table 8.2. Results from Table 8.2 indicates that lower potential requires to reach +10 mA cm^{-2} in presence of ultrasound and after ultrasonic treatment. However, even when ultrasound is "on" during the OER experiments, the lower overpotential at +10 mA cm^{-2} is required when compared to after ultrasonic treatment.

Ni-based materials show the Tafel slope values between 40 mV dec^{-1} to 130 mV dec^{-1}. Also, it is well known that there are generally two Tafel regions for the OER, separated at ~1.5 V *vs.* RHE in 1.0 M KOH [6, 7]. According to Table 8.2, the Tafel slopes of 52, 55, 50 mV dec^{-1} at low overpotential and 141, 90 and 130 mV dec^{-1} at high overpotentials obtained for the OER on Ni(poly) before ultrasonication (US), with US and after 30 min US, respectively. The Tafel slopes are in good agreement with the literature [7, 24, 25]. By comparing the Tafel slopes under different US conditions reported in Table 8.2, it can be concluded that ultrasound does not change the Tafel slopes significantly for the OER and does not affect the mechanism of OER. It is worth mentioning that the experiments have been repeated for several times and almost the same values have been obtained showing the reproducibility of the work.

Figure 8.3c illustrates the plot of E at +10 mA cm^{-2} ($E_{+10\ \mathrm{mA\ cm^{-2}}}$) *vs*. different ultrasonic conditions. It can be seen in Figure 8.3c that the overpotential to reach +10 mA cm^{-2} decreases when US is "on" during OER experiment.

Figure 8.3d shows the Nyquist representation of the impedance data of Ni(poly) before US, with US and after 30 min US at T = 298 K and at E = +1.60 V *vs.* RHE. For all US conditions, a depressed semi-circle can be seen. Accordingly, the data were approximated by the modified Randles circuit shown in Figure 8.3d, whereas the capacitance is replaced by a constant phase element. Note, for $\alpha = 1$ the CPE reflects an ideal capacitance. R_s correlates with the cell ohmic resistance (electrodes). R_{ct} represents the charge transfer resistance and may also include other contributions such as the adsorption of intermediates. CPE is a constant phase element that is often associated with the capacitive charging of a rough electrode. The parameters obtained from the EIS measurement are shown in Table 8.3. According to Table 8.3, the Ni(poly) electrode after 30 min US treatment has the lowest charge transfer resistance compared to the two other conditions. While the R_s are almost constant in all US conditions. Since no significant increase in electrochemical surface area has been observed on Ni(poly) by applying US, the enhancement of OER activity of Ni(poly) after ultrasonication treatment could be due to the reaction of radicals at electrode/electrolyte interface such as ($OH^{\bullet}$, $H^{\bullet}$, H_2O_2, etc) caused by collapsing cavitation bubbles. It was reported before that such radicals could reacts with the electrolyte species and producing a secondary sonochemical reactions [15, 16, 26, 27].

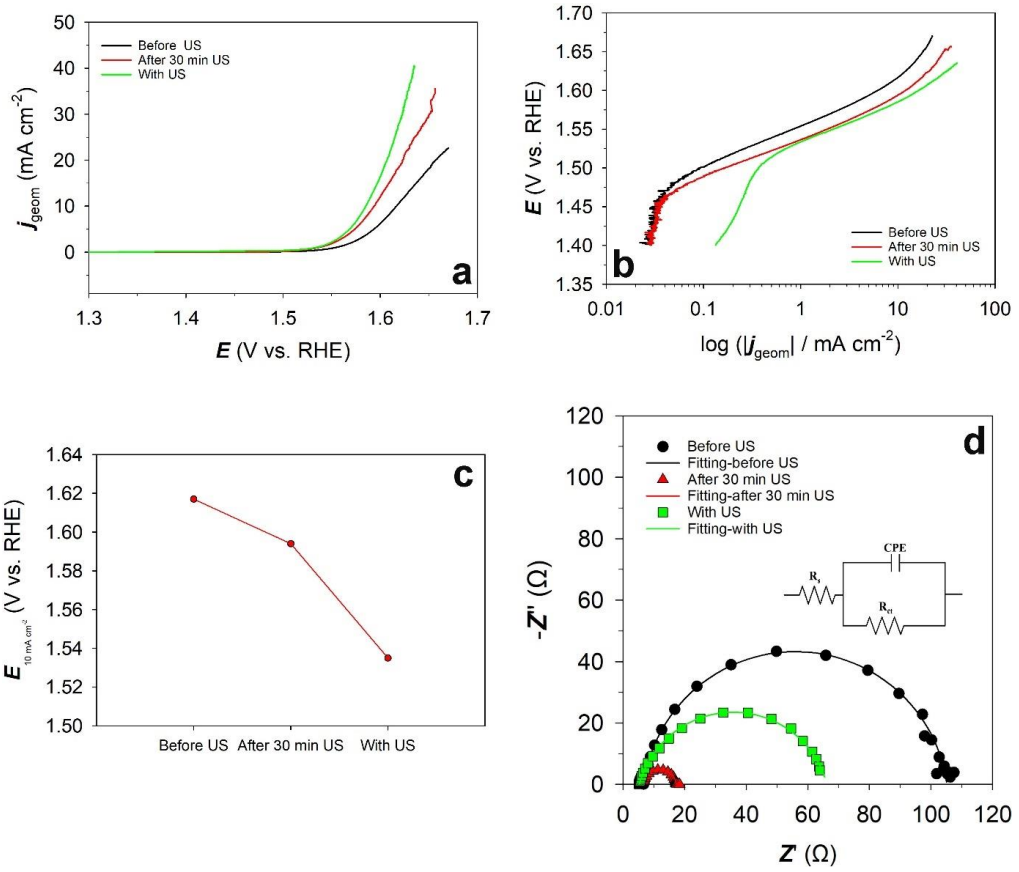

Figure 8.3. a) Linear sweep voltammograms (LSVs) for the OER, b) overlaid Tafel plots c) plot of E at 10 m A cm^{-2} vs. various US conditions and d) Nyquist plots; Insets show the equivalent circuit used to fit the impedance data of Ni(poly) electrode in N_2 saturated 1.0 M aqueous KOH solution on a at a scan rate of $\nu = 0.3$ mV s^{-1} and at $T = 298$ K before US, with US and after 30 min US treatment.

Table 8.2. Tafel slopes (b) and potential at 10 mA cm^{-2} ($E_{10\ mA\ cm^{-2}}$) for the OER on Ni(poly) disc electrode in 1.0 M KOH aqueous solutions before US, with US and after 30 min US.

Ni(poly)	b^* (mV dec^{-1}) at low overpotential	b^{**} (mV dec^{-1}) at high overpotential	$E_{+10\ mA\ cm^{-2}}$ (V vs. RHE)
Before US	52	141	1.617
With US	55	90	1.535
After 30 min US	50	130	1.594

* $1.45 \leq E \leq 1.55$

** $1.60 \leq E \leq 1.65$

Table 8.3. Cell ohmic resistance (R_s) and charge transfer resistance (R_{ct})

Ni(poly)	R_s (Ω)	R_{ct} (Ω)
Before US	6.69	98.5
With US	6.60	61.0
After 30 min US	6.25	11.1

8.4 Conclusions

We have developed a simple *in-situ* method to activate Ni(poly) electrodes in 1.0 M aqueous KOH solution towards the OER by ultrasonic treatments (24 kHz, 60% amplitude, 44 W) for 30 minutes. It was shown that ultrasound improves Ni(poly) OER activity by reducing the overpotential needed to achieve +10 mA cm^{-2} by -23 mV and charge transfer resistance from 98.5 Ω before US to 11.1 Ω after 30 min US treatment. However, the US treatment does not affect the electrochemical surface area of Ni(poly) or Tafel slope. The enhancement of OER activity of Ni(poly) could be attributed to the formation of free radicals by collapsing of cavitation bubbles and the secondary sonochemical reactions at the electrode/electrolyte interface.

Acknowledgement

The authors would like to thank NTNU and ENERSENSE for the 3-year financial support towards FF's doctoral studies. FF would like to thank Professors Gregory Jerkiewicz and Christophe Coutanceau for their useful advice.

References

[1] Suen, N.-T., et al., *Electrocatalysis for the oxygen evolution reaction: recent development and future perspectives.* Chemical Society Reviews, 2017. **46**(2): p. 337-365.

[2] Hu, C., L. Zhang, and J. Gong, *Recent progress made in the mechanism comprehension and design of electrocatalysts for alkaline water splitting.* Energy & Environmental Science, 2019. **12**(9): p. 2620-2645.

[3] Chen, Y., et al., *Recent Progress on Nickel-Based Oxide/(Oxy) Hydroxide Electrocatalysts for the Oxygen Evolution Reaction.* Chemistry–A European Journal, 2019. **25**(3): p. 703-713.

[4] Alsabet, M., M. Grdeń, and G. Jerkiewicz, *Electrochemical growth of surface oxides on nickel. Part 3: Formation of β-NiOOH in relation to the polarization potential, polarization time, and temperature.* Electrocatalysis, 2015. **6**(1): p. 60-71.

[5] Bode, H., K. Dehmelt, and J. Witte, *Zur kenntnis der nickelhydroxidelektrode—I. Über das nickel (II)-hydroxidhydrat.* Electrochimica Acta, 1966. **11**(8): p. 1079-IN1.

[6] Cossar, E., et al., *The performance of nickel and nickel-iron catalysts evaluated as anodes in anion exchange membrane water electrolysis.* Catalysts, 2019. **9**(10): p. 814.

[7] Fabbri, E., et al., *Developments and perspectives of oxide-based catalysts for the oxygen evolution reaction.* Catalysis Science & Technology, 2014. **4**(11): p. 3800-3821.

[8] Shinagawa, T., M.T.K. Ng, and K. Takanabe, *Boosting the performance of the nickel anode in the oxygen evolution reaction by simple electrochemical activation.* Angewandte Chemie International Edition, 2017. **56**(18): p. 5061-5065.

[9] Shinde, P., et al., *Optimized performance of nickel in crystal-layered arrangement of NiFe2O4/rGO hybrid for high-performance oxygen evolution reaction.* International Journal of Hydrogen Energy, 2021. **46**(2): p. 2617-2629.

[10] Pollet, B., *Power Ultrasound in Electrochemistry: From Versatile Laboratory Tool to Engineering Solution*. 2012: John Wiley & Sons.

[11] Dulle, J., et al., *Sonochemical activation of Al/Ni hydrogenation catalyst.* Advanced Functional Materials, 2012. **22**(15): p. 3128-3135.

[12] Abdullah, M.I., et al., *Ultrasonically Surface-Activated Nickel Foam as a Highly Efficient Monolith Electrode for the Catalytic Oxidation of Methanol to Formate.* ACS Applied Materials & Interfaces, 2021. **13**(26): p. 30603-30613.

[13] Pollet, B.G., *A novel method for preparing PEMFC electrodes by the ultrasonic and sonoelectrochemical techniques.* Electrochemistry communications, 2009. **11**(7): p. 1445-1448.

[14] Pollet, B.G., *The use of ultrasound for the fabrication of fuel cell materials.* international journal of hydrogen energy, 2010. **35**(21): p. 11986-12004.

[15] Cherepanov, P.V., M. Ashokkumar, and D.V. Andreeva, *Ultrasound assisted formation of Al–Ni electrocatalyst for hydrogen evolution.* Ultrasonics sonochemistry, 2015. **23**: p. 142-147.

[16] Cherepanov, P.V., et al., *The use of ultrasonic cavitation for near-surface structuring of robust and low-cost AlNi catalysts for hydrogen production.* Green chemistry, 2015. **17**(5): p. 2745-2749.

[17] Margulis, M. and I. Margulis, *Calorimetric method for measurement of acoustic power absorbed in a volume of a liquid.* Ultrasonics Sonochemistry, 2003. **10**(6): p. 343-345.

[18] Contamine, R.F., et al., *Power measurement in sonochemistry.* Ultrasonics Sonochemistry, 1995. **2**(1): p. S43-S47.

[19] Jerkiewicz, G., *Standard and reversible hydrogen electrodes: Theory, design, operation, and applications.* ACS Catalysis, 2020. **10**(15): p. 8409-8417.

[20] Cossar, E., et al., *Comparison of electrochemical active surface area methods for various nickel nanostructures.* Journal of Electroanalytical Chemistry, 2020: p. 114246.

[21] Alsabet, M., M. Grden, and G. Jerkiewicz, *Electrochemical growth of surface oxides on nickel. Part 1: formation of α-Ni (OH) 2 in relation to the polarization potential, polarization time, and temperature.* Electrocatalysis, 2011. **2**(4): p. 317-330.

[22] Pollet, B.G., *Does power ultrasound affect heterogeneous electron transfer kinetics?* Ultrasonics sonochemistry, 2019. **52**: p. 6-12.

[23] Madigan, N.A., et al., *Effects of sonication on electrode surfaces and metal particles.* Ultrasonics Sonochemistry, 1996. **3**(3): p. S239-S247.

[24] Van Drunen, J., et al., *Electrochemically active nickel foams as support materials for nanoscopic platinum electrocatalysts.* ACS applied materials & interfaces, 2014. **6**(15): p. 12046-12061.

[25] Huang, Y., et al., *Highly efficient oxygen evolution reaction enabled by phosphorus doping of the Fe electronic structure in iron–nickel selenide nanosheets.* Advanced Science, 2021. **8**(18): p. 2101775.

[26] Theerthagiri, J., et al., *Application of advanced materials in sonophotocatalytic processes for the remediation of environmental pollutants.* Journal of Hazardous Materials, 2021. **412**: p. 125245.

[27] Theerthagiri, J., et al., *Sonoelectrochemistry for energy and environmental applications.* Ultrasonics Sonochemistry, 2020. **63**: p. 104960.

9 PAPER 5: Understanding the Effects of Ultrasound (408 kHz) on the Hydrogen Evolution Reaction (HER) and the Oxygen Evolution Reaction (OER) on Raney-Ni in Alkaline Media

Faranak Foroughi[1*], Christian Immanuel Bernäcker[2], Lars Röntzsch[2], Bruno G. Pollet[1,3]

[1]Hydrogen Energy and Sonochemistry Research Group, Department of Energy and Process Engineering, Faculty of Engineering, Norwegian University of Science and Technology (NTNU), NO-7491 Trondheim, Norway

[2]Fraunhofer Institute for Manufacturing Technology and Advanced Materials IFAM, Branch Lab Dresden, Winterbergstraße 28, 01277 Dresden, Germany

[3]Green Hydrogen Lab (GH2Lab), Pollet Research Group, Hydrogen Research Institute, Université du Québec à Trois-Rivières, 3351 Boulevard des Forges, Trois-Rivières, Québec G9A 5H7, Canada

Authors to whom correspondence should be addressed: *faranak.foroughi@ntnu.no

Abstract

The hydrogen evolution reaction (HER) and the oxygen evolution reaction (OER) occurring at the Raney-Ni mesh electrode in 30 wt.-% aqueous KOH solution were studied in the absence (*silent*) and presence of ultrasound (408 kHz, ~54 W, 100% acoustic amplitude) at different electrolyte temperatures (T = 25, 40 and 60 °C). Linear sweep voltammetry (LSV) and electrochemical impedance spectroscopy (EIS) experiments were performed to analyse the electrochemical behaviour of the Raney-Ni electrode under these conditions. Under *silent* conditions, it was found that the electrocatalytic activity of Raney-Ni towards the HER and the OER depends upon the electrolyte temperature, and higher current densities at lower overpotentials were achieved at elevated temperatures. It was also observed that the HER activity of Raney-Ni under ultrasonic conditions increased at low temperatures (e.g., 25 °C) while the ultrasonic effect on the OER was found to be insignificant. In addition, it was observed that the ultrasonic effect on both the HER and OER decreases by elevating the temperature. In our conditions, it is suggested that ultrasound enhances the electrocatalytic performance of Raney-Ni towards the HER due to principally the efficient gas bubble removal from the electrode surface and the dispersion of gas bubbles into the electrolyte, and this effect depends upon the behaviour of the hydrogen and oxygen gas bubbles in alkaline media.

Keywords: Hydrogen evolution reaction (HER); Oxygen evolution reaction (OER); Raney-Nickel; Alkaline; Ultrasound; Sonoelectrochemistry.

9.1 Introduction

Water electrolysis is the most significant primary electrochemical method for molecular hydrogen (H_2) production, and its importance is increasing rapidly with affordable renewable energy production [1]. The electrolysis of water involves two half-cell reactions: the hydrogen evolution reaction (HER) taking place at the cathode (the negative electrode) and the oxygen evolution reaction (OER) at the anode (the positive electrode) [2]. Depending on the electrolytes, separators, working temperatures and pressures employed, currently, there are five main types of water electrolysers, namely [1, 2]:

6. Proton exchange membrane water electrolyser (PEMWE, liquid water, perfluorosulfonic acid (PFSA), < 80 °C, < 200 bar);
7. Alkaline water electrolyser (AWE, 30-40% KOH or NaOH, < 80 °C, < 30 bar);
8. Anion exchange membrane water electrolyser (AEMWE, dilute KOH, < 90 °C, < 30 bar);
9. Solid oxide electrolysis cell (SOEC, water steam, 500-850 °C, atmospheric); and,
10. Proton conducting ceramic electrolyser (PCCEL, water stream, 300-600 °C, < 8 bar).

PEMWEs are still expensive ($1,000 – $2,000/kW) [1, 2] due to the high cost of precious metals (mainly iridium, Ir and platinum, Pt) and other materials such as the polymeric proton exchange membrane (e.g., Nafion®). AWE is a proven technology offering advantages such as the use of inexpensive metals (e.g., nickel, Ni) and materials and lower manufacturing costs and operations [1, 2]. It is expected that the cost of AWE will drop significantly in the next 5 years by optimizing stack design and developing more efficient and long-term stable electrodes, made from inexpensive raw materials, and produced by mass fabrication-suitable processes [1-3].

Raney-type electrodes are made of Ni-Zn and Ni-Al precursor alloys, producing high surface area after leaching in alkaline solutions [4, 5]. Raney-Ni electrodes have shown well-proven good electrocatalytic activity towards the HER (Eq. 9.1) and the OER (Eq. 9.2) in alkaline electrolytes [6-8].

Cathodic reaction: $4H_2O(l) + 4e^- \rightarrow 2H_2(g) + 4OH^-(aq)$ (9.1)

Anodic reaction: $4OH^-(aq) \rightarrow O_2(g) + 2H_2O(l) + 4e^-$ (9.2)

In water electrolysis, the cell voltage (V_{cell}) is a crucial factor representing energy consumption and is expressed in Equation (9.3), where E_a is the anode potential for the OER, E_c is cathode potential for the HER, j is the current density, $\sum R$ is total ohmic resistance, E^{rev} is the theoretical reversible potential (*Nernst*), η_a is the anode overpotential, and η_c is the cathode overpotential [9].

$$V_{cell} = |E_c - E_a| + j \times \sum R = \Delta E^{rev} + |\eta_a| + |\eta_c| + j \times \sum R \quad (9.3)$$

According to Equation (9.3), V_{cell} is comprised of three components, the theoretical reversible cell voltage (ΔE^{rev}), the total cell overpotential ($\Sigma\eta$) and the Ohmic cell voltage drop ($j\Sigma R$). For increasing the water electrolysis rate, reducing the total overpotential is essential to overcome the energy barrier, and thus electrode materials and the effective electrode surface area play a crucial role on reaction overpotential. Another important factor leading to high energy consumption in water electrolysis is the Ohmic voltage drop which is expressed in Equation (9.4).

$$\sum R = R_e + R_m + R_b + R_c \quad (9.4)$$

where R_{e} is the electrolyte resistance, R_{m} is the membrane/separator resistance, R_{b} is the bubble resistance and R_c is the external circuit resistance. The R_{m} and R_{c} are constant in water electrolysis, which can be reduced by optimizing cabling connection and membrane/separator production process. The dispersion of the bubbles in the electrolyte decreases the electroanalyte conductivity and in turns increases R_{e}. In addition, the bubble coverage on the electrode surface act as an insulating layer, reducing the effective surface area of the electrode, yielding high bubble resistance R_{b}. In most cases, the Ohmic voltage drop can be minimized by increasing the electrolyte flowrate, using gravity, using a magnetic field at the gas-evolving electrodes or by applying ultrasound [9].

Overall, the efficiency of water electrolysis can be improved by: (i) enabling the detachment of gas bubbles from the electrodes and the membranes more effective, thereby eliminating gas blanketing; (ii) by promoting faster removal of the bubbles at the electrodes to increase the local heat/mass transfer coefficients; and (iii) by allowing efficient electrolyte degassing, even with very small electrode spacing.

Ultrasound is an acoustic wave that has a frequency above the upper limit of the human hearing range. Power ultrasound or low-frequency ultrasound is a well-defined sound wave in the range of [20 kHz – 2 MHz] and it is regarded as the effects of the sound wave on the medium [9-11]. The most important phenomenon that arises from the propagation of an ultrasonic wave into a liquid is acoustic cavitation [12]. When an ultrasonic wave propagates through a liquid media such as water, many tiny gas bubbles are formed. The phenomenon of the formation of bubbles and their subsequent violent collapse of the bubbles is known as *acoustic cavitation* [12]. The collapsing bubble can generate high temperatures up to 5,000 °C and high pressures up to 2,000 atm [13]. The sonochemical process can occur in three regions as follows [14, 15]:

1. The interior of the cavitation bubble, also called the gaseous region. Here, the cavitation of micro-sized bubbles generates free radicals ($H^{\bullet}$ and $OH^{\bullet}$) by water pyrolysis.
2. The region at the interface of the bubble and liquid (gas-liquid interface), where the generation of $OH^{\bullet}$ radicals is predominant.
3. The region of bulk liquid. In this case, the free radicals generated at the interface of the bubble/liquid region move to the bulk liquid, producing a secondary sonochemical reaction.

The evolution of a cavitation bubble during ultrasonication is shown in Figure 9.1.

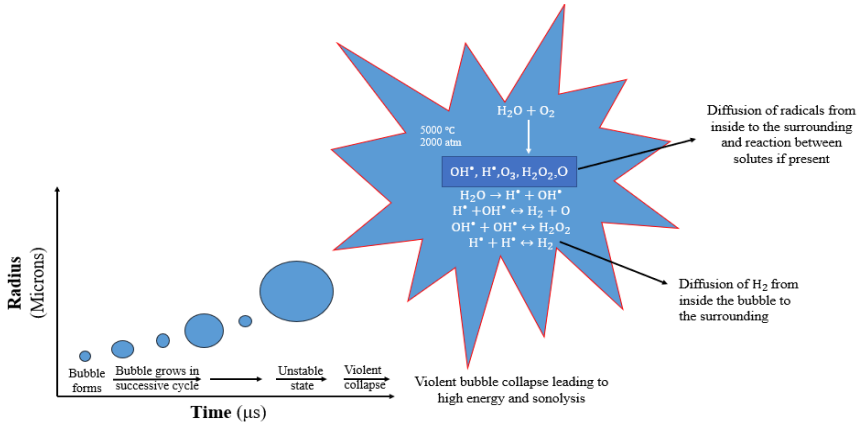

Figure 9.1. The evolution of a cavitation bubble during ultrasonication and the production of sonolysis species by acoustic cavitation.

Sonoelectrochemistry is the combination of power ultrasound with electrochemistry. It has been shown that the use of ultrasound in electrochemistry offers many advantages including [10, 11]:

6. Gas bubble removal at the electrode surface.
7. Solution degassing.
8. Decreased adsorption process.
9. Increased chemical reaction rates.
10. Disruption of the *Nernst* diffusion layer.
11. Enhancement of mass transport of electroactive specious through the double layer.
12. Activation and cleaning of the electrode surface due to the erosion caused by cavitation bubble implosion.

13. Improvement of reaction mechanism by the production of free radicals through the cavitation process.

Water electrolysis under ultrasonication was first studied by Moriguchi in the 1930's using a platinum (Pt) electrode and found that the process occurred at faster rates and lower cell voltages than under *silent* conditions [16]. Hydrogen production in the presence of ultrasound was then continued by the Pollet's research group at the Birmingham Proton Exchange Membrane Fuel Cell in 2011 [10]. For example, Lepesant [17] and other researchers such as Zadeh [18] and Symes [19] studied the influence of ultrasonication on electrolytic hydrogen production from weak acidic (H_2SO_4) and alkaline (NaOH and KOH) solutions using various electrode materials including Pt, industrial carbon (C), glassy carbon (GC) and 316 stainless steel (316-SS). Pollet *et al.* [20] also investigated the effects of ultrasound (26 kHz) on the hydrogen evolution reaction (HER) in the mild acidic electrolyte on polycrystalline Pt. They showed that a 250% enhancement in current density at maximum acoustic power (~30 W) through effective hydrogen bubble removal. Li *et al.* [21] studied the effects of power ultrasound on water electrolysis in various NaOH concentrations. They found that the energy efficiency of water electrolysis was considerably improved in the presence of an ultrasonic field. Overall, the energy-saving for molecular hydrogen production by using an ultrasonic field was found to be in the region of 10–25% for specific electrolyte concentrations, even when high current densities were employed.

Since water electrolysis is an important electrochemical process for generating hydrogen, the possibility of providing the basis for a more realistic cell design for water electrolysis in the presence of ultrasound is a valuable area of investigation [21]. In previous studies, in-depth kinetic analyses were not carried out to shed some light on the effects of ultrasound on the HER and OER mechanisms as well as Tafel parameters in mild acidic and alkaline electrolytes. In this study, we have investigated the effects of ultrasound on the kinetics and mechanism of HER and OER on Raney-Ni in 30 wt.-% aqueous KOH solution at different temperatures (T = 25 °C, 40 °C and 60 °C).

9.2 Experimental Method

All electrochemical experiments were conducted using a potentiostat/galvanostat (BioLogic-SP 150) in a conventional three-electrode configuration using a 30 wt.-% KOH (Sigma-Aldrich, 99.99% in purity) solution at $T = 25$, 40 and 60 °C. All solutions were prepared by using ultra-high purity deionized water (Millipore, 18.2 MΩ cm in resistivity). Raney-Ni electrodes were synthesized by Fraunhofer IFAM and used as working electrodes (WE). The Raney-Ni electrodes were produced in three steps: a) spraying of an aqueous binder solution followed by the deposition of alumimim (Al) powder onto a Ni-mesh, b) heat-treatment to produce the Ni-Al phases (Ni_2Al_3 and $NiAl_3$), and c) leaching of the electrodes. Their production and preparation are fully described elsewhere [7]. For each sonoelectrochemical experiment, a fresh Raney-Ni electrode was used. A Ni mesh (40 mesh woven from 0.13 mm diameter wire, 99.99% metal basis, Alfa Aesar, Germany) was cut out in a rectangle shape (20.67 × 10.76 mm) and used as a counter electrode (CE). The reference electrode (RE) was a mercury/mercury oxide (Hg/HgO) filled with 30 wt.% KOH solution (the same electrolyte). All potentials in this work are reported with respect to RHE ($E_{RHE} = E_{Hg/HgO} + 0.90$ V). Also, potential values were *IR* compensation corrected based upon Equation (9.5):

$$E_{IR\text{-corrected}} = E - IR \qquad (9.5)$$

where I is the measured current and R the electrolyte resistance, measured for each electrolyte solutions employed. The R value was determined by electrochemical impedance spectroscopy (EIS) from the value of the *real* impedance (Z') where the *imaginary* impedance (Z'') is zero in the Nyquist plot. The EIS experiments were carried out from 100 kHz to 0.1 Hz with a voltage perturbation of ±10 mV at $T = 25$, 40 and 60 °C.

All current densities are given in relation to the geometric surface area of the electrodes ($A_{geo} = 0.085$ cm^2) and are referred to as j. The geometric surface area comprises only the front side of the electrode and neglecting the holes of the used mesh. Consequently, the surface area is underestimated [7]. The electrochemical surface area (A_{ecsa}) was determined electrochemically by calculating the double-layer capacitance, C_{dl}, from cyclic voltammetry (CV) experiments. The CV experiments were performed in the non-faradaic region at −0.55 to −0.45 V *vs.* Hg/HgO (+0.35 to +0.45 V *vs.* RHE). Before each experiment, a pre-treatment CV test was performed to remove all absorbed *H*-species from the electrode surface (Figure 9.2). An appropriate potential range of ±0.05 V and a series of scan rates from 1 to 0.02 V s^{-1} (in decreasing direction) were chosen. The average current densities, $j_{average}$ (see Equation 9.6),

were plotted *versus* the scan rate, resulting in a straight line. The slope of the line corresponds to the double-layer capacitance, C_{dl}. The electrochemical surface area was then calculated by using the specific capacitance density (c) of 40 µF cm^{-2} [27] and Equation (9.7) [26]:

$$j_{average} = \frac{j_{anodic} - j_{cathodic}}{2} \quad (9.6)$$

$$A_{ecsa} = \frac{C_{dl}}{c} \quad (9.7)$$

After calculating the A_{ecsa} , the specific surface area (A_s) was obtained. The C_{dl}, A_{ecsa} and A_s of Raney-Ni electrodes at different temperatures are given in Table 9.1.

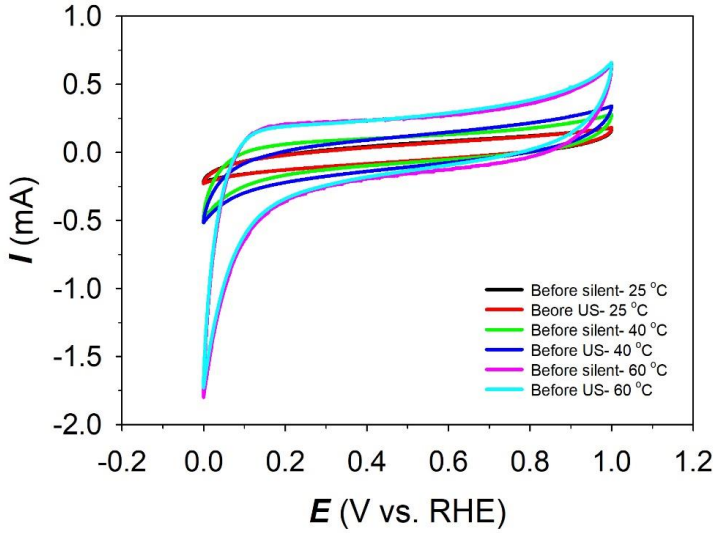

Figure 9.2. Pre-treatment CV profiles of Raney-Ni in 30 wt.-% aqueous KOH solution at a scan rate of v = 10 mV s^{-1} after purging with N_2(g) for 30 min at T = 25, 40 and 60 °C.

Table 9.1. Double-layer capacitance (C_{dl}), electrochemical surface area (A_{ecsa}) and specific surface area (A_s) of Raney-Ni at various temperatures.

Temperature (°C)	C_{dl} (mC)	A_{ecsa} (cm^2)	A_s (cm^2 g^{-1})
25	0.37	9.25	925
40	1.31	32.82	3,282
60	3.28	82.00	8,200

The electrochemical studies were performed in a double-jacketed sonoelectrochemical cell (Figure 9.3) connected to a water bath (JULABO, GmbH) to keep the temperature at T = 25, 40 and 60 °C. The electrolyte was degassed with an ultra-high purity N_2(g) (99.999% in purity) prior to and during the measurements. The WE was washed with ultra-high purity water before each sonoelectrochemical experiment. Ultrasonication was applied to the electrochemical cell by a plate transducer vibrating at a frequency f = 408 kHz (100% amplitude) powered by a multi-frequency ultrasonic generator (Meinhardt Ultrasonics). The ultrasonic or acoustic power ($P_{acoustic}$) was determined calorimetrically using the methods of Margulis *et al.* [22] and Contamine *et al*. [23] and was found to be 54 ± 1.7 W.

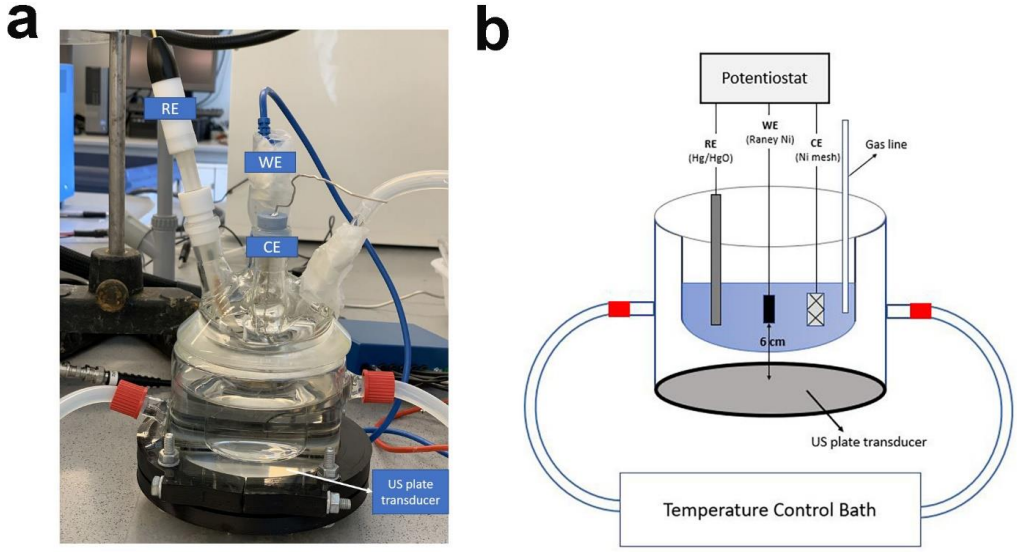

Figure 9.3. a) Experimental sonoelectrochemical set-up and b) schematic diagram of set-up.

Linear sweep voltammograms (LSV) were recorded at the potential region -0.80 ≤ E_{app} ≤ -1.50 V *vs.* Hg/HgO (+0.10 ≤ E_{app} ≤ -0.60 V *vs.* RHE) for the HER and +0.20 ≤ E_{app} ≤ +0.80 V *vs.* Hg/HgO (+1.10 ≤ E_{app} ≤ +1.70 V *vs.* RHE) for the OER experiments. The overpotentials for the OER at different temperatures were calculated based upon Equation (9.8):

$$\eta = E_{app} - E_{H2O}^{rev} \qquad (9.8)$$

where E_{app} is the applied potential *vs.* RHE and E_{H2O}^{rev} corresponds to the theoretical (reversible) cell potential for decomposition of H_2O at different temperatures. The temperature effect on the HER and OER has been discussed by many groups [24-29]. A common understanding is based upon Equation (9.9) [29]:

$$k = A \exp\left(\frac{-E_a}{RT}\right) \qquad (9.9)$$

where k is the chemical reaction rate; A is the *Arrhenius* pre-exponential factor; R is the universal gas constant (8.314 J mol^{-1} K^{-1}); T is the absolute temperature (K), and E_a is the apparent activation energy (J mol^{-1}). Equation (9.9) suggests that the higher the temperature, the faster the reaction rate so that larger current densities (at the same overpotential (η)) can be achieved at higher temperatures [29].

For the inspection of the electrodes' cross-section, scanning electron microscopy (SEM) measurements were performed using a Jeol JSM F100 equipped with a field emission gun coupled to a Bruker Quantax 200 EDS spectrometer.

9.3 Results and Discussion

9.3.1 Scanning Electron Microscopy (SEM) Characterization of Raney-Ni Before and After Ultrasonication

In order to see the stability of the coating layer of Raney-Ni under ultrasonication, SEM measurements were performed. Figures 9.4a and 9.4c show the cross-sections of Raney-Ni after immersion in 30 wt.-% aqueous KOH solution for 15 min without ultrasound (*silent*) and Figure 9.4b and 9.4d represents the cross-section of Raney-Ni after 15 min ultrasonication in 30 wt.-% aqueous KOH solution at T = 25 °C. Figure 9.4a appears to be different to the other ones. However, this could be related to the position of the cut during cross-sectional preparation. It can be seen in Figure 9.4 that ultrasound does not influence the stability of the Raney-Ni coating and the cross-section shows no delamination of the Raney-Ni under ultrasonic conditions. Figure 9.5 underpins the information from the cross-section. Figures 9.5a and 9.5b illustrate top-view SEM images of Raney-Ni after immersion in 30 wt.-% aqueous KOH solution for 15 min in the absence of ultrasound and Figures 9.5c and 9.5d demonstrate SEM micrographs of Raney-Ni after 15 min ultrasonication in 30 wt.-% aqueous KOH solution at T = 25 °C. According to Figure 9.5, the Raney-Ni layer appears to be strongly connected to the substrate, confirming the stability of the Raney-Ni coating after ultrasonication.

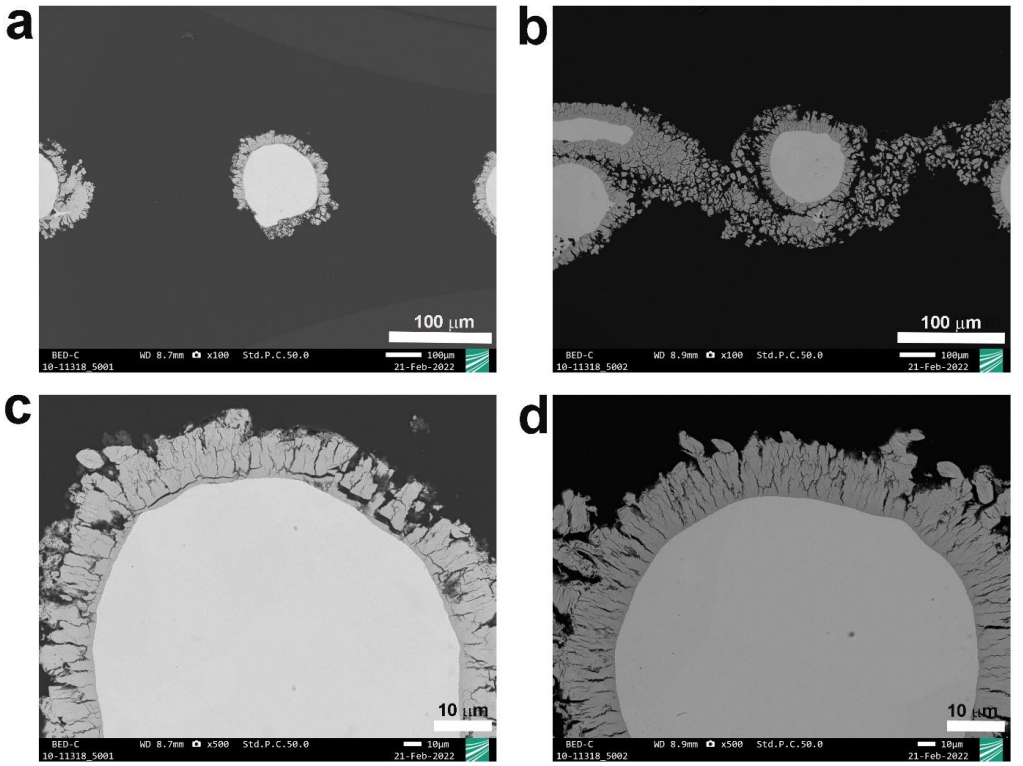

Figure 9.4. Cross-section SEM images of Raney-Ni at various magnifications: a) and c) without ultrasonication (*silent* conditions), b) and d) after ultrasonication for 15 min in 30 wt.-% aqueous KOH solution at $T = 25$ °C.

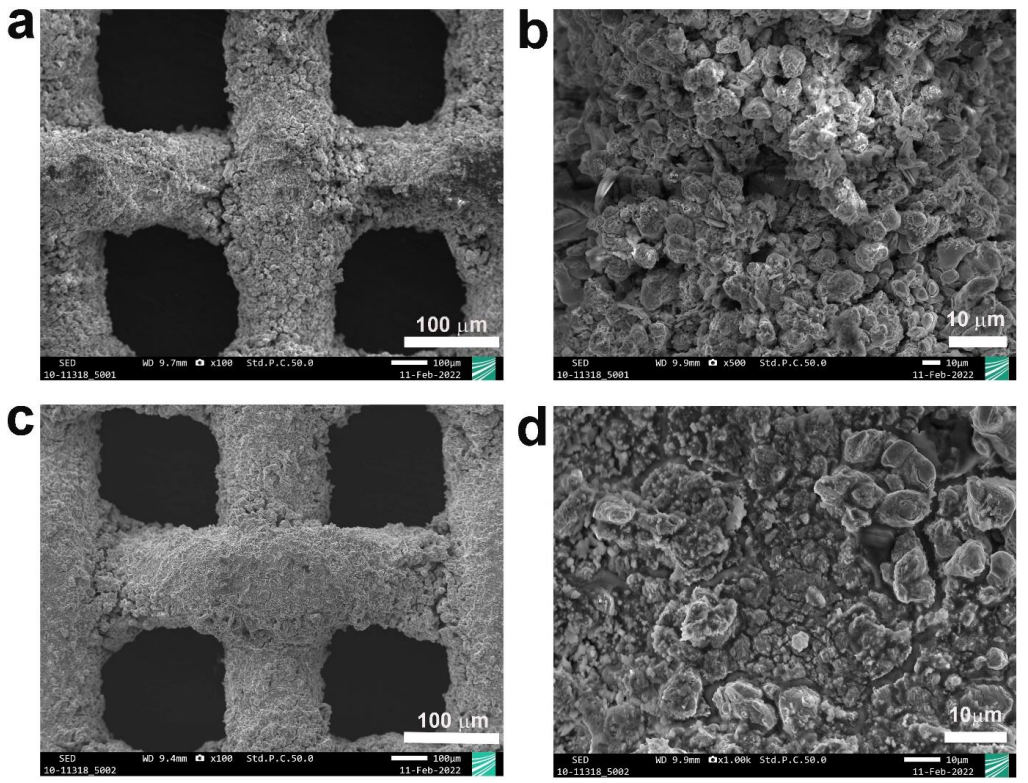

Figure 9.5. Top-view SEM images (SE mode) of Raney-Ni at different magnifications: a) and b) without ultrasonication (*silent* conditions), c) and d) after ultrasonication for 15 min in 30 wt.-% aqueous KOH solution $T = 25$ °C.

9.3.2 Effect of Power Ultrasound and Temperature on the Hydrogen Evolution Reaction

To study the effect of power ultrasound on the hydrogen evolution reaction on Raney-Ni, linear sweep voltammetry (LSV) experiments were performed in the applied potential region of $-0.80 \leq E_{app} \leq -1.50$ V *vs.* Hg/HgO ($+0.1 \leq E_{app} \leq -0.60$ V *vs.* RHE) and at a very low potential scan rate $v = 0.30$ mV s^{-1} to obtain a "quasi-steady-state" condition. Figure 9.6 shows the LSVs and the corresponding Tafel plots of Raney-Ni in the absence and presence of ultrasound at T = 25, 40 and 60 °C. In our conditions, it can be seen from the LSV curves (Figure 9.6-a,c and e) that the HER in the presence of ultrasound starts earlier for all temperatures used. Tafel slopes (b), exchange current densities (j_o) and overpotential (η) at -300 mA cm^{-2} obtained from the Tafel plots at different temperatures under *silent* and ultrasonic conditions are shown in Table 9.2. Table 9.2 shows that ultrasonication decreases the overpotential at -300 mA cm^{-2} by 34 mV (at 25 °C), 13 mV (at 40 °C) and 5 mV (at 60 °C), respectively.

Two mechanisms can be proposed to explain the decrease in overpotential under ultrasonic conditions [9]. The first is that ultrasonically produced cavitation modifies the surface of the electrode, for instance, by changing the nature of active sites available for the adsorption of hydrogen (H_{ad}) on the electrode surface. The erosion, caused by the implosion of high-energy cavitation bubbles, cleans and activates the electrode surface and produces nucleation sites continuously [21]. The second proposed mechanism is the degassing effect associated with micro-streaming (non-periodic motion of the fluid resulting from the propagation of the sound wave in the electrolyte) [30] together with acoustic cavitation. It is well-accepted in water electrolysis that the electrolyte adjacent to the electrode surface is supersaturated with molecular hydrogen (because of the low solubility of molecular hydrogen in aqueous solutions) leading to the so-called "bubble overpotential" or "bubble resistance" [9]. It is also known that acoustic streaming and cavitation help degas the solution immediately adjacent to the electrode, thus, decreasing and even eliminating this overpotential in some cases [9]. In our study, the observed decreased overpotential could be due to the elimination of gas bubbles on the surface of the electrode (second proposed mechanism) since no structural change has been observed on Raney-Ni surface after ultrasonication according to the SEM images (Figures 9.4 and 9.5).

Our results also show that the effect of ultrasonication decreases with increasing the electrolyte temperature. This phenomenon can be explained by the basic principle of

sonochemistry in pure water. Increasing temperature decreases the polytropic index ($\gamma = \frac{c_p}{c_v}$) of gases, the C_p and C_v are the specific heats of an ideal gas at constant pressure and at constant volume, respectively. When the liquid temperature increases, it causes a less violent collapse of the cavitation bubble due to the decrease of the polytropic index. Less violent collapse leads to lower internal bubble temperatures. Lower internal bubble temperature lowers the formation of free radicals by the decomposition of water i.e. sonolysis [9]. It is also known that increasing temperature quenches the cavitation process. Therefore, increasing temperature decreases the global cavitational activity of the system leading to the decrease in the sonoelectrochemical effect [31].

The Tafel slope is a specific characteristic of the HER catalysts from which some indication about the reaction mechanism of the HER and the rate-determining step (*rds*) can be obtained. The Volmer reaction involves the electroreduction of water molecules with hydrogen adsorption as shown in Equation 9.10, while Heyrovsky's reaction involves electrochemical hydrogen desorption (Eq. 9.11). The Tafel reaction involves chemical desorption (Eq. 9.12) [3, 32, 33].

$H_2O + e^- \rightarrow H_{ads} + OH^-$ Volmer (9.10)

$H_{ads} + H_2O + e^- \rightarrow H_2 + OH^-$ Heyrovsky (9.11)

$2H_{ads} \rightarrow H_2$ Tafel (9.12)

The HER pathway in alkaline medium follows the Volmer–Heyrovsky step or Volmer–Tafel step [25, 33-35]. The Tafel slopes for the HER in alkaline aqueous media at Ni materials and at room temperature have been reported by many researchers to be ca. 116–117 mV dec^{-1} in the low overpotential region [25]. However, lower values (e.g., < 100 mV dec^{-1}), as well as higher values (e.g., > 140 or higher mV dec^{-1}) of the Tafel slope, are sometimes reported for Ni materials having various forms, such as bulk Ni, porous Ni, and Raney-Ni [35-40]. According to literature, the *rds* for the HER on Ni is usually the Volmer step [41-43]. Table 9.2 shows that the Tafel slopes are between 113 mV dec^{-1} and 144 mV dec^{-1} which are in good agreement with literature and the *rds* of HER on Raney-Ni in the absence and presence of ultrasound at T = 25, 40 and 60 ℃ is the Volmer reaction, suggesting that ultrasound does not change the mechanism of the HER on Raney-Ni electrodes under our conditions.

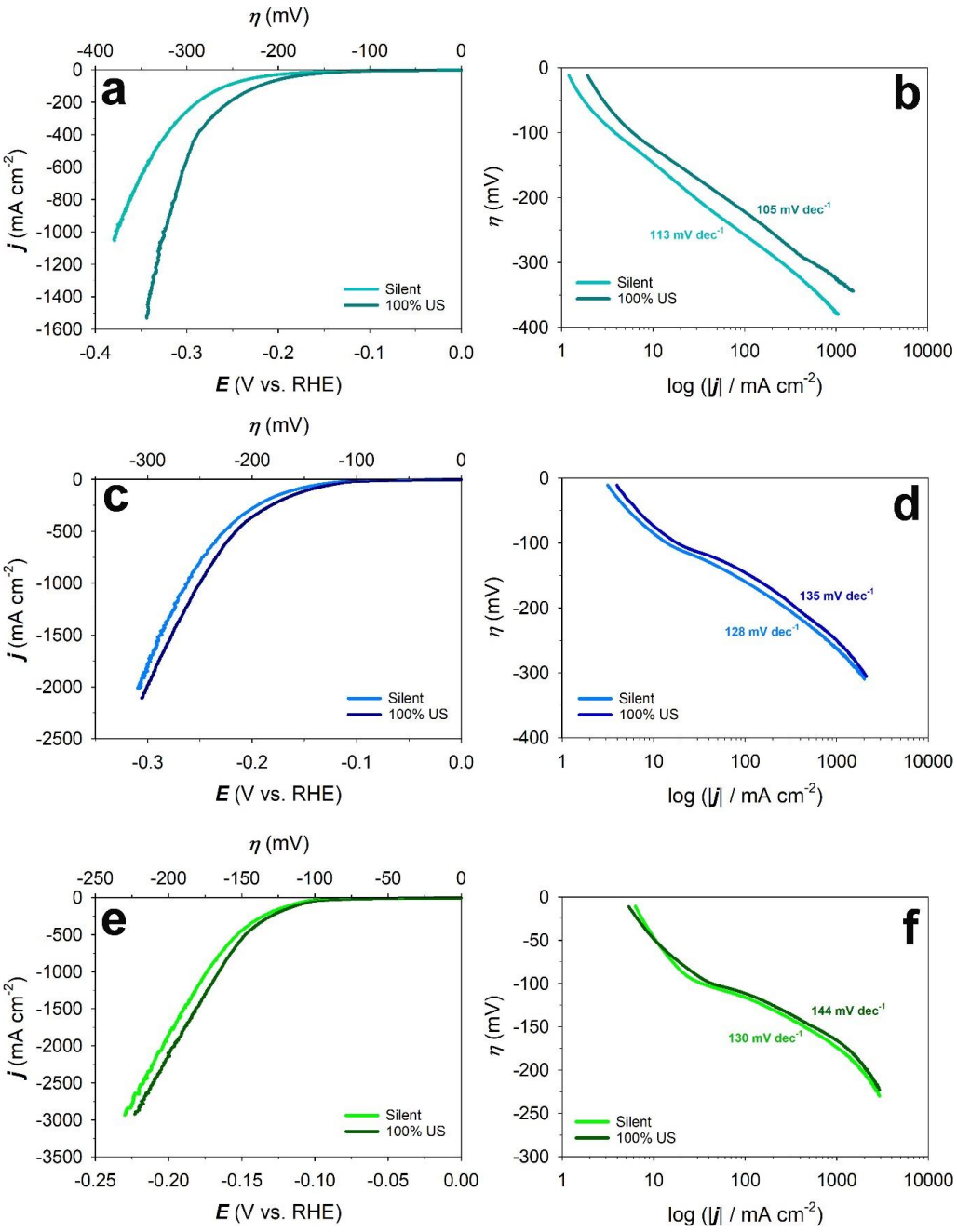

Figure 9.6. Linear sweep voltammograms (LSV) at a) 25 °C, c) 40 °C, e) 60 °C and Tafel plots of HER at b) 25 °C, d) 40 °C, f) 60 °C on Raney-Ni in 30 wt.-% aqueous KOH solution at a scan rate of $v = 0.3$ mV s^{-1} after purging with N_2(g) for 30 min under *silent* and ultrasonic (US) conditions ($f = 408$ kHz).

Table 9.2. Comparison of Tafel slopes (b), exchange current densities (j_o), overpotential (η) at -300 mA cm^{-2} and the difference between the overpotentials under *silent* and ultrasonic conditions (ΔE) for the HER on Raney-Ni in 30 wt.-% aqueous KOH solution at T = 25, 40 and 60 °C.

Temperature (°C)	Ultrasonic amplitude	b* (mV dec^{-1})	j_o (mA cm^{-2})	Overpotential at -300 mA cm^{-2} (mV)	$\Delta\eta$ (mV)
25	0 (*silent*)	113	0.52	-308	34
	100%	105	0.77	-274	
40	0 (*silent*)	128	8.38	-203	13
	100%	135	13.07	-190	
60	0 (*silent*)	130	52.78	-140	5
	100%	144	83.73	-135	

* $-180 \leq \eta \leq -300$ mV

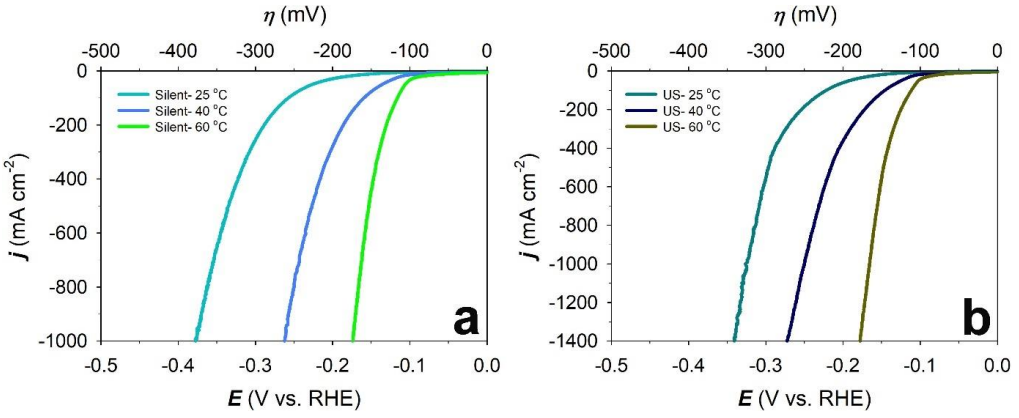

Figure 9.7. Comparison of LSV curves of HER on Raney-Ni in 30 wt.-% aqueous KOH solution in a) *silent* and b) ultrasonic (US) conditions at a scan rate of v = 0.3 mV s^{-1} and T = 25, 40 and 60 °C.

To better understand the effect of temperature on the HER on Raney-Ni, LSV curves of Raney-Ni at T = 25, 40 and 60 °C under *silent* and ultrasonic conditions were generated. Table 9.2 and Figure 9.7 show that the exchange current density (j_o) increases and the overpotential decreases by increasing the temperature. Also, the Tafel slopes under *silent* conditions increase from 113 mV dec^{-1} (at 25 °C) to 128 mV dec^{-1} (at 40 °C) and to 130 mV dec^{-1} (at 60 °C), and the Tafel slopes under ultrasonication increases from 105 mV dec^{-1} (at 25 °C) to 135 mV dec^{-1} (at 40 °C) and to 144 mV dec^{-1} (at 60 °C). These results are in good agreement with the literature since the Tafel slope increases by increasing temperature T according to Equation (9.13) [44]:

$$b = \frac{2.303\,RT}{\alpha F} \tag{9.13}$$

where α is the charge transfer coefficient, R is the gas constant, and F is the Faraday constant.

9.3.3 Effect of Ultrasound and Temperature on the Oxygen Evolution Reaction

Figure 9.8 shows the LSV curves and Tafel plots of Raney-Ni in 30 wt.-% aqueous KOH solution for the OER in the absence and presence of ultrasound at T = 25, 40 and 60 °C. These experiments were carried out in the applied potential region +0.20 ≤ E_{app} ≤ +0.80 V *vs.* Hg/HgO (+1.10 ≤ E_{app} ≤ +1.70 V *vs.* RHE) and at a potential scan rate of v = 0.30 mV s^{-1}. It is evident from the figure that ultrasound does not significantly affect the performance of Raney-Ni towards the OER compared to the HER (see before). This can be explained by the different behaviour of O_2 and H_2 bubble dynamics in the absence and presence of ultrasound [45].

There are three possible explanations: (i) the bubble coverage on the electrode for the OER is much higher than that for the HER in the absence of forced convection flow, (ii) the average size of H_2 bubbles is much smaller than that of O_2 bubbles, and (iii) the residence time of O_2 bubbles on the electrode is much longer than that of H_2 bubbles [45, 46]. Consequently, the O_2 gas bubbles are much harder to remove from the electrode surface than H_2 bubbles in our conditions, i.e., under ultrasonication at 408 kHz [45]. Li *et al.* [45] and Pollet *et al.*[20] reported that applying power ultrasound in a water electrolysis reactor improves the hydrogen production rate by 5–18% at certain current densities because the sound wave carries the hydrogen bubbles away from the electrode as soon as the hydrogen bubbles are generated and before they are able to coalesce. However, it was found that the generation of oxygen bubbles

at an electrode decreases by 8% at high electrolyte concentrations under ultrasonication [45, 47].

To this day, it is still unclear why ultrasound has little effect on the oxygen evolution at an electrode, however a few researchers have attempted to explain bubble hydrodynamic under an ultrasonic field [21, 48, 49]. Under *silent* conditions, oxygen bubbles grow and coalesce with adjacent bubbles. The buoyancy force can remove the bubbles from the surface of the electrode and once the bubble reaches a certain volume, a disengagement occurs at the interphase. When the bubbles are exposed to ultrasound, the bubbles start to oscillate and then interact with the ultrasonic field, inducing the primary *Bjerknes* force [50, 51]. Then the small bubbles start moving toward the larger bubbles, influenced by the secondary *Bjerknes* force [52]. This force is induced by the difference in compressibility and density between the bubbles. After agglomeration, the bubbles coalesce due to unstable film caused by oscillation and collision [48]. It is possible that under ultrasonication, the oxygen bubble coalescence might be prevented by the oscillation dynamics on the bubbles, and since the oxygen bubbles have a larger average diameter compared to the hydrogen bubbles, it requires a higher force to overcome the surface tension at the gas-solid interphase [49]. It is also known that the gas type also affects the bubble hydrodynamics [45]. Under ultrasonication, the oxygen bubble size might not reach a critical diameter to release it from the electrode surface via buoyancy force, and thus, disengagement would not occur.

Table 9.3 compares Tafel slopes (b), exchange current densities (j_o) and overpotential at +300 mA cm^{-2} (η_{300}) for the OER on Raney-Ni in 30 wt.-% aqueous KOH solution at T = 25, 40 and 60 °C. According to Table 3, η_{300} decreases by 13 mV (at 25 °C), and 1 mV (at 60 °C) and increases by 4 mV (at 40 °C) in presence of ultrasound. It can be observed that the Tafel slopes at low current densities are independent of temperature. Also, an increase of Tafel slope is shown at high temperatures T = 40 °C and 60 °C by applying ultrasound while at T = 25 °C the opposite behaviour can be observed. It can be suggested that ultrasound has a more pronounced effect in high current densities towards the OER.

The OER mechanism for catalysis can be based upon theoretical studies reported by Rossmeisl *et al.* [53]. Accordingly, oxygen evolution consists of four steps that involve three oxygen-adsorbed species (OH_{ad}, O_{ad} and OOH_{ad}) plus the active site (*) as intermediates in the overall process, as shown in Equations 9.14 to 9.17 [54]:

$$H_2O + * \rightleftharpoons OH_{ad} + H^+ + e^- \quad (120\ \text{mV dec}^{-1}) \quad (9.14)$$

$$OH_{ad} \rightleftharpoons O_{ad} + H^+ + e^- \quad (40\ \text{mV dec}^{-1}) \quad (9.15)$$

$$O_{ad} + H_2O \rightleftharpoons OOH_{ad} + H^+ + e^- \quad (9.16)$$

with oxygen evolution finally taking place through:

$$OOH_{ad} \rightleftharpoons * + O_2 + H^+ + e^- \quad (9.17)$$

According to our results and at low current densities, deprotonation of the adsorbent (Eq. 9.15) is the rate-limiting step in the OER process. At higher current densities, the rate-determining step moves to the oxidative adsorption of water (Eq. 9.14) [54]. It must be mentioned that the production of radicals by sonolysis has to be considered but appears to be not relevant here and further studies are necessary. Exchange current density at high overpotential regions slightly increases at all the temperatures under our investigation in presence of ultrasound. By comparing the high overpotential region at different temperatures, we can see that j_o improves by increasing temperature based upon Arrhenius' law. Also, lower overpotentials (η_{300}) can be achieved by increasing temperature (Figure 9.9).

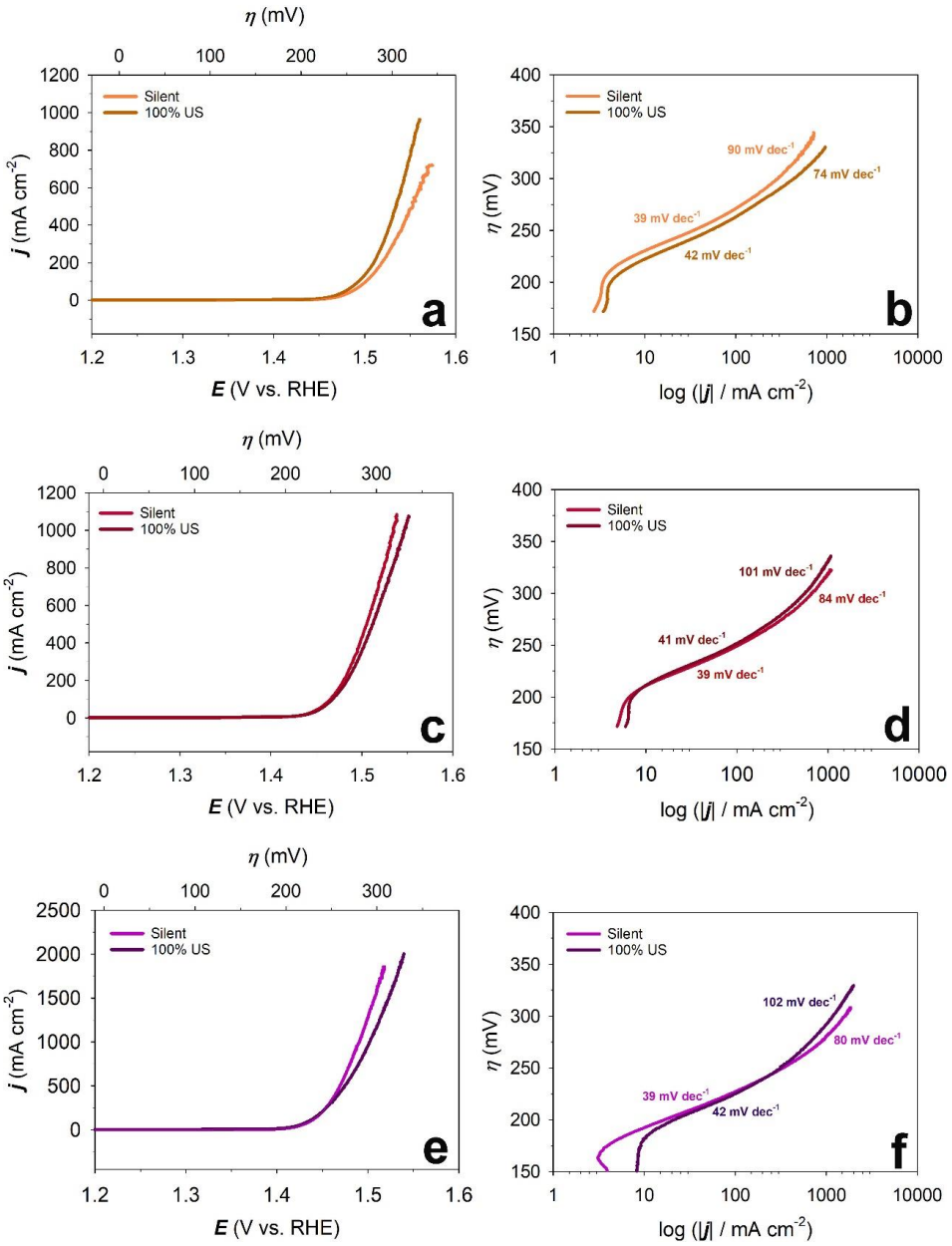

Figure 9.8. Linear sweep voltammograms (LSV) at a) 25 °C, c) 40 °C, e) 60 °C and Tafel plots of OER at b) 25 °C, d) 40 °C, f) 60 °C on Raney-Ni in 30 wt.-% aqueous KOH solution at a scan rate of v = 0.3 mV s^{-1} after purging with N_2(g) for 30 min in *silent* and ultrasonic (US) conditions (f = 408 kHz).

Table 9.3. Comparison of Tafel slopes (b), exchange current densities (j_o) and overpotential (η) at +300 mA cm^{-2} for the OER on Raney-Ni in 30 wt.-% aqueous KOH solution at T = 25, 40 and 60 °C.

Temperature (°C)	Ultrasonic amplitude	b (mV dec^{-1}) at low overpotential*	b (mV dec^{-1}) at high overpotential**	j_o (mA cm^{-2}) at low overpotential	j_o (mA cm^{-2}) at high overpotential	η +300 mA cm^{-2} (mV)
25	0 (*silent*)	39	90	1.35×10^{-5}	0.12	302
	100%	42	74	5.51×10^{-5}	0.038	290
40	0 (*silent*)	39	84	4.0×10^{-5}	0.18	274
	100%	41	101	7.9×10^{-5}	0.54	278
60	0 (*silent*)	39	80	12.0×10^{-5}	0.3	247
	100%	42	102	45.0×10^{-5}	1.25	248

* $200 \leq \eta \leq 250$ mV

** $250 \leq \eta \leq 300$ mV

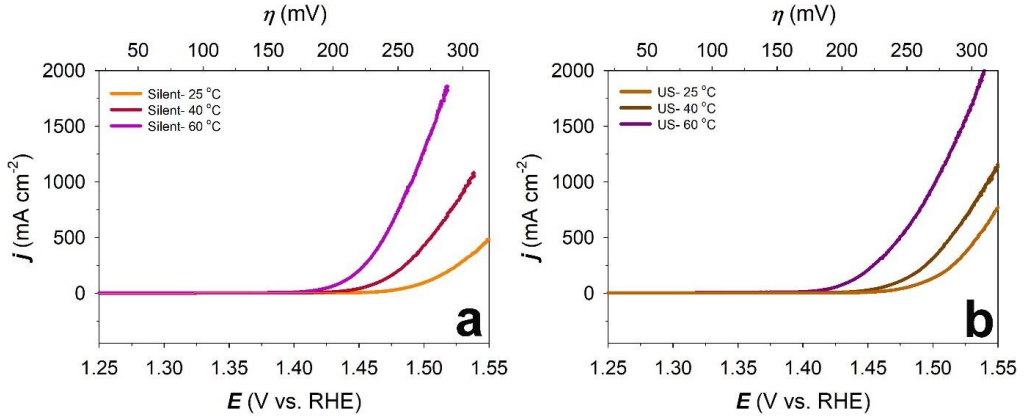

Figure 9.9. Comparison of LSV curves of OER on Raney-Ni in 30 wt.-% aqueous KOH solution in a) *silent* and b) ultrasonic (US) conditions at a scan rate of v = 0.3 mV s^{-1} and T = 25, 40 and 60 °C.

9.3.4 Electrochemical Impedance Spectroscopy (EIS) at Different Temperatures

Figure 9.10 shows the Nyquist representation of the impedance data of Raney-Ni under *silent* and ultrasonic conditions, at T = 25 °C, 40 °C and 60 °C and E = -200 mV *vs.* RHE. In both conditions at T = 25 °C and 40 °C, a depressed semi-circle can be seen which can be attributed to the porosity or surface roughness of the electrode [55-57]. Accordingly, the data at T = 25 and 40 °C were approximated by the modified Randles circuit shown in Figure 9.10, whereas the capacitance is replaced by a constant phase element. Note, for α = 1 the CPE reflects an ideal capacitance. However, at T = 60 °C the impedance consists of two partly overlapping and depressed semi-circles. The fitted electrical circuit is comprised of two RC parallel combinations in series with a resistor. R_s correlates with the cell Ohmic resistance (electrodes and current collectors). R_{ct} represents the charge transfer resistance and may also include other contributions such as the adsorption of intermediates. CPE1 is a constant phase element that represents the capacitive charging of a rough electrode. The equivalent circuit has an extra R-CPE combination, where CPE2 and R_b are suggested to represent the formation of bubbles and mass transport at the electrode−electrolyte interface [58]. The parameters obtained from the EIS measurement are shown in Table 4. The capacitance (C) can be calculated by using Equation (9.18) [55, 57].

$$C = \left[Q_1 \left(\frac{1}{R_s} + \frac{1}{R_{ct}+R_b}\right)^{(a-1)}\right]^{\frac{1}{a}} \qquad (9.18)$$

where Q_1 is the parameter of the constant phase element (CPE1), α is related to the phase angle of the frequency response, R_s is the Ohmic resistance, R_{ct} is the charge transfer resistance and R_b is the resistance due to the formation of bubbles. The CPE (constant phase element) instead of a real capacitance was used because a depressed semi-circle is observed. Furthermore, the increase of the parameter of the constant phase element, Q is mainly due to the enhancement of the active surface area. Table 9.4 presents the temperature dependence of the Ohmic resistance and charge transfer resistance. For the three temperatures i.e., 25, 40 and 60 °C, the recorded Ohmic and charge transfer resistance exhibited significant reduction by increasing the temperature. In addition, the capacitance increases by elevating the temperature which indicates a higher active surface area by rising the temperature. The above could be explained in terms of extended access to the catalytic surface within the electrode structure at elevated temperatures. In addition, higher temperatures should considerably facilitate hydrogen bubble removal [59].

As stated earlier, the effect of ultrasonication decreases with increasing the electrolyte temperature. It was found that at 25 °C and under ultrasonication, the charge transfer resistance was almost half compared to *silent* conditions. While at 60 °C, a slight decrease of R_{ct} was observed. In addition, higher capacitance values at T = 25 °C and 40 °C were observed in presence of ultrasound. The EIS results underpin our assumption that ultrasonication has mainly an impact on the gas bubble release, i.e., it can easily remove the gas bubbles from the electrode surface and bulk electrolyte to reduce the bubble surface coverage of the electrodes which in turn increase the active sites for the further reaction [21]. The Tafel as well as EIS results show that the electrode global HER activity increases with temperature (exemplarily outlined by the R_{ct}, C, and j_o values). Since HER is already greatly improved at high temperatures, adding ultrasonication does not greatly improve the HER when the electrolyte temperature is increased. Moreover, ultrasonication cannot overcompensate the reduced activity by lowering the temperature.

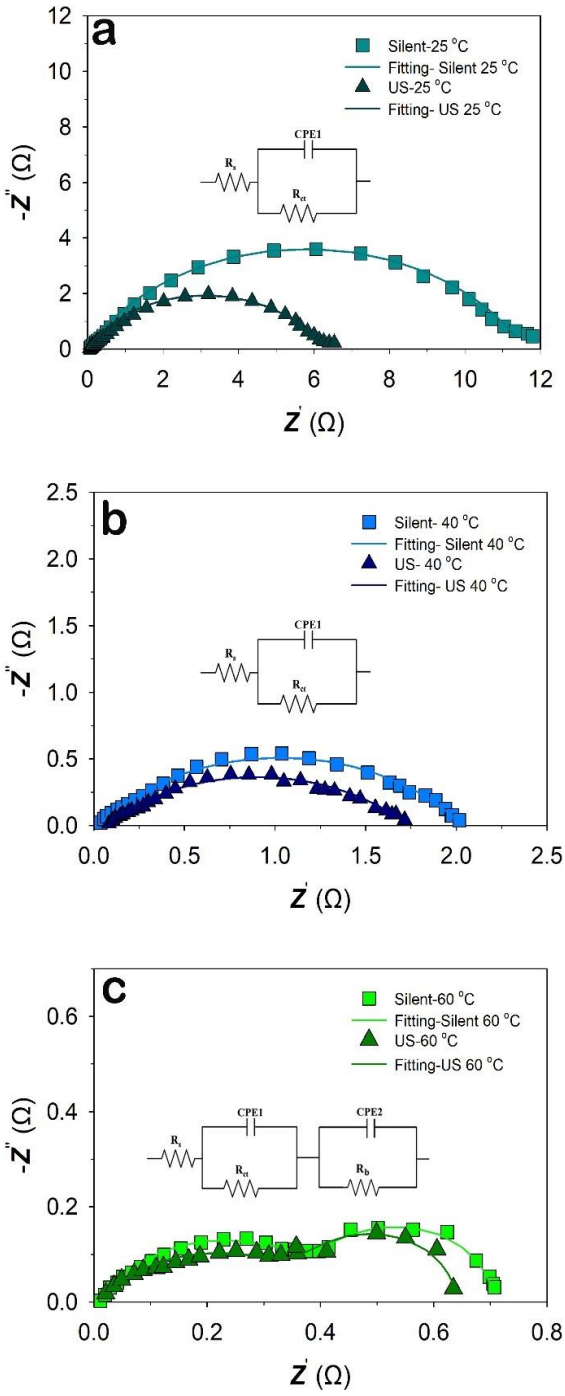

Figure 9.10. Nyquist plots of Raney-Ni in 30 wt.-% aqueous KOH under *silent* and ultrasonic (US) conditions at a) 25 °C, b) 40 °C, c) 60 °C, at the potential E = -200 mV *vs.* RHE; Inset figures show the equivalent circuit used to fit the impedance data.

Table 9.4. Parameters obtained from the EIS measurements at E = -200 mV *vs.* RHE.

Temperature (°C)	Ultrasonic amplitude	R_s (Ω)	R_{ct} (Ω)	R_b (Ω)	a	Q_1 (mF $s^{(a-1)}$)	C (mF cm^{-2})
25	0 (*silent*)	2.55	11.59	-	0.70	5.27	8.98
	100 %	2.07	6.31	-	0.70	8.17	14.40
40	0 (*silent*)	1.74	2.01	-	0.60	25	25.88
	100%	1.78	1.67	-	0.52	48	41.18
60	0 (*silent*)	1.16	0.49	0.29	0.62	49	47.06
	100%	1.04	0.47	0.24	0.58	43	36.47

Figure 9.11 shows the Nyquist representation of the impedance data of Raney-Ni under *silent* and ultrasonic conditions at T = 25, 40 and 60 °C at E = +1,550 mV *vs.* RHE in the OER region. Figure 9.11 shows depressed semi-circles which can be fitted to a modified Randles circuit as described above. The values for each circuit element/parameter are given in Table 9.5. Figure 9.11 and Table 9.5 show that under ultrasonic conditions the charge transfer resistance slightly decreases at 25 °C while at 40 and 60 °C, the charge transfer resistance increases to a slight extent. The EIS data are in good agreement with the Tafel results and illustrate that ultrasonication does not influence the mass transfer of oxygen bubbles, especially at high temperatures. In short, both the EIS and Tafel data indicate that ultrasound has a different effect on the HER and OER. While it has significant influence on the hydrogen bubble release from the electrode surface, it does not affect the O_2 bubble surface coverage at the ultrasonic frequency used (408 kHz). This may be due to the fact that the dynamic behaviour of O_2 gas bubbles for alkaline water electrolysis is different from that of H_2 bubbles [21, 46] and the ultrasound effect is directly related to gas bubbles size in electrochemical reactions [21, 49].

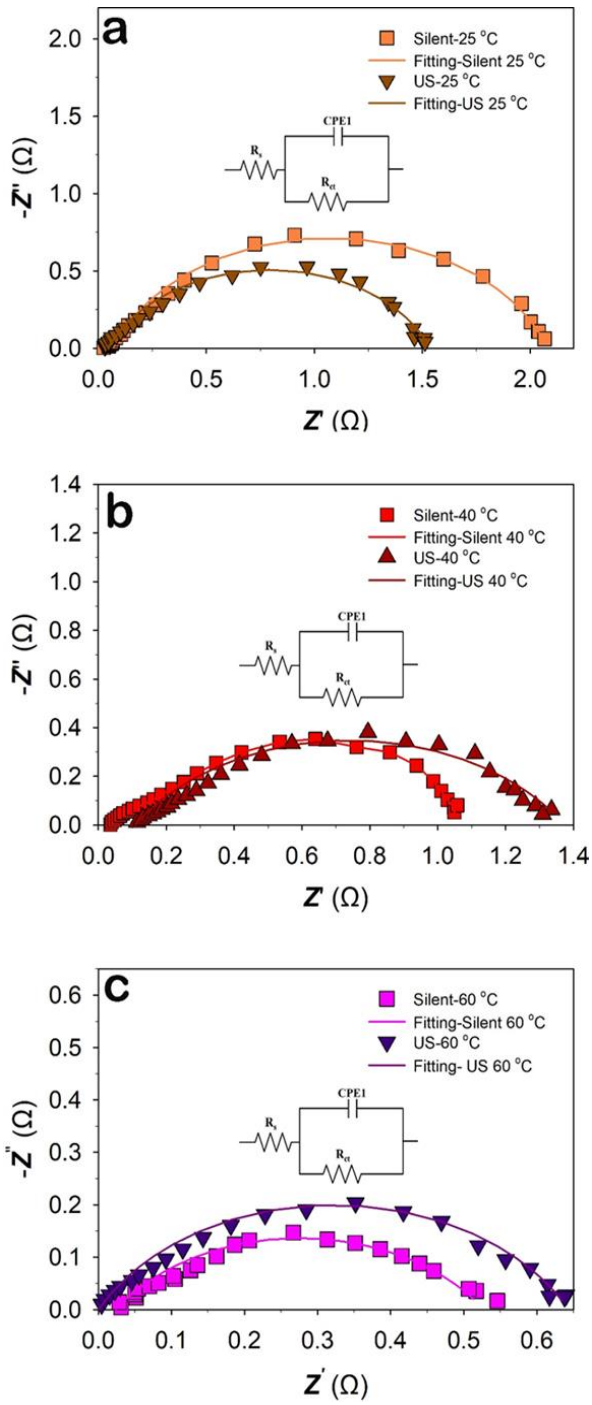

Figure 9.11. Nyquist plots of Raney-Ni in 30 wt.-% aqueous KOH under *silent* and ultrasonic (US) conditions at a) 25 °C, b) 40 °C , c) 60 °C, at the applied potential E = +1,550 mV vs. RHE; Inset figures show the equivalent circuit used to fit the impedance data.

Table 9.5. Parameters obtained from the EIS measurements at E = +1,550 mV *vs.* RHE in the OER region.

Temperature (°C)	Ultrasonic amplitude	R_s (Ω)	R_{ct} (Ω)	a	Q_1 (mF $s^{(a-1)}$)	C (mF cm^{-2})
25	0 (*silent*)	2.126	2.015	0.78	28	117.7
	100 %	1.757	1.494	0.76	35	129.4
40	0 (*silent*)	1.878	0.97	0.78	82	423.5
	100%	1.725	1.27	0.64	73	494.1
60	0 (*silent*)	1.178	0.50	0.63	135	282.1
	100%	0.939	0.64	0.71	64	200.0

9.4 Conclusions

The electrochemical kinetics and mechanism of Raney-Ni towards the HER and the OER under *silent* and ultrasonic (408 kHz) conditions have been investigated in 30 wt.- % aqueous KOH solution at different temperatures (T = 25, 40 and 60 °C). It was observed that there is a significant difference between the effect of ultrasonication on the HER and the OER. Ultrasonication significantly shifts the overpotential at -300 mA cm^{-2} (η_{300}) of HER by +34 mV at 25 °C due chiefly to the effective bubble removal while it does not influence the OER overpotential. This may be attributed to the direct dependence of the ultrasonic effect on the difference of O_2 and H_2 gas bubble sizes and dynamic behaviours. It was also shown that the ultrasonic effect on the HER depends upon temperature and ultrasonication does not play a remarkable role at high temperatures since at these temperatures, the HER is already very efficient. In addition, increasing the electrolyte temperature decreases the global cavitational activity of the system leading to a decrease in the sonoelectrochemical effect. Moreover, ultrasonication cannot overcompensate the decreasing HER activity by lowering the temperature. This study has highlighted some improvements that can be achieved using power ultrasound and the results obtained were indicative of some benefits and improvements to water electrolysis. Also, for the first time, the Tafel plots and mechanism of HER and OER on Raney-Ni under ultrasonication at different temperatures have been reported.

These preliminary findings might be helpful for experimentalists that intend to use power ultrasound in energy storage and energy conversion for hydrogen production. The performance of the sonoelectrochemical technique can be improved by the optimization of various operating conditions and parameters as follows [10]: an ultrasonic probe-type emitter is preferable for producing high-intensity bubbles and free radical formation since ultrasonic frequencies are mostly in the range of 20–100 kHz. The rate of electrochemical reaction rate mostly increases by increasing the acoustic power and intensity. Lower ultrasonic frequency is preferred over higher frequencies to improve mass transfer at the electrode. Electrode materials selection is important for efficient sonoelectrochemical processes. Finally, optimization of different experimental parameters, such as experimental design, ultrasonic frequency, acoustic power, ultrasonic transducer–electrode distance, irradiation time, electrode materials, electrode potentials, temperature, pH, conductivity, and electrolyte compositions are recommended for efficient sonoelectrochemical processes.

Acknowledgement

The authors would like to thank NTNU and ENERSENSE for the 3-year financial support towards FF's doctoral studies. The electrode production was part of the ELYntegration project which has received EU funding from the Fuel Cells and Hydrogen 2 Joint Undertaking under grant agreement No. 671458 and the Swiss State Secretariat for Education, Research and Innovation (SERI) under contract No. 15.0252.

References

[1] Pollet, B.G. and J.J. Lamb, *Hydrogen, Biomass and Bioenergy: Integration Pathways for Renewable Energy Applications*. 2020: Academic Press.

[2] Coutanceau, C., S. Baranton, and T. Audichon, *Hydrogen electrochemical production*. 2017: Academic Press.

[3] Wei, C., et al., *Recommended practices and benchmark activity for hydrogen and oxygen electrocatalysis in water splitting and fuel cells.* Advanced Materials, 2019. **31**(31): p. 1806296.

[4] Choquette, Y., et al., *Study of the kinetics of hydrogen evolution reaction on raney nickel composite-coated electrode by AC impedance technique.* Journal of The Electrochemical Society, 1990. **137**(6): p. 1723.

[5] Birry, L. and A. Lasia, *Studies of the Hydrogen evolution reaction on raney nickel—molybdenum electrodes.* Journal of applied electrochemistry, 2004. **34**(7): p. 735-749.

[6] Lohrberg, K. and P. Kohl, *Preparation and use of Raney-Ni activated cathodes for large scale hydrogen production.* Electrochimica Acta, 1984. **29**(11): p. 1557-1561.

[7] Bernäcker, C.I., et al., *A Powder Metallurgy Route to Produce Raney-Nickel Electrodes for Alkaline Water Electrolysis.* Journal of The Electrochemical Society, 2019. **166**(6): p. F357.

[8] Tanaka, S.i., et al., *Effect of Ni-Al precursor alloy on the catalytic activity for a raney-Ni cathode.* Journal of the Electrochemical Society, 2000. **147**(6): p. 2242.

[9] Islam, M.H., O.S. Burheim, and B.G. Pollet, *Sonochemical and sonoelectrochemical production of hydrogen.* Ultrasonics sonochemistry, 2019. **51**: p. 533-555.

[10] Theerthagiri, J., et al., *Sonoelectrochemistry for energy and environmental applications.* Ultrasonics Sonochemistry, 2020. **63**: p. 104960.

[11] Pollet, B., *Power ultrasound in electrochemistry: from versatile laboratory tool to engineering solution. 2012*. John Wiley & Sons.

[12] Yasui, K., *Acoustic cavitation and bubble dynamics*. 2018: Springer.

[13] Suslick, K.S., *Sonochemistry.* science, 1990. **247**(4949): p. 1439-1445.

[14] Theerthagiri, J., et al., *Application of advanced materials in sonophotocatalytic processes for the remediation of environmental pollutants.* Journal of Hazardous Materials, 2021. **412**: p. 125245.

[15] Madhavan, J., et al., *Hybrid advanced oxidation processes involving ultrasound: an overview.* Molecules, 2019. **24**(18): p. 3341.

[16] Moriguchi, N., *The effect of supersonic waves on chemical phenomena,(III). The effect on the concentration polarization.* J. Chem. Soc. Jpn, 1934. **55**: p. 749-750.

[17] Lepesant, M., *Sonoelectrochemical Production of Hydrogen for PEM Fuel Cell Applications*. 2011.

[18] Zadeh, S.H., *Hydrogen production via ultrasound-aided alkaline water electrolysis.* Journal of Automation and Control Engineering Vol, 2014. **2**(1).

[19] Symes, D., *Sonoelectrochemical (20 kHz) production of hydrogen from aqueous solutions*. 2011, University of Birmingham.

[20] Pollet, B.G., et al., *Does power ultrasound (26 kHz) affect the hydrogen evolution reaction (HER) on Pt polycrystalline electrode in a mild acidic electrolyte?* Ultrasonics Sonochemistry, 2020. **69**: p. 105238.

[21] Li, S.-D., C.-C. Wang, and C.-Y. Chen, *Water electrolysis in the presence of an ultrasonic field.* Electrochimica Acta, 2009. **54**(15): p. 3877-3883.

[22] Margulis, M. and I. Margulis, *Calorimetric method for measurement of acoustic power absorbed in a volume of a liquid.* Ultrasonics Sonochemistry, 2003. **10**(6): p. 343-345.

[23] Contamine, R.F., et al., *Power measurement in sonochemistry.* Ultrasonics Sonochemistry, 1995. **2**(1): p. S43-S47.

[24] Oshchepkov, A.G., et al., *On the effect of temperature and surface oxidation on the kinetics of hydrogen electrode reactions on nickel in alkaline media.* Electrochimica Acta, 2018. **269**: p. 111-118.

[25] Krstajić, N., et al., *On the kinetics of the hydrogen evolution reaction on nickel in alkaline solution: Part I. The mechanism.* Journal of Electroanalytical Chemistry, 2001. **512**(1-2): p. 16-26.

[26] Bockris, J.O.M. and E. Potter, *The mechanism of hydrogen evolution at nickel cathodes in aqueous solutions.* The Journal of Chemical Physics, 1952. **20**(4): p. 614-628.

[27] Miles, M., et al., *Effect of temperature on electrode kinetic parameters for hydrogen and oxygen evolution reactions on nickel electrodes in alkaline solutions.* Journal of the Electrochemical Society, 1976. **123**(3): p. 332.

[28] Krstajić, N., et al., *On the kinetics of the hydrogen evolution reaction on nickel in alkaline solution: Part II. Effect of temperature.* Journal of Electroanalytical Chemistry, 2001. **512**(1-2): p. 27-35.

[29] Zhang, G., et al., *Temperature effect on Co-based catalysts in oxygen evolution reaction.* Inorganic chemistry, 2018. **57**(5): p. 2766-2772.

[30] Wang, C. and J. Cheng, *Cavitation microstreaming generated by a bubble pair in an ultrasound field.* The Journal of the Acoustical Society of America, 2013. **134**(2): p. 1675-1682.

[31] Islam, M.H., et al., *Sonochemical conversion of CO2 into hydrocarbons: The Sabatier reaction at ambient conditions.* Ultrasonics Sonochemistry, 2021. **73**: p. 105474.

[32] Faid, A.Y., et al., *Optimized Nickel-Cobalt and Nickel-Iron Oxide Catalysts for the Hydrogen Evolution Reaction in Alkaline Water Electrolysis.* Journal of The Electrochemical Society, 2019. **166**(8): p. F519-F533.

[33] Theerthagiri, J., et al., *Fundamental aspects and recent advances in transition metal nitrides as electrocatalysts for hydrogen evolution reaction: A review.* Current Opinion in Solid State and Materials Science, 2020. **24**(1): p. 100805.

[34] Mahmood, N., et al., *Electrocatalysts for hydrogen evolution in alkaline electrolytes: mechanisms, challenges, and prospective solutions.* Advanced Science, 2018. **5**(2): p. 1700464.

[35] Theerthagiri, J., et al., *Highly electroactive Ni pyrophosphate/Pt catalyst toward hydrogen evolution reaction.* ACS applied materials & interfaces, 2019. **11**(5): p. 4969-4982.

[36] Ouyang, C., et al., *Hierarchically porous Ni3S2 nanorod array foam as highly efficient electrocatalyst for hydrogen evolution reaction and oxygen evolution reaction.* Electrochimica Acta, 2015. **174**: p. 297-301.

[37] Zhang, K., et al., *Electrocatalytic activity and electrochemical stability of Ni–S/CeO2 composite electrode for hydrogen evolution in alkaline water electrolysis.* International Journal of Hydrogen Energy, 2016. **41**(48): p. 22643-22651.

[38] Brown, I. and S. Sotiropoulos, *Preparation and characterization of microporous Ni coatings as hydrogen evolving cathodes.* Journal of applied electrochemistry, 2000. **30**(1): p. 107-111.

[39] Kibria, M., M.S. Mridha, and A. Khan, *Electrochemical studies of a nickel electrode for the hydrogen evolution reaction.* International journal of hydrogen energy, 1995. **20**(6): p. 435-440.

[40] McArthur, M., et al., *Synthesis and characterization of 3D Ni nanoparticle/carbon nanotube cathodes for hydrogen evolution in alkaline electrolyte.* Journal of Power Sources, 2014. **266**: p. 365-373.

[41] Conway, B.E. and L. Bai, *Determination of the adsorption behaviour of 'overpotential-deposited'hydrogen-atom species in the cathodic hydrogen-evolution reaction by analysis of potential-relaxation transients.* Journal of the Chemical Society, Faraday Transactions 1: Physical Chemistry in Condensed Phases, 1985. **81**(8): p. 1841-1862.

[42] Divisek, J., *Determination of the kinetics of hydrogen evolution by analysis of the potential-current and potential-coverage curves.* Journal of electroanalytical chemistry and interfacial electrochemistry, 1986. **214**(1-2): p. 615-632.

[43] Machado, S.A. and L. Avaca, *The hydrogen evolution reaction on nickel surfaces stabilized by H-absorption.* Electrochimica acta, 1994. **39**(10): p. 1385-1391.

[44] Grdeń, M. and G. Jerkiewicz, *Influence of surface treatment on the kinetics of the hydrogen evolution reaction on bulk and porous nickel materials.* Electrocatalysis, 2019. **10**(2): p. 173-183.

[45] Wang, C.-C. and C.-Y. Chen, *Water electrolysis in the presence of an ultrasonic field.* Electrochimica Acta, 2009. **54**(15): p. 3877-3883.

[46] Matsushima, H., Y. Fukunaka, and K. Kuribayashi, *Water electrolysis under microgravity: Part II. Description of gas bubble evolution phenomena.* Electrochimica acta, 2006. **51**(20): p. 4190-4198.

[47] Hung, C.-Y., C.-C. Wang, and C.-Y. Chen, *Influences of a bipolar membrane and an ultrasonic field on alkaline water electrolysis.* Journal of Membrane Science, 2012. **389**: p. 197-204.

[48] Cho, K.M., P. Deshmukh, and W.G. Shin, *Hydrodynamic behavior of bubbles at gas-evolving electrode in ultrasonic field during water electrolysis.* Ultrasonics Sonochemistry, 2021. **80**: p. 105796.

[49] Taqieddin, A., et al., *Physicochemical hydrodynamics of gas bubbles in two phase electrochemical systems.* Journal of The Electrochemical Society, 2017. **164**(13): p. E448.

[50] Leighton, T., A. Walton, and M. Pickworth, *Primary bjerknes forces.* European Journal of Physics, 1990. **11**(1): p. 47.

[51] Bjerknes, V. and J. Sandström, *Hilfsgrößen zur Berechnung der Druckverteilung in der Atmosphäre an den internationalen Tagen 1900-1903.* Beiträge zur Physik der freien Atmosphäre, 1906.

[52] Crum, L.A., *Bjerknes forces on bubbles in a stationary sound field.* The Journal of the Acoustical Society of America, 1975. **57**(6): p. 1363-1370.

[53] Rossmeisl, J., et al., *Electrolysis of water on oxide surfaces.* Journal of Electroanalytical Chemistry, 2007. **607**(1-2): p. 83-89.

[54] da Silva, G.C., N. Perini, and E.A. Ticianelli, *Effect of temperature on the activities and stabilities of hydrothermally prepared IrOx nanocatalyst layers for the oxygen evolution reaction.* Applied Catalysis B: Environmental, 2017. **218**: p. 287-297.

[55] Baumann, R., et al., *Laser Structuring of Open Cell Metal Foams for Micro Scale Surface Enlargement.* Journal of Laser Micro/Nanoengineering, 2020. **15**(2).

[56] Orazem, M.E. and B. Tribollet, *Electrochemical impedance spectroscopy.* New Jersey, 2008: p. 383-389.

[57] Li, G., et al., *New insights into evaluating catalyst activity and stability for oxygen evolution reactions in alkaline media.* Sustainable Energy & Fuels, 2018. **2**(1): p. 237-251.

[58] Faid, A.Y., et al., *Tuning Ni–MoO2 Catalyst–Ionomer and Electrolyte Interaction for Water Electrolyzers with Anion Exchange Membranes.* ACS applied energy materials, 2021. **4**(4): p. 3327-3340.

[59] Pierozynski, B. and T. Mikolajczyk, *On the temperature dependence of hydrogen evolution reaction at nickel foam and Pd-modified nickel foam catalysts.* Electrocatalysis, 2015. **6**(1): p. 51-59.

10 Conclusions and Suggestions for Future Work

10.1 Conclusions

Paper 1. We studied the effects of power ultrasound (26 kHz, up to ~75 W/cm^2) on a platinum (Pt) polycrystalline disc electrode immersed in a 0.5 M H_2SO_4 solution by cyclic and linear sweep voltammetry at 298 K. We observed that, in our experimental conditions, a ~250% increase in current density towards the hydrogen evolution reaction (HER) was achieved at maximum ultrasonic power (100%), although no obvious changes in the "real" surface area (A_r) and roughness factor (R) were observed. It was found that the HER started earlier under sonication at maximum acoustic power i.e., a ΔE shift of ~+20 mV was observed, suggesting that ultrasound improves the HER activity on Pt. A nearly 100% increase in the exchange current density (j_o) at 100% ultrasonic amplitude was observed, although the Tafel slopes (b) at high overpotentials were not greatly affected when compared to *silent* conditions. Overall, it was found that ultrasound did not significantly modify the mechanism of HER but instead increased currents at the Pt disc surface area through effective hydrogen bubble removal as indicated by the ultra-fast camera imaging experiments. From this study, it can be postulated that the main contribution of ultrasound is the efficient gas bubble removal from the electrode surface and from the bulk electrolyte in turn reducing the bubble surface coverage and the void fraction of the bulk electrolyte, respectively.

Paper 2. We have developed a simple *in-situ* method to activate Ni(poly) electrodes in 1.0 M aqueous KOH solution towards the HER by continuous and pulsed ultrasonic treatments (24 kHz, 60% amplitude, 44 W). It was shown that increasing the ultrasonic treatment time improves the HER activity and the longer ultrasonication treatment, the higher the electrocatalytic activity. Sonoactivated Ni(poly) electrode after 105 min ultrasonic treatment showed +52 mV lower overpotentials at –10 mA cm^{-2} as compared to non-activated Ni(poly). Moreover, HER rate enhanced 2-fold of magnitude after ultrasonication. Electrochemical analysis and Raman spectroscopy measurements demonstrated that ultrasonic treatment could oxidise the Ni surface and generate NiO and $Ni(OH)_2$ from 15-60 min ultrasonication while reducing the Ni surface after 75 min up to 105 min ultrasonic treatment due to acoustic cavitation and sonolytically generated radicals. This facile and economical approach could be simply used to activate Ni-based electrodes on an industrial scale for energy storage and energy conversion devices for hydrogen production.

Paper 3. The influence of pH/KOH concentration on Ni-based catalyst HER activity depends upon the catalyst composition and morphology. For polycrystalline Ni, the catalyst performance and kinetics has three regions depending upon the KOH concentration: (i) a promoting (0.01 to 0.10 M, pH=12-13), (ii) stabilizing (0.1 to 1.0 M, pH=13-14), and (iii) an inhibiting region (2.0 M, pH > 14). While for nanostructured NiMo, there is typically a promoting region under various pH/KOH concentrations (0.01 to 1.0 M, pH=12-14), and then it turns to inhibiting region at 2.0 M (pH > 14). The pH/KOH concentration has an essential role for nanostructured NiMo HER activity and kinetics, as observed from the overpotential values to achieve -10 mA/cm^2 and Tafel slope changes. The difference in pH/KOH concentration trend with polycrystalline Ni and nanostructured NiMo confirmed the importance of optimizing the electrode-electrolyte interface for optimum HER performance and kinetics.

Paper 4. We have developed a simple *in-situ* method to activate Ni(poly) electrodes in 1.0 M aqueous KOH solution towards the OER by ultrasonic treatments (24 kHz, 60% amplitude, 44 W) for 30 minutes. It was shown that ultrasound improves Ni(poly) OER activity by reducing the overpotential needed to achieve +10 mA cm^{-2} by -23 mV and charge transfer resistance from 98.5 Ω before ultrasound to 11.1 Ω after 30 min ultrasonic treatment. However, the ultrasonic treatment does not affect the electrochemical surface area of Ni(poly) or Tafel slope. The enhancement of OER activity of Ni(poly) could be attributed to the formation of free radicals by collapsing of cavitation bubbles and the secondary sonochemical reactions at the electrode/electrolyte interface.

Paper 5. The electrochemical kinetics and mechanism of Raney-Ni towards the HER and the OER under *silent* and ultrasonic (408 kHz) conditions have been investigated in 30 wt.- % aqueous KOH solution at different temperatures (T = 25, 40 and 60 °C). It was observed that there is a significant difference between the effect of ultrasonication on the HER and the OER. Ultrasonication significantly shifts the overpotential at -300 mA cm^{-2} (η_{300}) of HER by +34 mV at 25 °C due chiefly to the effective bubble removal while it does not influence the OER overpotential. This may be attributed to the direct dependence of the ultrasonic effect on the difference of O_2 and H_2 gas bubble sizes and dynamic behaviours. It was also shown that the ultrasonic effect on the HER depends upon temperature and ultrasonication does not play a remarkable role at high temperatures since at these temperatures, the HER is already very efficient. In addition, increasing the electrolyte temperature decreases the global cavitational activity of the system leading to a decrease in the sonoelectrochemical effect. Moreover, ultrasonication cannot overcompensate the decreasing HER activity by lowering the

temperature. This study has highlighted some improvements that can be achieved using power ultrasound and the results obtained were indicative of some benefits and improvements to water electrolysis. Also, for the first time, the Tafel plots and mechanism of HER and OER on Raney-Ni under ultrasonication at different temperatures have been reported.

These preliminary findings might be helpful for experimentalists that intend to use power ultrasound in energy storage and energy conversion for hydrogen production. The performance of the sonoelectrochemical technique can be improved by the optimization of various operating conditions and parameters as follows [1]: an ultrasonic probe-type emitter is preferable for producing high-intensity bubbles and free radical formation since ultrasonic frequencies are mostly in the range of 20–100 kHz. The rate of electrochemical reaction rate mostly increases by increasing the acoustic power and intensity. Lower ultrasonic frequency is preferred over higher frequencies to improve mass transfer at the electrode. Electrode materials selection is important for efficient sonoelectrochemical processes. Finally, optimization of different experimental parameters, such as experimental design, ultrasonic frequency, acoustic power, ultrasonic transducer–electrode distance, irradiation time, electrode materials, electrode potentials, temperature, pH, conductivity, and electrolyte compositions are recommended for efficient sonoelectrochemical processes.

Overall, it was found that:

1. Ultrasound does not significantly affect the electrochemical surface area of polycrystalline Ni and Pt.
2. Ultrasound does not significantly modify the Tafel slopes of HER on polycrystalline Pt and Ni, and in turn does not change the rate-determining step (*rds*) and the mechanism of the HER.
3. Ultrasound enhances the HER activity by means of decreasing the overpotential (η) and increasing the exchange current density (j_o) of HER on polycrystalline Ni and Pt.
4. Ultrasound effect on the HER is more significant at low temperatures e.g., 298 K.
5. Although some improvement has been observed in the OER on polycrystalline Ni after ultrasonication, the effect of ultrasound on the OER is not significant compared to that observed for the HER.
6. Ultrasound can be used as a simple and *in-situ* route for the activation of electrodes for water electrolysis technology.
7. Ultrasound effect is not just limited to the efficient gas bubble removal from the electrode surface, it also has the ability to modify the surface composition of the electrode by generating free sonolytic radicals.

10.2 Suggestions for Future Work

Although some light has been shed on the effects of ultrasound on the HER and the OER at poly-Ni and Pt electrodes in alkaline and acidic electrolytes, further investigations are still necessary to transfer the findings to the electrolyser industry.

We suggest the following activities that would further improve this research:

- In our study, the HER and OER reactions were performed separately as two half-cell reactions. The effect of ultrasound on the overall water splitting should be investigated.
- The cycling and long-term electrolysis should be investigated to analyse the stability of the sonoactivated materials.
- *In-situ* generation of sonolytic products at various ultrasound frequencies needs to be carried out.
- Investigations on the effects of ultrasound on the HER and the OER at various KOH and H_2SO_4 concentrations at different ultrasonic frequencies is required.
- The effects of ultrasound on the conductivity of KOH and H_2SO_4 solutions at various concentrations and frequencies needs to be studied.
- Further *in-situ* and *ex-situ* surface characterization of the electrodes such as x-ray photoelectron microscopy (XPS) and atomic force microscopy (AFM) after ultrasonication is required.
- It is necessary to understand why ultrasonication does not have a significant effect on the OER when compared to the HER. Therefore, in-depth studies on the effects of ultrasound on the OER is required.
- The effects of ultrasound on other electrode material types (inc. alloys, e.g., stainless steels, Ni alloys etc) should be studied.
- PEM and alkaline water electrolyser prototypes, which incorporate ultrasonic systems, need to be modelled, constructed and tested in order to study the HER and the OER (close to “real” applications).
- Lastly, the efficiency and the generated volumes of molecular hydrogen and oxygen gases before and after ultrasonication using the prototypes should be studied.

References

[1] Theerthagiri, J., et al., *Sonoelectrochemistry for energy and environmental applications.* Ultrasonics Sonochemistry, 2020. **63**: p. 104960.